Fluctuations in the amplitude or intensity of the output from semiconductor injection lasers also leads to optical intensity noise. These fluctuations may be caused by temperature variations or, alternatively, they result from the spontaneous emission contained in the laser output, as mentioned previously. The random intensity fluctuations create a noise source referred to as relative intensity noise (RIN), which may be defined in terms of the mean square power fluctuation $\overline{\delta P_e^2}$ and the mean optical power squared $(\bar{P}_e)^2$ which is emitted from the device following:

$$RIN = \frac{\overline{\delta P_e^2}}{(\bar{P}_e)^2} \tag{6.44}$$

The above definition allows the RIN to be measured in dB Hz^{-1} where the power fluctuation is written as:

$$\overline{\delta P_e^2}(t) = \int_0^\infty S_{RIN}(f)\, \mathrm{d}f \tag{6.45}$$

where $S_{RIN}(f)$ is related to the power spectral density of the relative intensity noise $S_{RIN}(\omega)$ by:

$$S_{RIN}(f) = 2\pi S_{RIN}(\omega) \tag{6.46}$$

where $\omega = 2\pi f$.

Hence from Eq. (6.44), the RIN as a relative power fluctuation over a bandwidth B which is defined as 1 Hz:

$$RIN = \frac{S_{RIN}(f)\ B(=1\ \mathrm{Hz})}{(\bar{P}_e)^2} \tag{6.47}$$

Typically, the RIN for a single-mode semiconductor laser would lie in the range 130 to 160 dB Hz^{-1}. However, it should be noted that the relative intensity noise decreases as the injection current level I increases following the relation:

$$RIN \propto \left(\frac{I}{I_{th}} - 1\right)^{-3} \tag{6.48}$$

where I_{th} is the laser threshold current.

From the discussion of optical detectors following in Section 8.6 it is clear that when an optical field at a frequency f is incident with power $P_o(t)$ on a photodetector whose quantum efficiency (electrons per photon) is η then the output photocurrent $I_p(t)$ is:

$$I_p(t) = \frac{\eta e P_o(t)}{hf} \tag{6.49}$$

where e is the charge on an electron and h is Planck's constant. Therefore an optical power fluctuation $\delta P_o(t)$ will cause a fluctuating current component

$\delta I_p(t) = \eta e\, \delta P_o(t)/hf$ which exhibits a mean square value:

$$\overline{i^2}(t) = \overline{\delta I_p^2}(t) = \frac{\eta^2 e^2}{(hf)^2}\, \overline{\delta P_o^2}(t) \tag{6.50}$$

Now, considering the fluctuation in the incident optical power at the detector to result from RIN in the laser emission, using Eqs. (6.44) and (6.47), and transposing $\overline{P_e}$ for P_o, then the mean square noise current in the output of the detector $\overline{i_{RIN}^2}$ due to these fluctuations is:

$$\overline{i_{RIN}^2} = \frac{\eta^2 e^2}{(hf)^2}\,(RIN)(\overline{P_e})^2 B \tag{6.51}$$

Example 6.7

The output from a single-mode semiconductor laser with a RIN value of 10^{-15} dB Hz^{-1} is incident directly on an optical detector which has a bandwidth of 100 MHz. The device is emitting at a wavelength of 1.55 μm, at which the detector has a quantum efficiency of 60%. If the mean optical power incident on the detector is 2 mW, determine: (a) the rms value of the power fluctuation and (b) the rms noise current at the output of the detector.

Solution: (a) The relative mean square fluctuation in the detected current is equal to $\overline{\delta P_e^2}/(\bar{P}_e)^2$, which, using Eqs. (6.44) and (6.47), can be written as:

$$\frac{\overline{\delta P_e^2}}{(\bar{P}_e)^2} = \frac{S_{RIN}(f)}{(\bar{P}_e)^2}\, B = 10^{-15} \times 100 \times 10^6 = 10^{-7}$$

Hence the rms value of this power fluctuation is:

$$\frac{(\overline{\delta P_e^2})^{\frac{1}{2}}}{\bar{P}_e} = 3.16 \times 10^{-4}\ \text{W}$$

(b) The rms noise current at the detector output may be obtained from Eq. (6.51) as:

$$(\overline{i_{RIN}^2})^{\frac{1}{2}} = \frac{e\eta}{hf}\,(RIN)^{\frac{1}{2}}\bar{P}_e B^{\frac{1}{2}} = \frac{e\eta\lambda}{hc}\,(RIN)^{\frac{1}{2}}\bar{P}_e B^{\frac{1}{2}}$$

$$= \frac{1.602 \times 10^{-19} \times 0.6 \times 1.55 \times 10^{-6} \times 3.16 \times 10^{-8} \times 2 \times 10^{-3} \times 10^4}{6.626 \times 10^{-34} \times 2.998 \times 10^8}$$

$$= 4.74 \times 10^{-7}\ \text{A}$$

Optical ,feedback from unwanted external reflections can also affect the intensity and frequency stability of semiconductor lasers [Ref. 59]. With multimode lasers, however, this effect is reduced because the reflections are distributed among many fiber modes and therefore they are only weakly coupled back into the laser mode

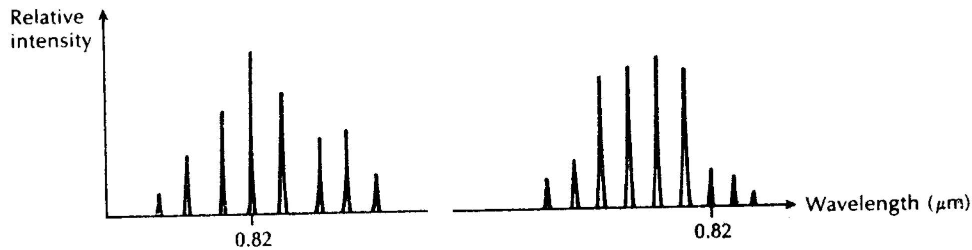

Figure 6.39 The effect of partition noise in a multimode injection laser. It is displayed as a variation in the distribution of the various longitudinal modes emitted from the device.

[Ref. 60]. The stronger fiber to laser coupling in single-mode systems, particularly those operating at 1.55 μm, can result in reflection-induced frequency hops and linewidth broadening [Ref. 51]. In these cases an optical isolator, which is a nonreciprocal device that allows light to pass in the forward direction but strongly attenuates it in the reverse direction, may be required to provide reliable single-mode operation.

Mode partition noise is a phenomenon which occurs in multimode semiconductor lasers when the modes are not well stabilized [Ref. 61]. Even when the total output power from a laser is maintained nearly constant, temperature changes can cause the relative intensities of the various longitudinal modes in the laser's output spectrum to vary considerably from one pulse to the next, as illustrated in Figure 6.39. These spectral fluctuations combined with the fiber dispersion produce random distortion of received pulses on a digital channel, causing an increase in bit error rate.

Mode partition noise can also occur in single-mode devices as a result of the residual side modes in the laser output spectrum. The effect varies between lasers emitting at 1.3 μm and those operating at 1.55 μm but, overall, a degree of side mode suppression is required in both cases in order to avoid additional errors at the receiver [Ref. 51].

6.7.5 Mode hopping

The single longitudinal mode output spectrum of a single-mode laser is illustrated in Figure 6.40(a). Mode hopping to a longer wavelength as the current is increased above threshold is demonstrated by comparison with the output spectrum shown in Figure 6.40(b). This behaviour occurs in all single-mode injection lasers and is a consequence of increases in temperature of the device junction. The transition (hopping) from one mode to another is not a continuous function of the drive current but occurs suddenly over only 1 to 2 mA. Mode hopping alters the light output against current characteristics of the laser, and is responsible for the kinks observed in the characteristics of many single-mode devices.

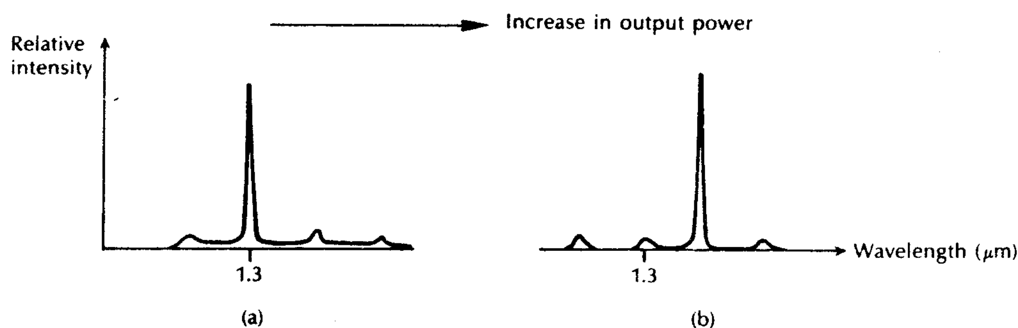

Figure 6.40 Mode hopping in a single-mode injection laser: (a) single longitudinal mode optical output: (b) mode hop to a longer peak emission wavelength at an increased optical output power.

Between hops the mode tends to shift slightly with temperature in the range 0.05 to 0.08 nm K^{-1}. Stabilization against mode hopping and mode shift may be obtained with adequate heat sinking or thermoelectric cooling. However, at constant heat sink temperature, shifts due to thermal increases can only be fully controlled by the use of feedback from external or internal grating structures (see Section 11.2.3).

6.7.6 Reliability

Device reliability has been a major problem with injection lasers and although it has been extensively studied, not all aspects of the failure mechanisms are fully understood [Ref. 13]. Nevertheless, much progress has been made since the early days when device lifetimes were very short (a few hours).

The degradation behaviour may be separated into two major processes known as 'catastrophic' and 'gradual' degradation. Catastrophic degradation is the result of mechanical damage of the mirror facets and leads to partial or complete laser failure. It is caused by the average optical flux density within the structure at the facet and therefore may be limited by using the device in a pulsed mode. However, its occurrence may severely restrict the operation (to low optical power levels) and lifetime of CW devices.

Gradual degradation mechanisms can be separated into two categories which are: (a) defect formation in the active region; and (b) degradation of the current confining junctions. These degradations are normally characterized by an increase in the threshold current for the laser which is often accompanied by a decrease in its external quantum efficiency [Ref. 62].

Defect formation in the active region can be promoted by the high density of recombining holes within the device [Ref. 63]. Internal damage may be caused by the energy released, resulting in the possible presence of strain and thermal gradients by these nonradiative carrier recombination processes. Hence if non-

radiative electron–hole recombination occurs, for instance at the damaged surface of a laser where it has been roughened, this accelerates the diffusion of the point defects into the active region of the device. The emission characteristics of the active region therefore gradually deteriorate through the accumulation of point defects until the device is no longer useful. These defect structures are generally observed as dark spot defects (DSDs).

Mobile impurities formed by the precipitation process, such as oxygen, copper or interstitial beryllium or zinc atoms, may also be displaced into the active region of the laser. These atoms tend to cluster around existing dislocations encouraging high local absorption of photons. This causes dark lines in the output spectrum of the device which are a major problem associated with gradual degradation. Such defect structures are normally referred to as dark line defects (DLDs). Both DLDs and DSDs have been observed in ageing AlGaAs lasers as well as in InGaAsP lasers [Ref. 63].

Degradation of the current confining junctions occurs in many index-guided laser structures (see Section 6.5.2) which utilize current restriction layers so that most of the injected current will flow through the active region. For example, the current flowing outside the active region in buried heterostructure (BH) lasers is known as leakage current. Hence a mode of degradation that is associated with this laser structure is an increase in the leakage current which increases the device threshold and decreases the external differential quantum efficiency with ageing.

Over recent years techniques have evolved to reduce, if not eliminate, the introduction of defects, particularly into the injection laser active region. These include the use of substrates with low dislocation densities (i.e. less than $10^{-3}\ cm^{-2}$), passivating the mirror facets to avoid surface-related effects and mounting with soft solders to avoid external strain. Together with improvements in crystal growth, device fabrication and material selection, this has led to CW injection lasers with reported mean lifetimes in excess of 10^6 hours, or more than 100 years. These projections have been reported [Ref. 64] for a variety of GaAs/AlGaAs laser structures. In the longer wavelength region where techniques were not as well advanced, earlier reported extrapolated lifetimes for CW InGaAsP/InP DH lasers were around 10^5 hours [Ref. 65]. More recently, however, InGaAsP/InP BH lasers emitting at 1.3 μm have been tested which display statistically estimated mean lifetimes in excess of 10^6 hours at operating temperatures of 50 °C [Ref. 66]. In addition DFB lasers emitting at 1.55 μm subject to accelerated ageing at a temperature of 60 °C have demonstrated stable ageing characteristics for more than 2000 hours of operating time.

6.8 Injection laser to fiber coupling

One of the major difficulties with using semiconductor lasers within optical fiber communication systems concerns the problems associated with the efficient coupling of light between the laser and the optical fiber (particularly single-mode

fiber with its small core diameter and low numerical aperture). Although injection lasers are relatively directional they have diverging output fields which do not correspond to the narrow acceptance angles of single-mode fibers. Thus butt coupling (see Figure 6.41(a)) efficiency from the laser to the fiber is often low at around 10%, even with good alignment and the use of a fiber with a well cleaved end [Ref. 67]. In this case the optimum coupling efficiency is obtained by positioning the fiber end very close to the laser facet. Unfortunately, this technique allows back reflections from the fiber to couple strongly into the laser which produce noise at the device output that can cause performance degradations in high speed systems [Ref. 68].

The coupling efficiency can be substantially improved when the output field from the laser is matched to the output field of the fiber. Such matching is usually achieved using a lens (or lens system) positioned between the laser and the fiber. A simple and popular technique is to employ a hemispherical lens formed on the end of a tapered optical fiber,* as illustrated in Figure 6.41(b) [Refs. 69, 70]. The numbers of piece-parts are therefore minimized and only one alignment step is required. Measured coupling efficiencies up to 65% have been obtained using this

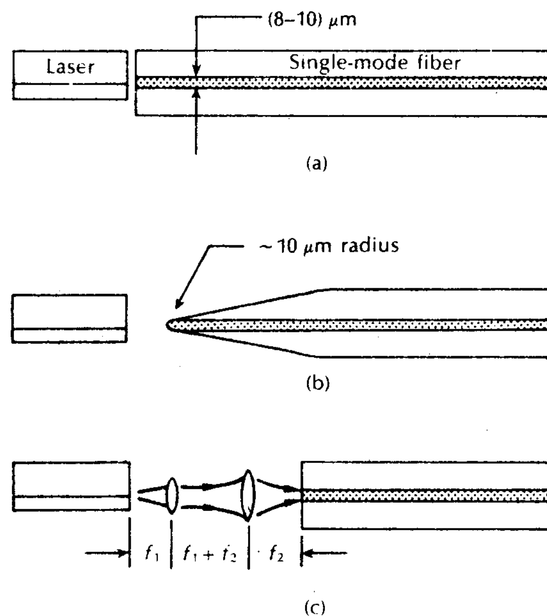

Figure 6.41 Techniques for coupling injection lasers to optical fiber, illustrated using single-mode fiber: (a) butt coupling; (b) tapered hemispherical fiber coupling; (c) confocal lens system.

* Such techniques are sometimes referred to as microlensed fibers [Ref. 71].

method [Ref. 71]. Alternative strategies for microlensed fiber coupling include the use of an etched fiber end with lens [Ref. 72] and a high index lens on the end of a fiber taper [Ref. 73]. Coupling efficiencies of 60% and 55%, respectively, have been achieved using these techniques.

Injection laser coupling using designs based on discrete lenses have also proved fruitful. In particular, such lens systems provide for a relaxation in the alignment tolerances normally required to achieve efficient microlensed fiber coupling. For example, the confocal lens system shown in Figure 6.41(c) allows a relaxation in the 1 dB tolerance by about a factor of 4 in comparison with an 8 μm radius microlensed fiber [Ref. 71]. The combination of the sphere lens and the GRIN-rod lens (see Section 5.5.1) is common within such systems because of the simplicity of the components. Coupling efficiencies of 40% have been obtained with the sphere and GRIN-rod lens in a confocal design. Furthermore, slightly higher efficiencies have been achieved using a GRIN-rod lens with one convex surface (49%) and with a silicon plano-convex lens (55%). Finally, the use of a silicon lens within a confocal system has provided coupling efficiencies of up to 70% [Ref.71].

6.9 Nonsemiconductor lasers

Although at present injection lasers are the major lasing source for optical fiber communications, certain nonsemiconductor sources are of increasing interest for application within this field. Both crystalline and glass waveguiding structures doped with rare earth ions (e.g. neodymium) show potential for use as optical communication sources. In particular, the latter devices in which the short waveguiding structures are glass optical fibers have formed an area of significant development only since 1985 [Ref. 74]. Prior to consideration of these rare earth doped fiber lasers, however, this section briefly discusses the most advanced of the crystalline solid state lasers which could find use within optical fiber communications: the Nd : YAG laser.

6.9.1 The Nd:YAG laser

The crystalline waveguiding material which forms the active medium for this laser is yttrium–aluminium–garnet ($Y_3Al_5O_{12}$) doped with the rare earth metal ion neodymium (Nd^{3+}) to form the Nd : YAG structure. The energy levels for both the lasing transitions and tne pumping are provided by the neodymium ions which are randomly distributed as substitutional impurities on lattice sites normally occupied by yttrium ions within the crystal structure. However, the maximum possible doping level is around 1.5%. This laser, which is currently utilized in a variety of areas [Ref. 75], has the following several important properties that may enable its use as an optical fiber communication source:

1. Single-mode operation near 1.064 and 1.32 μm, making it a suitable source for single-mode systems.

2. A narrow linewidth (<0.01 nm) which is useful for reducing dispersion on optical links.
3. A potentially long lifetime, although comparatively few data are available.
4. The possibility that the dimensions of the laser may be reduced to match those of the single-mode fiber.

However, the Nd : YAG laser also has the following drawbacks which are common to all neodymium doped solid state devices:

1. The device must be optically pumped. However, long lifetime AlGaAs LEDs may be utilized which improve the overall lifetime of the laser.
2. A long fluorescence lifetime of the order of 10^{-4} seconds which only allows direct modulation (see Section 7.5) of the device at very low bandwidths. Thus an external optical modulator is necessary if the laser is to be usefully utilized in optical fiber communications.
3. The device cannot take advantage of the well developed technology associated with semiconductors and integrated circuits.
4. The above requirements (i.e. pumping and modulation) tend to give a cost disadvantage in comparison with semiconductor lasers.

An illustration of a typical end pumped Nd : YAG laser is shown in Figure 6.42. It comprises a Nd : YAG rod with its ends ground flat and then silvered. One mirror is made fully reflecting whilst the other is about 10% transmitting to give the output.

The Nd : YAG laser is a four level system (see Section 6.2.3) with a number of pumping bands and fluorescent transitions. The strongest pumping bands are at wavelengths of 0.75 and 0.81 μm, giving major useful lasing transitions at 1.064 and 1.32 μm. Single-mode emission is obtained at these wavelengths with devices which are usually only around 1 cm in length [Ref. 75]. Although the Nd : YAG laser has the specific advantages and drawbacks noted above, it also has a cost disadvantage in comparison with rare earth doped glass fiber lasers (see next section) in that it is far easier and less expensive to fabricate glass fiber than it is to grow YAG crystals.

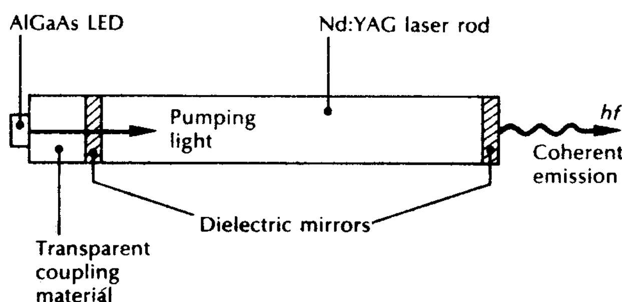

Figure 6.42 Schematic diagram of an end pumped Nd:YAG laser.

6.9.2 Glass fiber lasers

The basic structure of a glass fiber laser is shown in Figure 6.43. An optical fiber, the core of which is doped with rare earth ions, is positioned between two mirrors adjacent to its end faces which form the laser cavity. Light from a pumping laser source is launched through one mirror into the fiber core which is a waveguiding resonant structure forming a Fabry–Perot cavity. The optical output from the device is coupled through the mirror on the other fiber end face, as illustrated in Figure 6.43. Thus the fiber laser is effectively an optical wavelength converter in which the photons at the pumping wavelength are absorbed to produce the required population inversion and stimulated emission; this provides a lasing output at a wavelength which is characterized by the dopant in the fiber.

The rare earth elements, or lanthanides number fifteen and occupy the penultimate row of the periodic table. They range from lanthanum (La), with an atomic number of 57, to lutetium which has an atomic number of 71. Ionization of the rare earths normally takes place to form a trivalent state and the two major dopants currently employed for fiber lasers are neodymium (Nd^{3+}) and erbium (Er^{3+}). In common with the Nd : YAG laser (see Section 6.9.1) the former element provides a four level scheme with significant lasing outputs at wavelengths of 0.90, 1.06 and 1.32 μm. The latter element gives a three level scheme (see Section 6.2.3) with major useful lasing transitions at 0.80, 0.98 and 1.55 μm [Ref. 74]. One consequence of the number of levels involved in the laser action that is of particular significance to fiber lasers is the length dependence of the threshold power. Provided that the imperfection losses are low, then in a four level system the threshold power decreases inversely with the length of the fiber gain medium. In a three level system, however, there is an optimum length that gives the minimum threshold power which is independent of the value of the imperfection losses [Ref. 74].

The glasses which form the host materials for the rare earth doped fiber lasers mainly comprise covalently bonded molecules in the form of a disordered matrix with a wide range of bond lengths and bond angles [Ref. 76]. The rare earth ions which are impurities either act as network modifiers or are interstitially located within the glass network. To date, silica-based glasses have provided the major host material although fluorozirconate fibers (see Section 3.7) doped with both neodymium and erbium ions have produced lasers emitting at wavelengths of 1.05 and 1.35 μm, and 1.55 μm respectively. In addition, fluoride glasses with other dopants give lasing outputs in the mid-infrared wavelength range (see Section 6.11).

Both neodymium and erbium doped silica fiber lasers employ codopants such as

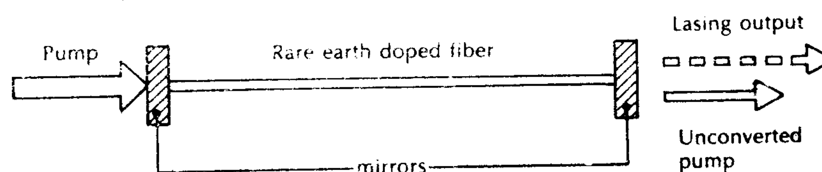

Figure 6.43 Schematic diagram showing the structure of a fiber laser.

phosphorous pentoxide (P_2O_5), germania (e.g. GeO_2, $GeCl_4$) or alumina (Al_2O_5). Dopant levels are generally low (at 400 parts per million) in order to avoid concentration quenching which causes a reduction in the population of the upper lasing levels as well as crystallization within the glass matrix [Ref. 74]. In addition, certain properties of the glass host materials lead to significant spectral broadening of the laser outputs through several mechanisms [Ref. 77] in contrast to what occurs with the Nd:YAG gain medium (see Section 6.9.1). For example, the different fluorescence spectra for an erbium doped silica fiber and a similarly doped fluorozirconate fiber (ZBLANP*) may be observed in Figure 6.44 [Ref. 78].

The light output versus absorbed pump power characteristics for two fiber lasers are displayed in Figure 6.45. The characteristic shown in Figure 6.45(a) corresponds to a neodymium doped silica fiber laser in which every effort was made to optimize the optical components in the cavity [Ref. 79]. This device in which the mirrors were dielectric coatings deposited directly on to the fiber end faces emitted at a wavelength of 1.06 μm. It may be observed from Figure 6.45(a) that the fiber laser provided a CW output power in excess of 4 mW with a threshold power of 1.51 mW. In addition, the characteristic is linear above threshold with a slope efficiency of 55%. Figure 6.45(b) corresponds to an erbium/ytterbium with alumina codoped silica fiber laser emitting at a wavelength of 1.56 μm [Ref. 80]. The device which could be injection laser pumped without the need for stringent pump-laser

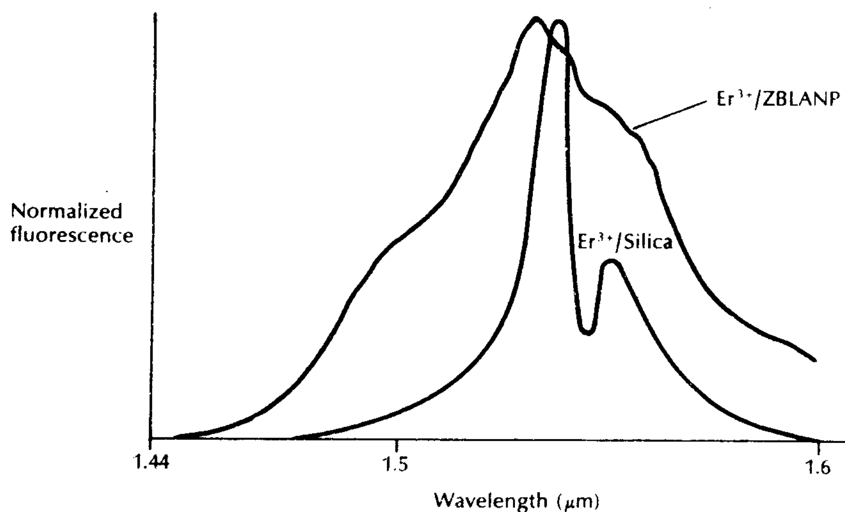

Figure 6.44 Normalized fluorescence from erbium doped silica and ZBLANP fibers. Reproduced with permission from C. A. Millar, M. C. Brierley and P. W. France, 'Optical amplification in an erbium-doped fluorozirconate fibre between 1480 nm and 1600 nm', *IEE Conf. Pub.*, **292**, Pt. 1, p. 66, 1988.

* ZBLANP fiber has lead fluoride added to the core glass to raise the relative refractive index.

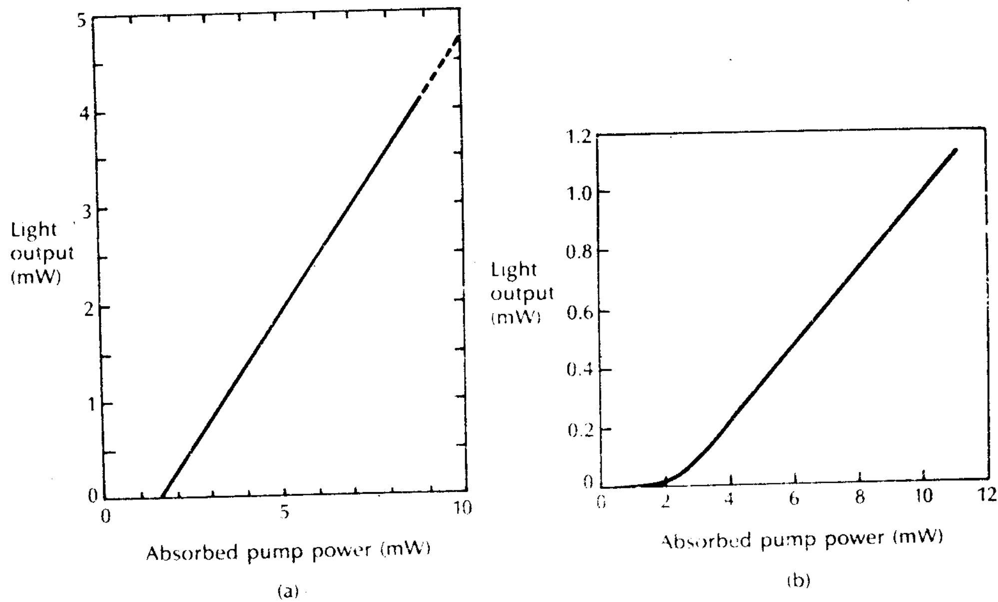

Figure 6.45 Light output against absorbed pump power characteristics for fiber lasers: (a) Neodymium doped silica fiber. Reproduced with permission from M. Shimitzu, H. Suda and M. Horiguchi, 'High efficiency Nd-doped fibre lasers using direct-coated dielectric mirrors', *Electron. Lett.*, **23**, p. 768, 1987 (IEE).
(b) Erbium/ytterbium with alumina codoped silica fiber. Reproduced with permission from D. N. Payne and L. Reekie, 'Rare-earth-doped fibre lasers and amplifers', *IEE Conf. Pub.*, **292**, Pt. 1, p. 49, 1988.

wavelength selection gave 1 mW of CW output power with a threshold power of 2 mW.

The basic Fabry–Perot cavity fiber laser shown in Figure 6.43 can be easily constructed from standard optical components but it has several limitations. In particular, the launching of light from the pump laser through one of the mirrored fiber ends can cause damage to the mirror coating as well as a substantial reduction in the launch efficiency. Furthermore, as mentioned previously, the gain spectrum of most rare earth ions extends over a wavelength range of some 50 nm. Unless the dielectric coatings on the mirrors are specially designed for broadband performance, however, the lasing output will be restricted to between 5 and 10 nm. Such a linewidth is too narrow for the provision of a broadband optical source but too wide to be used in single frequency laser applications such as coherent transmission. A number of alternative fiber laser structures have therefore been fabricated which do not require dielectric or metallic mirrors. Two of these structures, which are illustrated in Figure 6.46, are the fiber ring resonator [Ref. 81] and the fiber loop reflector made from a series concatenation of distributed reflectors using loops of fiber [Refs. 82, 83].

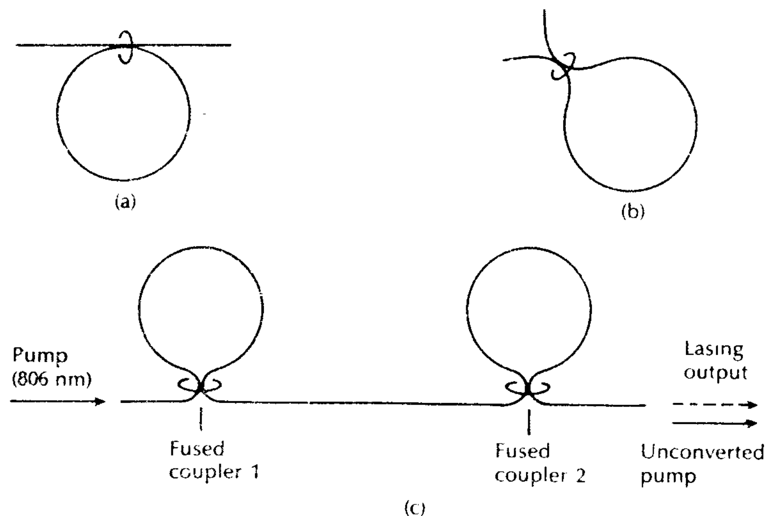

Figure 6.46 Fiber laser structures: (a) fiber ring resonator; (b) fiber loop reflector; (c) all-fiber laser made from two loops in series.

The fiber ring resonator may employ the coherent beam splitting properties of the single-mode fiber fused directional coupler (see Section 5.6.1). In this case two of the arms of the coupler are spliced together as shown in Figure 6.46(a) to form a circulating pathway in which light can travel. Hence an optical cavity without mirrors is formed, the finesse* of which is determined by the splitting ratio of the coupler. When the splitting ratio is low, the finesse is high and the energy storage on resonance is high, thus lowering the laser threshold. However, as with the Fabry–Perot laser, the lower threshold is obtained at the expense of a reduction in the slope efficiency. Alternatively, high performance fiber ring resonators can be fabricated by forming the two halves from a single fiber length. This technique has the effect of both reducing losses and of producing a higher finesse.

The structure of a fiber loop reflector which may also be based on a directional coupler is illustrated in Figure 6.46(b). However, in contrast to the fiber ring where there is energy storage within the resonant structure the fiber loop is a nonresonant interferometer (it constitutes a Sagnac interferometer, see Section 14.6.1). Light entering the loop through the input fiber end forms forward and backward (reflected) waves which are counter propagating, providing a coherent superposition of the clockwise and counterclockwise propagating fields. Hence the single fiber loop performs as a distributed all-fiber reflector which may be used to form a fiber laser [Ref. 82]. In addition, when two such loops are joined together in series a

* The finesse of the Fabry–Perot cavity provides a measure of its filtering properties and can be defined as the free spectral range divided by the full width half maximum permitted by the cavity.

resonator is obtained, as shown in Figure 6.46(c). This two loop structure provided the all-fiber laser which was fabricated from a single length of neodymium doped fiber without a splice [Ref. 83]. The excess loss of the couplers was only 0.04 dB, giving efficient laser action when the device was pumped with an AlGaAs injection laser at a wavelength of 0.806 μm and with a launch power of 470 μW. Lasing output from the device was obtained at a wavelength of 1.064 μm and was combined with the unconverted pump emission.

Narrow linewidth and frequency tunable rare earth doped fiber lasers are also under investigation and these devices are discussed in the following section.

6.10 Narrow linewidth and wavelength tunable lasers

The single frequency injection lasers described in Section 6.6 have been developed to minimize the transmission limitations resulting from fiber dispersion in high speed digital systems. For systems employing intensity modulation with direct detection of the optical signal, however, the laser linewidth and its absolute stability are of secondary importance. This is not the case with coherent optical fiber transmission where laser linewidth and stability are critical factors affecting the system performance (see Section 12.4.1). Laser linewidths in the range 1 MHz and below are required for such system applications which are around two orders of magnitude smaller than the 100 MHz linewidths obtained with 250 μm long Fabry–Perot or DFB devices which emit a few milliwatts without special linewidth control. In addition, wavelength or frequency tunable devices are considered to be key components for the provision of both the transmitter and local oscillator optical sources within coherent systems [Ref. 85].

Injection laser linewidth broadening occurs as a result of the change in lasing frequency with gain [Ref. 86]. It is a fundamental consequence of the spontaneous emission process which is directly related to fluctuations in the phase of the optical field. These phase fluctuations arise from the phase noise directly associated with the spontaneous emission process as well as the conversion of spontaneous emission amplitude noise to phase noise through a coupling mechanism between the photon and carrier densities. In the latter case, because the refractive index is strongly dependent on the carrier density which produces the gain, the fluctuations of gain due to spontaneous emission produce a substantial change in the refractive index which therefore increases the frequency/phase noise in the laser emission. The relationship for the linewidth Δf of an injection laser in terms of the emitted power P_e is given by [Ref.86]:

$$\Delta f = \frac{V_g^2 E n_{sp} \alpha_m}{8\pi P_e} (\alpha_i + \alpha_m)(1 + \alpha^2) \qquad (6.52)$$

where V_g is the group velocity, E is the carrier (electron) energy, n_{sp} (in the range 2 to 3) is the spontaneous emission factor, α_i is the internal waveguide loss per unit

length,* α_m is the mirror loss per unit length and α is called the linewidth enhancement factor. This latter parameter is defined as the ratio of the refractive index change with electron density to the differential gain change with electron density and is a measure of the amplitude to phase fluctuation conversion caused by the spontaneous emission. It can take up values between 2 and 16 depending upon the device material composition, structure and operating wavelength. The term $(1 + \alpha^2)$ in Eq. (6.52) results from the contributions to the linewidth of the two phase fluctuation effects.

It is clear that as the laser power increases, the spontaneous emission becomes relatively less important at the higher photon densities and hence the device linewidth decreases. However, as the output power of the laser cannot be made arbitrarily large, then a more effective method to reduce the linewidth is to make the cavity longer. The linewidth is decreased by increasing the laser length because the effective mirror loss α_m per unit length in Eq. (6.52) is decreased. Two techniques which can be utilized to increase the injection laser cavity length are to either use a long laser chip or to extend the cavity with a passive medium such as air, an optical fiber or an appropriate semiconductor integrated passive waveguide [Refs. 18, 38]. The latter external cavity devices also provide wavelength/frequency tunability.

6.10.1 Long external cavity lasers

Extension of the laser cavity length by the introduction of external feedback can be achieved by using an external cavity with a wavelength dispersive element as part of the cavity. Such devices are often referred to as long external cavity (LEC) lasers. A wavelength dispersive element is required because the long resonator structure has very closely spaced longitudinal modes which necessitates additional wavelength selectivity. A common technique for laboratory use is illustrated in Figure 6.47 where a diffraction grating is employed as an external mirror in order to filter the lasing emission from the wide gain spectrum of a laser chip giving a narrow linewidth at a desired wavelength [Refs. 87, 88]. Spectral linewidths as narrow as 10 kHz have been reported with such devices [Refs. 85, 87]. Furthermore, wavelength tuning of the output may be achieved by mechanical rotation of the grating such that the lasing wavelength moves with mode hops from one longitudinal mode to the next. In general, coarse spectral adjustment is obtained by rotation of the grating, whilst fine tuning can be achieved by lateral translation of the grating, as shown in Figure 6.47. Coarse tuning of a single-mode 1.5 μm laser over 90 nm through rotation of the external grating with fine tuning of the same device over approximately 1 GHz by lateral translation of the grating has been demonstrated [Ref. 89].

Another long external cavity method which has been proposed [Ref. 90] employs an external prism grating and graded-index (GRIN) rod lens (see Section 5.5.1)

* α_i is the injection laser equivalent of the laser loss coefficient per unit length $\bar{\alpha}$ defined in Section 6.2.5.

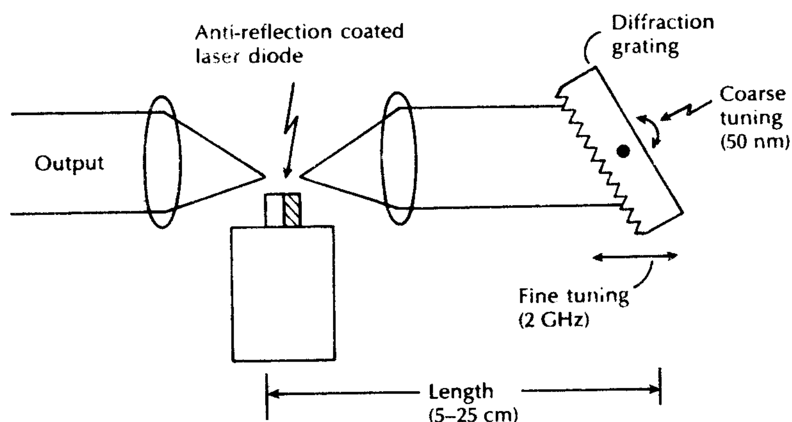

Figure 6.47 Wavelength tuning of an ILD using an external reflective diffraction grating (long external cavity technique).

combination. This technique enabled coarse wavelength adjustment of a buried heterostructure single-mode device over a range of 40 nm through the lateral displacement of the GRIN-rod lens relative to the laser chip. Fine tuning of around 6 GHz μm^{-1} could be achieved by slight variations in the separation between the laser chip and the GRIN-rod lens end face. The principal disadvantage with these mechanically tuned devices is their relatively low switching speeds. However, by using electro-optic [Ref. 91], acousto-optic [Ref. 92] devices to modulate the external cavity, much higher switching speeds can be achieved. Wavelength selection can then be produced by altering the electro-optic or acousto-optic drive frequency. For example, an acousto-optic filter and modulator pair has been used to select wavelengths over a range of 35 nm for a 0.85 μm laser, with switching speeds of 10 ns [Ref. 93].

6.10.2 Integrated external cavity lasers

An alternative technique for the provision of the external cavity is the integrated waveguide approach. Such monolithic integrated devices often utilize the distributed feedback (DFB) or the distributed Bragg reflector (DBR) structure. An example of an integrated external cavity DBR laser providing narrow linewidth dynamic single-mode (DSM) operation at a wavelength of 1.51 μm is shown in Figure 6.48 [Ref. 94]. This device which had a cavity length of 4.5 mm exhibited a spectral linewidth of 2 MHz with some 6 mW of optical output power.

Monolithic integrated DSM lasers also offer the potential for wavelength tuning. There are, in principle, two techniques which can be employed to tune these devices. One method is to use the mode selectivity of a coupled cavity structure such as a C^3 laser (see Section 6.6.1) [Ref. 29]. In this case the effective gain peak wavelength is controlled by the multicavity structure together with multisegment

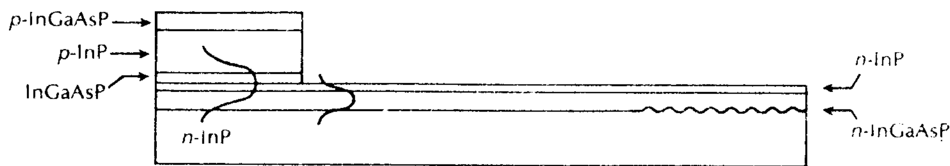

Figure 6.48 Structure of an integrated external cavity DBR laser.

electrodes, as illustrated in Figure 6.49(a). Hence the lasing wavelength can be varied within the effective gain width which is a range in excess of 15 nm for a 1.5 μm InGaAsP laser [Ref. 95]. The device wavelength changes, however, with mode jumps and thus this technique does not provide continuous wavelength tunability.

The other wavelength tuning method for monolithic integrated lasers is to use a refractive index change in the device cavity provided by current injection or the application of an electric field. Typically, this is achieved by employing a multiple electrode DFB or DBR structure [Ref. 38]. For example, with a single electrode DFB laser operated above threshold, the high injected carrier density (10^{18} cm^{-3}) reduces the effective refractive index in the corrugation region (Bragg region), thereby decreasing the lasing wavelength. Most of the injected carriers recombine, however, to produce photons which results in a very small increase in the carrier density leading to only a very small change in the lasing wavelength. The two electrode DFB laser shown in Figure 6.49(b) allows the wavelength tuning range to be improved by the application of a large current to one electrode and a small current to the other.

With the asymmetric DFB laser structure of Figure 6.49(b), the optical field is higher in the region near the output port where the facet is nonreflecting (antireflection (AR) coated, as shown in diagram), and the device operating wavelength is primarily determined by the effective refractive index in this region. When the aforementioned section is pumped at current densities at or slightly below the threshold density (under uniform pumping) simply to overcome the absorption losses, then it acts as a Bragg reflector. Furthermore, the injected carriers do not

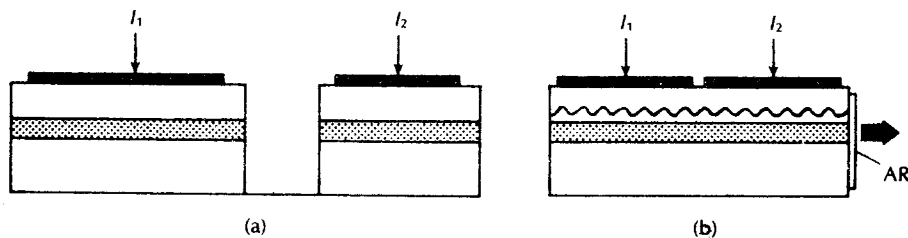

Figure 6.49 Monolithic integrated DSM lasers: (a) cleaved-coupled-cavity (C^3) laser; (b) double-sectioned DFB laser.

contribute significantly to the generation of photons because of the low pumping level. This factor results in a large change of refractive index which gives wavelength tuning. It should be noted that the gain is provided by the other section which is pumped well above threshold. A maximum continuous tuning range of 3.3 nm with 1 mW output power has been obtained with such a device [Ref. 96]. The spectral linewidth of this laser was 15 MHz and the tuning range reduced to 2 nm at an output power of 5 mW.

Three electrode DFB lasers have also demonstrated good tunability. A $\lambda/4$ shifted device (see Section 6.6.2) in which the two outer electrodes were electrically connected to a common current supply whilst the central electrode was supplied with a different current has given a continuous tuning range of 2 nm by varying the two currents [Ref. 97]. In addition, the device displayed a spectral linewidth of only 500 kHz. Although such tunable DFB lasers have a limited tuning range in comparison with coupled cavity devices, they exhibit advantages of ease of fabrication as well as providing continuous tuning rather than discrete jumps.

Multiple electrode DBR laser structures have also been developed to allow wavelength tuning [Ref. 95]. In particular, wider wavelength tuning ranges have been obtained by not only separating the Bragg region in the passive waveguide (a large bandgap material) from the active region (a small bandgap material) inside the laser cavity but also by introducing a phase region within the waveguide. The structure of such a three-sectioned DBR laser is illustrated in Figure 6.50(a). The wavelength of this device can simply be electronically tuned by current injection into the DBR section. This region exhibits a high reflectance within a certain wavelength band (the stop band) which is nominally between 2 and 4 nm wide. The mechanism which results from a refractive index change in the passive waveguide layer is known as Bragg wavelength control. A continuous tuning range, however, is limited to the resonant mode spacing which is defined from the effective cavity length of the laser. It is the mode which is nearest to the centre of the stop band and which simultaneously satisfies the 2π round trip phase condition that lases. Therefore, the introduction of the phase region in the waveguide (Figure 6.50(a)) which is independently controlled by the injection current allows the lasing wavelength to be tuned around each Bragg wavelength. Such a region provides phase control which again occurs through refractive index changes in the passive waveguide.

The combination of the two types of tuning (Bragg wavelength and phase tuning) provides a significantly larger tuning range because the lasing wavelength deviation from the Bragg wavelength can be compensated by phase control. With good design and the independent adjustment of the three currents in the active Bragg and phase regions, quasi-continuous tuning ranges between 8 and 10 nm have been obtained [Refs. 38, 98]. In addition, a continuous tuning range of 6.2 nm has been achieved with a similar device [Ref. 99]. Alternatively, for continuous wavelength tuning, one control current has been divided in a prescribed proportion into the Bragg and phase sections as illustrated in Figure 6.50(b). Continuous tuning ranges of between 2 and 4 nm have been reported using this method [Ref. 38]

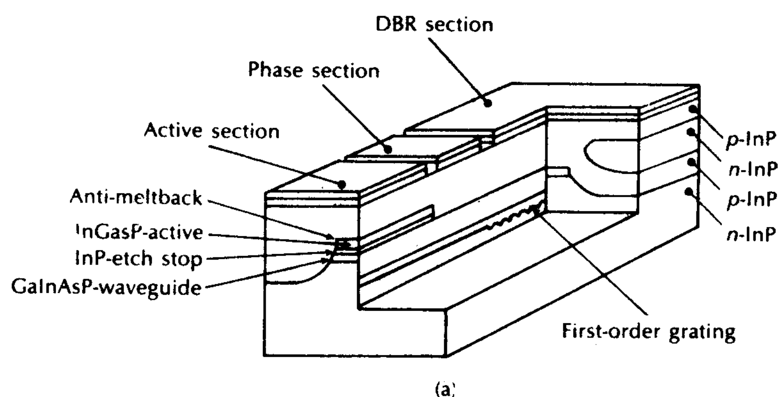

(a)

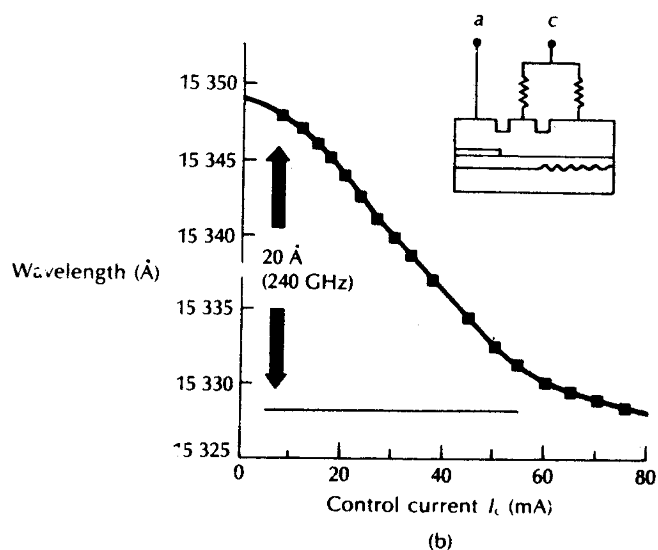

(b)

Figure 6.50 Three-sectioned DBR laser: (a) structure; (b) range of continuous wavelength tuning. Reproduced with permission from T. P. Lee and C. E. Zah, 'Wavelength-tunable and single-frequency semiconductor lasers for photonic communications networks' *IEEE Commun. Mag*, p. 42, Oct., 1989. Copyright © 1989 IEEE.

6.10.3 Fiber lasers

Techniques are also under investigation to obtain narrow linewidth output from glass fiber lasers [Ref. 74]. The rare earth doped fiber lasers described in Section 6.9.2 have spectral linewidths typically in the range 0.1 to 1 nm which are too broad for high speed transmission. One method to achieve narrower spectral linewidths employed polished silica blocks with surface gratings, as illustrated in Figure 6.51

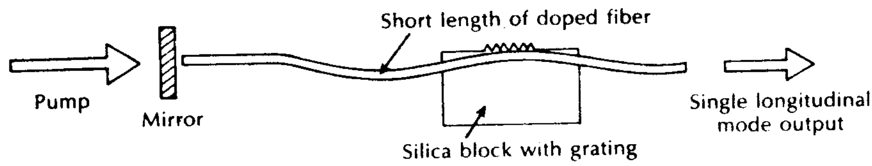

Figure 6.51 Fiber laser with a cavity incorporating a polished silica block and grating reflector [Ref. 100].

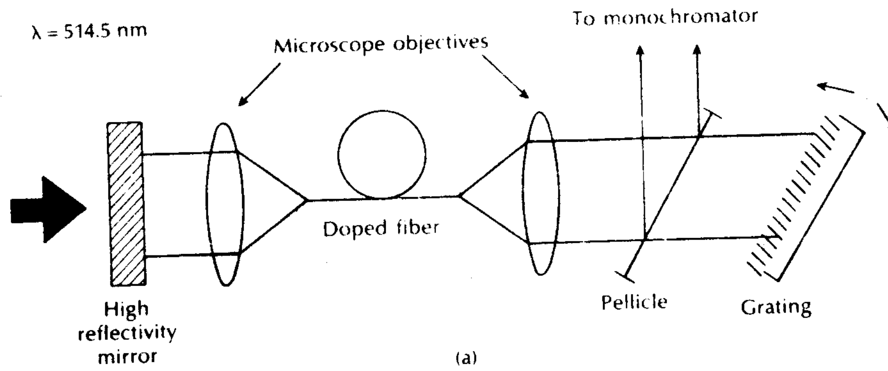

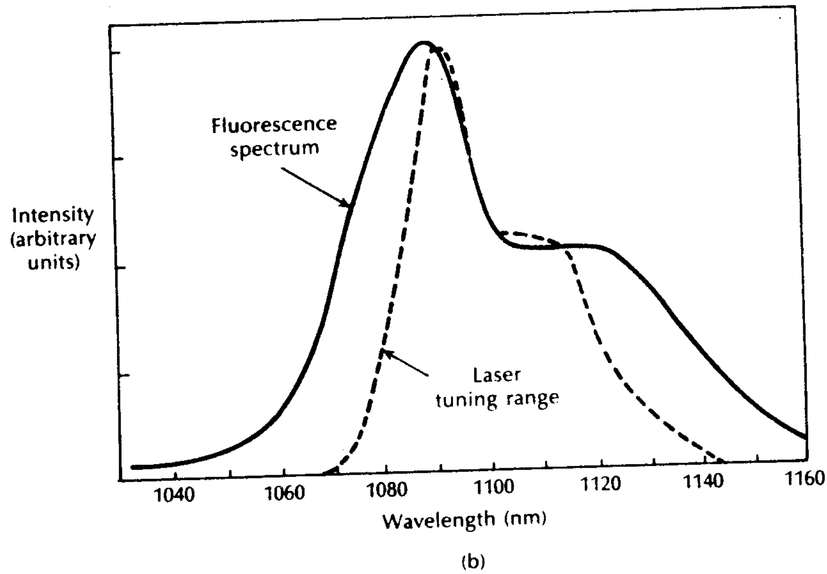

Figure 6.52 Tunable neodymium-doped single-mode fiber laser: (a) configuration; (b) fluorescence spectrum for doped fiber and the laser tuning range. Reproduced with permission from L. Reekie, R. J. Mears, S. B. Poole and D. N. Payne, 'Tunable single-mode fiber lasers', *J. Lightwave Technol.*, **LT-4**, p. 956, 1986. Copyright © 1986 IEEE.

[Ref. 100]. In this case the holographic gratings acted as distributed feedback reflectors which reflected only a narrow band of wavelengths. The reflector (Figure 6.51) through which the pump beam was launched was a dielectric mirror butted against the fiber end. Moreover, the fiber in the coupler block was undoped and one end was butt jointed to an erbium doped fiber. An output spectral linewidth of 0.04 nm (5 GHz) was obtained which is indicative of the relative state of development of fiber lasers in comparison with semiconductor devices.

Substantially narrower spectral linewidths have, however, been obtained with fiber lasers using a fiber Fox–Smith resonator design [Ref. 74]. This device which employs a fused coupler fabricated from erbium doped fiber has demonstrated a lasing linewidth of less than 8.5 MHz which compares favourably with the linewidths obtained from conventional semiconductor DFB lasers but not external cavity lasers.

Finally, wavelength tuning has also been obtained with fiber lasers. In particular, the use of silica as the laser medium provides good power handling characteristics and broadens the rare earth transitions, enabling tunable devices. An investigation of wavelength tuning in a neodymium (Nd^{3+}) doped single-mode fiber laser employed the experimental configuration shown in Figure 6.52(a) [Ref. 101]. Tuning was accomplished by changing the angle of the diffraction grating, which was mounted on a sine-bar-driven turntable. A tuning range of 80 nm was obtained, as may be observed from the characteristic (including the fluorescence spectrum of Nd^{3+} ions in silica) displayed in Figure 6.52(b). Furthermore, the wavelength tuning of an erbium (Er^{3+}) doped single-mode fiber laser was also reported [Ref. 101] to provide a tuning range of 25 nm around the 1.54 μm wavelength region using a similar experimental configuration.

An alternative method for wavelength tuning of fiber lasers employed the loop reflector discussed in Section 6.9.2. In this case a temperature shift was used to adjust the coupling ratio through the directional coupler which had a direct effect on the output optical wavelength. A 60 °C variation in temperature provided a tuning range of around 33 nm [Ref. 102].

6.11 Mid-infrared lasers

Laser sources for transmission at wavelengths beyond 2 μm, in particular gas and solid state lasers as well as low temperature injection lasers, have been utilized in nontelecommunications applications such as high resolution spectroscopy, materials processing and remote monitoring. More recently, however, progress in the potentially ultra-low-loss fibers for mid-infrared transmission (see Section 3.7) operating over the wavelength range 2 to 5 μm has encouraged greater activity in the pursuit of longer wavelength optical sources. For practical communication systems in the mid-infrared wavelength region the requirement is for semiconductor or fiber lasers which are capable of operating at, or close to, room temperature.

Semiconductor materials with direct bandgaps which encompass the mid-infrared wavelength range include many of the III–V, II–VI and IV–VI alloys. Injection lasers operating in this longer wavelength region, however, are subject to increased carrier losses over devices emitting at wavelengths up to 1.6 μm which result from nonradiative recombination via the Auger interaction [Ref. 103]. The recombination energy of the injected carriers is dissipated as thermal energy to the remaining free carriers by this process. Moreover, the probability of the occurrence of such a process increases as the bandgap of the semiconductor is reduced. In addition, optical losses due to free carrier absorption are also greater because of their dependence on the square of the wavelength. Both of these effects present more problems in the mid-infrared wavelength range and they exhibit increased importance at higher temperatures as a result of the higher concentration of free carriers. They therefore play a major role in the determination of the injection laser threshold current and efficiency, as well as providing a limit to the maximum operating temperature of the device.

The total current required to provide the injection laser threshold is greater than the amount attributable only to radiative recombination by the addition of an Auger current. Although the Auger current depends upon the precise electronic band structure of the material, and often consists of contributions from a number of different Auger transitions, it is generally large for materials with bandgaps which provide longer wavelength emission. In this context the results of calculations for threshold current and internal quantum efficiency for several long wavelength semiconductor alloys are displayed in Figure 6.53 [Ref. 104]. A comparison of the highest predicted oscillation temperatures of pulsed DH lasers fabricated from various compounds as a function of wavelength, based on estimates of the temperature at which the device internal quantum efficiency at current threshold falls to 2.5%, is shown. In addition, experimental observations are depicted as data points in the figure. It may be observed from Figure 6.53 that this data indicates an overall limit to room temperature laser action at wavelengths slightly above 2 μm for any of the semiconductor alloys investigated.

Room temperature operation of III–V alloy semiconductor lasers fabricated from InGaAsSb, and GaAlAsSb lattice matched to either GaSb or InAs has been obtained in the wavelength range 2.2 to 2.3 μm [Refs. 105, 106] Low threshold current density of 1.7 kA cm^{-2} at room temperature has also been reported [Ref. 107] but although laser oscillation is predicted to occur up to a wavelength of 4.4 μm, it is at a temperature of only 77 K due to the presence of the Auger current [Ref. 18]. In addition, the InAsPSb lattice matched to InAs offers the potential for operation over the 2 to 3.5 μm wavelength region but calculations indicate a similar dependence of the maximum operating temperature on wavelength to GaInAsSb (see Figure 6.53).

An example of a II–VI alloy semiconductor is the HgCdTe material system, also shown in Figure 6.53, from which infrared detectors have been fabricated (see Section 8.10). Although LEDs and optically pumped lasers for operation over the wavelength range 2 to 4 μm have been demonstrated using this alloy, injection laser

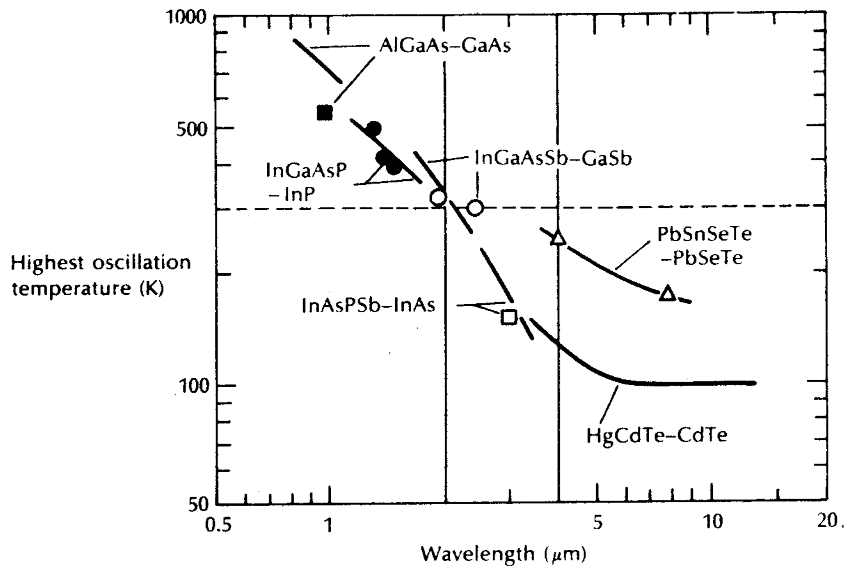

Figure 6.53 Characteristics showing maximum temperature of pulsed operation for DH lasers versus wavelength for several material systems [Ref. 104].

sources have as yet to be reported [Ref. 18]. Injection lasers, however, fabricated from IV–VI lead–salt alloys have been developed for high resolution spectroscopic as well as gas monitoring applications. Devices based on the quaternary PbSnSeTe and related ternary compounds generally emit at wavelengths longer than 4 μm. In this case the Auger effects have been calculated [Ref. 104] to be less in certain of these alloys than those obtained in III–V semiconductor materials, which could provide both lower current thresholds and higher maximum operating temperatures. The replacement of Sn with Eu, Cd or Ge increases the bandgap to provide shorter wavelength operation. For example, the structure of some recently reported ternary alloy PbEuTe/PbTe DH lasers [Ref. 108] is shown in Figure 6.54. These mesa-stripe devices which emitted over the 3.5 to 6.5 μm wavelength range provided in excess of 200 μW output power at temperatures up to 210 K in pulsed operation.

The investigation of rare earth doped fiber lasers for application in the mid-infrared wavelength region is also under way. In particular, fluorozirconate fiber lasers doped with erbium [Ref. 109], holium [Ref. 110] and thulium [Ref. 111] have been reported to provide emissions in the 2 to 3 μm wavelength range. The 2.702 μm transition in erbium which had only previously been obtained in bulk fluorozirconate glass samples [Ref. 74] was demonstrated in a CW fiber laser pumped at twice threshold [Ref. 109]. Lasing was obtained when 191 mW of pump light at a wavelength of 0.477 μm was launched into the doped fluorozirconate fiber.

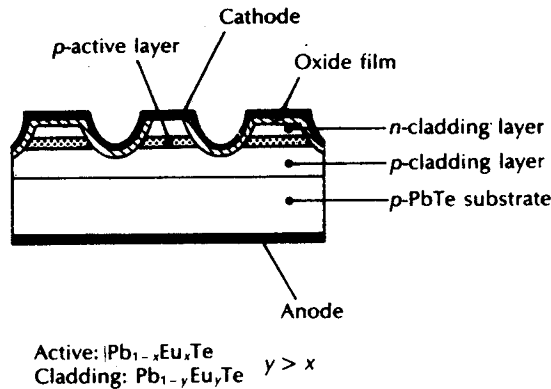

Figure 6.54 Structure of PbEuTe/PbTe DH laser [Ref. 108].

The holium doped fluorozirconate fiber was made to lase with a CW output at wavelengths of 1.38 μm and 2.08 μm [Ref. 110]. In both cases, pumping was obtained from an argon ion source at a wavelength of 0.488 μm and the 2.08 μm emission was the first report of the operation of a fiber laser at wavelengths beyond 1.55 μm [Ref. 74]. Finally, the thulium doped fiber laser emitted at a wavelength of 2.3 μm when pumped with the pulsed output from an alexandrite laser at 0.786 μm [Ref. 111]. Unlike the longer wavelength holium emission which originates from a three level system, the thulium system at 2.3 μm is four level in which the pump band is also the upper lasing level.

Problems

6.1 Briefly outline the general requirements for a source in optical fiber communications.
Discuss the areas in which the injection laser fulfils these requirements, and comment on any drawbacks of using this device as an optical fiber communication source.

6.2 Briefly describe the two processes by which light can be emitted from an atom. Discuss the requirement for population inversion in order that stimulated emission may dominate over spontaneous emission. Illustrate your answer with an energy level diagram of a common nonsemiconductor laser.

6.3 Discuss the mechanism of optical feedback to provide oscillation and hence amplification within the laser. Indicate how this provides a distinctive spectral output from the device.
The longitudinal modes of a gallium arsenide injection laser emitting at a wavelength of 0.87 μm are separated in frequency by 278 GHz. Determine the length of the optical cavity and the number of longitudinal modes emitted. The refractive index of gallium arsenide is 3.6.

6.4 An injection laser has a GaAs active region with a bandgap energy of 1.43 eV. Estimate the wavelength of optical emission from the device and determine its linewidth in Hertz when the measured spectral width is 0.1 nm.

6.5 When GaSb is used in the fabrication of an electroluminescent source, estimate the necessary hole concentration in the p type region in order that the radiative minority carrier lifetime is 1 ns.

6.6 The energy bandgap for lightly doped gallium arsenide at room temperature is 1.43 eV. When the material is heavily doped (degenerative) it is found that the lasing transitions involve 'bandtail' states which effectively reduce the bandgap transition by 8%. Determine the difference in the emission wavelength of the light between the lightly doped and this heavily doped case.

6.7 With the aid of suitable diagrams, discuss the principles of operation of the injection laser.

Outline the semiconductor materials used for emission over the wavelength range 0.8 to 1.7 μm and give reasons for their choice.

6.8 Determine the range of bandgap energies for:

(a) $Al_yGa_{1-y}As/Al_xGa_{1-x}As$;
(b) $In_{1-x}Ga_xAs_yP_{1-y}/InP$.

6.9 A DH injection laser has an optical cavity of length 50 μm and width 15 μm. At normal operating temperature the loss coefficient is 10 cm^{-1} and the current threshold is 50 mA. When the mirror reflectivity at each end of the optical cavity is 0.3, estimate the gain factor $\bar{\beta}$ for the device. It may be assumed that the current is confined to the optical cavity.

6.10 The coated mirror reflectivity at either end of the 350 μm long optical cavity of an injection laser is 0.5 and 0.65. At normal operating temperature the threshold current density for the device is 2×10^3 A cm^{-2} and the gain factor β is 22×10^{-3} cm A^{-1}. Estimate the loss coefficient in the optical cavity.

6.11 Describe the techniques used to give both electrical and optical confinement in multimode injection lasers. Contrast these techniques when used in gain-guided and index-guided lasers.

6.12 A gallium arsenide injection laser with a cavity of length 500 μm has a loss coefficient of 20 cm^{-1}. The measured differential external quantum efficiency of the device is 45%. Calculate the internal quantum efficiency of the laser. The refractive index of gallium arsenide is 3.6.

6.13 Compare the ideal light output against current characteristic for the injection laser with one from a typical gain-guided device. Describe the points of significance on the characteristics and suggest why the two differ.

6.14 Describe, with the aid of suitable diagrams, the major strategies and structures utilized in the fabrication of single frequency injection lasers. Indicate the reasons for the great interest in such devices.

6.15 The threshold current density for a stripe geometry AlGaAs laser is 3000 A cm^{-1} at a temperature of 15 °C. Estimate the required threshold current at a temperature of 60 °C when the threshold temperature coefficient T_0 for the device is 180 K, and the contact stripe is 20×100 μm.

6.16 Briefly describe what is meant by the following terms when they are used in relation to injection lasers:

(a) relaxation oscillations;
(b) frequency chirp;
(c) partition noise;
(d) mode hopping.

6.17 The rms value of the power fluctuation on the output from a single-mode semiconductor laser is 2×10^{-4} W when the relative intensity noise (RIN) is -160 dB Hz^{-1}. The emission, which is at a wavelength of 1.30 μm, is directly incident on an optical detector with a quantum efficiency of 70% at this wavelength. If the rms noise current at the detector output is 0.53 μA, and assuming that the RIN is the dominant noise source, calculate the mean optical power incident on the photodetector.

6.18 A single-mode injection laser launches light with a 3 dB linewidth Δf into a fiber link which has two connectors exhibiting reflectivities r_1 and r_2. It is known that the worst case relative intensity noise (RIN) occurs when the direct and doubly reflected optical fields interfere in quadrature [Ref. 112] following:

$$RIN(f) = \frac{4r_1r_2}{\pi}\frac{\Delta f}{f^2 + \Delta f^2}\left[1 + \exp(-4\pi\,\Delta f\,\tau) - 2\exp(-2\pi\,\Delta f\,\tau)\cos(2\pi f\tau)\right]$$

Demonstrate that the above expression reduces to:

$$RIN(f) = \frac{16r_1r_2}{\pi}\Delta f\tau^2 \qquad \text{for } \Delta f\cdot\tau \ll 1$$

and

$$RIN(f) = \frac{4r_1r_2}{\pi}\frac{\Delta f}{f^2 + \Delta f^2} \qquad \text{for } f\cdot\tau \gg 1$$

6.19 A DFB laser has a 3 dB linewidth Δf of 50 MHz. It is connected to a short optical jumper cable such that $\Delta f\cdot\tau$ is 0.1. Using the relationship given in Problem 6.18 when the frequency f is also 50 MHz, obtain the average reflectivity for each of the connectors so that the RIN is reduced below a level of -130 dB Hz^{-1}.

6.20 Discuss degradation mechanisms in injection lasers. Comment on these with regard to the CW lifetime of the devices.

6.21 Describe the structure and operation of a glass fiber laser. Comment on the glass compounds currently employed together with their fluorescence spectra.

6.22 Discuss linewidth narrowing and wavelength tunability associated with single frequency injection lasers. Outline the major techniques which are being adopted to facilitate these characteristics.

Answers to numerical problems

6.3 150 μm, 1241
6.4 0.87 μm, 39.6 GHz
6.5 4.2×10^{18} cm^{-3}
6.6 0.07 μm
6.8 (a) 1.38 to 1.91 eV
(b) 0.73 to 1.35 eV
6.9 3.76×10^{-2} cm A^{-1}
6.10 28 cm^{-1}
6.12 84.5%
6.15 77.0 mA
6.17 3.6 mW
6.19 -25.2 dB

References

[1] C. Kittel, *Introduction to Solid State Physics* (5th edn), John Wiley, 1976.
[2] E. S. Yang, *Fundamentals of Semiconductor Devices*, McGraw-Hill, 1978.

[3] Y. P. Varshni, 'Band to band radiative recombination in groups IV, VI and III–V semiconductor I', *Phys. Stat. Solidi (Germany)*, **19**(2), pp. 459–514, 1967.

[4] H. Kressel and J. K. Butler, *Semiconductor Lasers and Heterojunction LEDs*, Academic Press, 1977.

[5] H. Kressel, 'Electroluminescent sources for fiber systems', in M. K. Barnoski (Ed.), *Fundamentals of Optical Fiber communications*, pp. 109–141, Academic Press, 1976.

[6] S. M. Sze, *Physics of Semiconductor Devices* (2nd edn), John Wiley, 1981.

[7] H. C. Casey and M. B. Parish, *Heterostructure Lasers: Part A and B*, Academic Press, 1978.

[8] A. Yariv, *Optical Electronics* (4th edn), Holt, Rinehart and Winston, 1991.

[9] K. Y Lau and A. Yariv, 'High-frequency current modulation of semiconductor injection lasers', in *Semiconductors and Semimetals*, 22, Pt. B, pp. 70–152, Academic Press, 1985.

[10] J. C. Dyment, L. A. D'Asaro, J. C. Norht, B. I. Miller and J. E. Ripper, 'Proton-bombardment formation of stripe-geometry heterostructure lasers for 300 K CW operation', *Proc. IEEE*, **60**, pp. 726–728, 1982.

[11] H. Kressel and M. Ettenburg, 'Low-threshold double, heterojunction AlGaAs/GaAs laser diodes: theory and experiment', *J. Appl. Phys.*, **47**(8), pp. 3533–3537, 1976.

[12] P. R. Selway, A. R. Goodwin and P. A. Kirby, 'Semiconductor laser light sources for optical fiber communications', in C. P. Sandbank (Ed.), *Optical Fiber Communication Systems*, pp. 156–183, John Wiley, 1980.

[13] N. K. Dutta, 'Optical sources for lightwave systems applications', in E. E. Basch (Ed.) *Optical-Fiber Transmission*, H. W. Sams & Co., 1987.

[14] I. P. Kaminow, L. W. Stulz, J. S. Ko, A. G. Dentai, R. E. Nahory, J. C. DeWinter and R. L. Hartman, 'Low-Threshold InGaAsP ridge waveguide lasers at 1.3 μm', *IEEE J. Quantum Electron.*, **QE-19**, pp. 1312–1319, 1983.

[15] C. J. Armistead, S. A. Wheeler, R. G. Plumb and R. W Musk, 'Low threshold ridge waveguide lasers at λ = 1.5 μm', *Electron. Lett.*, **22**, pp. 1145–1147, 1986.

[16] S. E. H. Turley, G. D. Henshall, P. D. Greene, V. P. Knight, D. M. Moule and S. A. Wheeler, 'Properties of inverted rib-waveguide lasers operating at 1.3 μm wavelength', *Electron. Lett.*, **17**, pp. 868–870, 1981.

[17] K. Saito and R. Ito, 'Buried-heterostructure AlGaAs lasers', *IEEE J. Quantum Electron.*, **QE-16**(2), pp. 205–215, 1980.

[18] J. E. Bowers and M. A. Pollack, 'Semiconductor lasers for telecommunications', in S. E. Miller and I. P. Kaminow (Eds.), *Optical Fiber Telecommunications II*, Academic Press, pp. 509–568, 1988.

[19] I. Mito, M. Kitamura, K. Kobayashi, S. Murata, M. Seki, Y. Odagiri, H. Nishimoto, M. Yamaguchi and K. Kobayashi, 'InGaAsP double-channel planar buried-heterostructure laser diode (DCPBH LD) with effective current confinement', *IEEE J. Lightwave Technol.*, **LT-1**, pp. 195–202, 1983.

[20] N. K. Dutta, R. B. Wilson, D. P. Wilt, P. Besomi, R. L. Brown, R. J. Nelson and R. W. Dixon, 'Performance comparison of InGaAsP lasers emitting at 1.3 and 1.55 μm for lightwave system applications', *AT&T Tech. J.*, **64**, pp. 1857–1884, 1985.

[21] S. E. Miller, 'Integrated low-noise lasers', *Electron., Lett.* **22**, pp. 256–257, 1986.

[22] J. E. Bowers, B. R. Hemenway, A. H. Gnauck, T. J. Bridges and E. G. Burkhardt, 'High-frequency constricted mesa lasers', *Appl. Phys. Lett.*, **47**, pp. 78–80, 1985.

[23] W. T. Tsang, 'Extremely low threshold AlGaAs modified multiquantum-well heterostructure lasers grown by MBE', *Appl. Phys. Lett.*, **39**, p. 786, 1981.

[24] T. E. Bell, 'Single-frequency semiconductor lasers', *IEEE Spectrum*, **20**, p. 38, 1983.

[25] T. Nakagami and T. Sakurai, 'Optical and optoelectronic devices for optical fiber transmission systems', *IEEE Commun. Mag.*, **26**(1), pp. 28–33, 1988.

[26] H. Blauvelt, N. Bar-Chaim, D. Fekete, S. Margalet and A. Yariv, 'AlGaAs lasers with micro-cleaved mirrors suitable for monolithic integration', *Appl. Phys. Lett.*, **40**, pp. 289–290, 1982.

[27] L. A. Coldren, K. Furuya, B. I. Miller and J. A. Rentschler, 'Etched mirror and groove-coupled GaInAsP/InP laser devices for integrated optics', *IEEE J. Quantum Electron.*, **QE-18**, pp. 1679–1688, 1982.

[28] K.-Y. Liou, C. A. Burrus, R. A. Linke, I. P. Kaminow, S. W. Granlund, C. B. Swan and P. Besomi, 'Single longitudinal-mode stabilized graded-index-rod external coupled-cavity laser', *Appl. Phys. Lett.*, **45**, p. 729, 1984.

[29] W. T. Tsang, N. A. Olsson and R. A. Logan, 'High-speed direct single-frequency modulation with large tuning rate in cleaved-coupled-cavity lasers', *Appl. Phys. Lett.*, **42**(8), pp. 650–651, 1983.

[30] L. A. Coldren, G. D. Boyd, J. E. Bowers and C. A. Burrus, 'Reduced dynamic linewidth in three-terminal two-section diode lasers', *Appl. Phys. Lett.*, **46**, pp. 125–127, 1985.

[31] D. R. Scifres, R. D. Burham and W. Streifer, 'Distributed feedback single heterojunction diode laser', *Appl. Phys. Lett.*, **25**, p. 203, 1974.

[32] W. T. Tsang and S. Wang, 'GaAs-AlGaAs double-heterostructure injection laser with distributed Bragg reflector', *Appl. Phys. Lett.*, **28**, p. 596, 1976.

[33] M. Nakumura, K. Aidi, J. Umeda and A. Yariv, 'CW operation of distributed-feedback GaAs-GaAlAs diode lasers at temperatures up to 300 K', *Appl. Phys. Lett.*, **27**(7), pp. 403–405, 1975.

[34] H. Ishiawa, H. Soda, K. Wakao, K. Kihara, K. Kamite, Y. Kotaki, M. Matsuda, H. Sudo, S. Yamakoshi, S. Isozumi and H. Imai, 'Distributed feedback laser emitting at 1.3 μm for gigabit communication systems', *J. Lightwave Technol.*, **LT-5**(6), pp. 848–855, 1987.

[35] S. Tsuji, A. Ohishi, H. Nakamura, M. Hirao, N. Chinone and H. Matsumura, 'Low threshold operation of 1.5 μm DFB laser diodes', *J. Lightwave Technol.*, **LT-5**(6), pp. 822–826, 1987.

[36] K. Utaka, S. Akiba, K. Sakai and Y. Matsushima, 'λ/4 shifted InGaAsP/InP DFB lasers', *IEEE J. Quantum Electron*, **QE-22**, pp. 1042–1051, 1986.

[37] S. Akiba, M. Usami and K. Utaka, '1.5 μm λ/4 shifted InGaAsP/InP DFB lasers', *J. Lightwave Technol.*, **LT-5**(11), pp. 1564–1573, 1987.

[38] T-P. Lee and C. Zah, 'Wavelength-tunable and single-frequency semiconductor lasers for photonic communications networks', *IEEE Commun. Mag.*, pp. 42–51, October 1989.

[39] P. A. Kirby, 'Semiconductor laser sources for optical communications', *Radio Electron. Eng., J IERE*, **51**(7/8), pp. 363–376, 1981.

[40] D. Botez and G. J. Herskowitz, 'Components for optical communications systems: a review', *Proc., IEEE*, **68**(6), pp. 689–730, 1980.

[41] H. C. Casey, 'Temperature dependence of the threshold current density in InP-$Ga_{0.28}In_{0.72}As_{0.6}P_{0.4}$ (λ = 1.3 μm) double heterostructure lasers', *J. Appl. Phys.*, **56**, p. 1959, 1984.

[42] D. H. Newman and S. Ritchie, 'Sources and detectors for optical fibre communications applications: the first 20 years', *IEE Proc., Pt. J*, **133**(3), pp. 213–229, 1986.

[43] T. Ikegami, 'Spectrum broadening and tailing effect in direct-modulated injection lasers', *Proceedings of 1st European Conference on Optical Fiber Communication* (London, UK), p. 111, 1975.

[44] K. Furuya, Y. Suematsu and T. Hong, 'Reduction of resonance like peak in direct modulation due to carrier diffusion in injection laser', *Appl. Opt.*, 17(12), pp. 1949–1952, 1978.

[45] P. M. Boers, M. T. Vlaardingerbroek and M. Danielson, 'Dynamic behaviour of semiconductor lasers', *Electron. Lett.*, **11**(10), pp. 206–208, 1975.

[46] D. J. Channin, 'Effect of gain saturation on injection laser switching', *J. Appl. Phys.*, **50**(6), pp. 3858–3860, 1979

[47] N. Chinane, K. Aiki, M. Nakamura and R. Ito, 'Effects of lateral mode and carrier density profile on dynamic behaviour of semiconductor lasers', *IEEE J. Quantum Electron.*, **QE-14**, pp. 625–631, 1977.

[48] R. S. Tucker, A. H. Gnauck, J. M. Wiesenfield and J. E. Bowers, '8 Gb/s return to zero modulation of a semiconductor laser by gain switching', *Internet. Conf. on Integrated Optics and Optical Fiber Commun. Technical Digest Series 1987 (OSA)*, **3**, p. 178, 1987.

[49] R. A. Linke, 'Modulation induced transient chirping in single frequency lasers', *IEEE J. Quantum Electron.*, **QE-21**, pp. 593–597, 1985.

[50] J. C. Cartledge and G. S. Burley, 'The effect of laser chirping on lightwave system performance', *J. Lightwave Technol.*, **7**(3), pp. 568–573, 1989.

[51] P. S. Henry, R. A. Linke and A. H. Gnauck, 'Introduction to lightwave systems', in S. E. Miller and I. P. Kaminow (Eds.) *Optical Fiber Telecommunications II*, Academic Press, pp. 781–831, 1988.

[52] L. Bickers and L. P. Westbrook, 'Reduction in laser chirp in 1.5 μm DFB lasers by modulation pulse shaping', *Electron. Lett.*, **21**, pp. 103–104, 1985.

[53] M. Yamaguchi, K. Emura, M. Kitamura, I. Mito and K. Kobayashi, 'Frequency chirping suppression by a distributed-feedback laser diode and a monolithically integrated loss modulator', *Technical Digest of Optical Fiber Commun. Conf., OFC '85* (USA), paper WI3, 1985.

[54] G. Arnold, P. Russer and K. Peterman, 'Modulation of laser diodes', in H. Kressel (Ed.), *Semiconductor Devices for Optical Communication, Topics in Applied Physics*, **39**, pp. 213–242, 1985.

[55] J. Saltz, 'Modulation and detection for coherent lightwave communications', *IEEE Commun. Mag.*, **24**(6), pp. 38–49, 1986.

[56] F. G. Walther and J. E. Kaufmann, 'Characterization of GaAlAs laser diode frequency noise', *Sixth Top. Mtg. Opt. Fiber Commun.* (USA), paper TUJ5, 1983.

[57] Y. Suematsu and T. Hong, 'Suppression of relaxation oscillations in light output of injection lasers by electrical resonance circuit', *IEEE J. Quantum. Electron.*, **QE-13**(9), pp. 756–762, 1977.

[58] C. H. Henry, 'Phase noise in semiconductor lasers', *J. Lightwave Technol.*, **LT-4**(3), pp. 298–310, 1986.

[59] C. H. Henry and R. F. Kazarinov, 'Instability of semiconductor lasers due to optical feedback from distant reflectors', *IEEE J. Quantum. Electron.*, **QE-22**, pp. 294–301, 1986.

[60] S. D. Personick, *Fiber Optic Technology and Applications*, Plenum Press, 1985.
[61] K. Ogawa, 'Analysis of mode partition noise in laser transmission systems', *IEEE J. Quantum. Electron.*, **QE-18**, pp. 849–855, 1982.
[62] F. R. Nash, W. J. Sundberg, R. L. Hartman, J. R. Pawlik, D. A. Ackerman, N. K. Dutta and R. W. Dixon, 'Implementation of the proposed reliability assurance strategy for an InGaAsP/InP planar mesa B H laser for use in a submarine cable', *AT&T Tech. J.*, **64**, p. 809, 1985.
[63] N. K. Dutta and C. L. Zipfel, 'Reliability of lasers and LEDs', in S. E. Miller and I. P. Kaminow (Eds.) *Optical Fiber Telecommunications II*, Academic Press, pp. 671–687, 1988.
[64] H. Kogelnik, 'Devices for optical communications', *Solid State Devices Research Conf. (ESSDERC)* and *4th Symposium on Solid Device Technology* (Munich, W. Germany), **53**, pp. 1–19, 1980.
[65] T. Yamamoto, K. Sakai and S. Akiba, '10000-h continuous CW operation of $In_{1-x}Ga_xAs_yP_{1-y}$/InP DH lasers at room temperature', *IEEE J. Quantum Electron.*, **QE-15**(8), pp. 684–687, 1979.
[66] M. Hirao, K. Mizuishi and M. Nakamura, 'High-reliability semiconductor lasers for optical communications', *IEEE J. on Selected Areas in Commun.*, **SAC-4**(9), pp. 1494–1501, 1986.
[67] I. W. Marshall, 'Low loss coupling between semiconductor lasers and single-mode fibre using tapered lensed fibres', *Br. Telecom Technol. J.*, **4**(2), pp. 114–121, 1986.
[68] H. Kawahara, Y. Onada, M. Goto and T. Nakagami, 'Reflected light in the coupling of semiconductor lasers with tapered hemispherical end fibres', *Appl. Opt.*, **22**, pp. 2732–2738, 1983.
[69] H. Kawahara, M. Sasaki and N. Tokoyo, 'Efficient coupling from semiconductor lasers into single-mode fibres with tapered hemispherical ends', *Appl. Opt.*, **19**, pp. 2578–2583, 1980.
[70] T. Schwander, B. Schwaderer and H. Storm, 'Coupling of lasers to single-mode fibres with high efficiency and low optical feedback', *Electron. Lett.*, **21**, pp. 287–289, 1985.
[71] J. Lipson, R. T. Ku and R. E. Scotti, 'Opto-mechanical considerations for laser-fiber coupling and packaging', *Proc. SPIE Int. Soc. Opt. Eng. (USA)*, **5543**, pp. 308–312, 1985.
[72] R. T. Ku, 'Progress in efficient/reliable semiconductor laser-to-single mode fiber coupler development', *Conf. on Opt. Fiber Commun.* (Washington DC, USA), *Tech. Dig.* pp. 4–6, January 1984.
[73] G. D. Khoe, H. G. Kock, D. Kuppers, J. H. F. M. Poulissen and H. M. DeVrieze, 'Progress in monomode optical fiber interconnection devices', *J. of Lightwave Technol.*, **LT-2**(3), pp. 217–227, 1984.
[74] P. Urquhart, 'Review of rare earth doped fiber lasers and amplifiers', *IEE Proc., Pt. J. Optoelectronics*, **135**(6), pp. 385–407, 1988.
[75] J. Wilson and J. F. B. Hawkes, *Lasers: Principles and applications*, Prentice Hall, 1987.
[76] K. Patek, *Glass Lasers*, Butterworth, 1970.
[77] R. M. MacFarlane and R. M. Shelby, 'Coherent transient and holeburning spectroscopy of rare earth ions in solids', in R. M. MacFarlane and A. A. Kaplyanskii (Eds.), *Spectroscopy of Solids Containing Rare Earth Ions*, North-Holland, pp. 51–184, 1987.

[78] C. A. Millar, M. C. Brierley and P. W. France, 'Optical amplification in an erbium-doped fluorozirconate fibre between 1480 nm and 1600 nm', *Fourteenth European Conf. on Optical Commun., ECOC '88 (UK), IEE Conf. Pub.*, **292**, Pt. 1, pp. 66–69, 1988.
[79] M. Shimitzu, H. Suda and M. Horiguchi, 'High efficiency Nd-doped fibre lasers using direct-coated dielectric mirrors', *Electron. Lett.*, **23**, pp. 768–769, 1987.
[80] D. N. Payne and L. Reekie, 'Rare-earth-doped fibre lasers and amplifiers', *Fourteenth European Conf. on Optical Commun., ECOC '88, (UK), IEE Conf. Pub.*, **292**, Pt. 1, pp. 49–51, 1988.
[81] L. F. Stokes, M. Chodorow and H. J. Shaw, 'All single-mode fibre resonator', *Opt. Lett.*, **7**, p. 288, 1982.
[82] I. D. Miller, D. B. Mortimore, P. Urquhart, B. J. Ainslie, S. P. Craig, C. A. Millar and D. B. Payne, 'A Nd^{3+}-doped CW fibre laser using all-fibre reflectors', *Appl. Opt.*, **26**, pp. 2197–2201, 1987.
[83] I. D. Miller, D. B. Mortimore, B. J. Ainslie, P. Urquhart, S. P. Craig, C. A. Millar and D. B. Payne, 'New all-fiber laser', *Opt. Fiber Commun. Conf., OFC '87* (USA), January 1987.
[84] P. Urquhart, 'Transversely coupled fibre Fabry–Perot resonator: theory', *Appl. Opt.*, **26**, pp. 456–463, 1987.
[85] K. Kobayashi and I. Mito, 'Single frequency and tunable laser diodes', *J. Lightwave Technol.*, **6**(11), pp. 1623–1633, 1988.
[86] C. H. Henry, 'Theory of the linewidth of semiconductor lasers', *IEEE J. Quantum Electron.*, **QE-18**, pp. 259–264, 1982.
[87] R. Wyatt and W. J. Devlin, '10-kHz linewidth 1.5-μm InGaAsP external cavity laser with 55-nm tuning range', *Electron. Lett.*, **19**, pp. 110–112, 1983.
[88] N. A. Olsson and J. P. van der Ziel, 'Performance characteristics of 1.5 micron external cavity semiconductor lasers for coherent optical communication', *J. Lightwave Technol.*, **LT-5**, pp. 510–515, 1987.
[89] W. V. Severin and H. J. Shaw, 'A single-mode fiber evanescent grating reflector', *J. Lightwave Technol.*, **LT-3**, pp. 1041–1048, 1985.
[90] J. Wittmann and G. Gaukel, 'Narrow-linewidth laser with a prism grating: GRINrod lens combination serving an external cavity', *Electron. Lett.*, **23**, pp. 524–525, 1987.
[91] F. Heismann, R. C. Alferness, L. L. Buhl, G. Eisenstein, S. K. Korotky, J. J. Veselka, L. W. Stulz and C. A. Burrus, 'Narrow-linewidth, electro-optically tunable InGaAsP–Ti : $LiNbO_3$ extended cavity laser', *Appl. Phys. Lett.*, **51**, pp. 164–165, 1987.
[92] G. Coquin, K. W. Cheung and M. M. Choy, 'Single and multiple wavelength operation of acousto-optically tuned semiconductor lasers at 1.3 microns', *Proc. 11th IEEE Int. Semiconductor Laser Conf.* (USA), pp. 130–131, 1988.
[93] G. Coquin and K. W. Cheung, 'An electronically tunable external cavity semiconductor laser', *Electron. Lett.*, **24**, pp. 599–600, 1988.
[94] N. K. Dutta, T. Cella, A. B. Piccirilli, R. L. Brown, 'Integrated external cavity lasers', *Conf. on Lasers and Electrooptics, CLEO '87* (USA), MF2, April 1987.
[95] Y. Suematsu and S. Arai, 'Integrated optics approach for advanced semiconductor lasers', *Proc. IEEE*, **75**(11), pp. 1472–1487, 1987.
[96] M. Okai, S. Sakano and N. Chinone, 'Wide-range continuous tunable double-sectioned distributed feedback lasers', *Fifteenth European Conf. on Opt. Commun.* (Sweden) pp. 122–125, September, 1989.

[97] H. Imai, 'Tuning results of 3-sectioned DFB lasers', *Semiconductor Laser Workshop, Conf. on Lasers and Electrooptics, CLEO '89* (USA), 1989.

[98] S. Murata, I. Mito and K. Kobayashi, 'Tuning ranges for 1.5 μm wavelength tunable DBR lasers', *Electron. Lett.*, **24**, pp. 577–579, 1988.

[99] Y. Kotaki, M. Matsuda, H. Ishikawa and H. Imni, 'Tunable DBR laser with wide tuning range', *Electron. Lett.*, **24**, pp. 503–505, 1988.

[100] I. M. Jauncey, L. Reekie, J. E. Townsend and D. N. Payne, 'Single longitudinal-mode operation of an Nd^{3+}-doped fibre laser', *Electron. Lett.*, **24**, pp. 24–26, 1988.

[101] L. Reekie, R. J. Mears, S. B. Poole and D. N. Payne, 'Tunable single-mode fibre lasers', *J. Lightwave Technol.*, **LT-4**(7), pp. 956–960, 1986.

[102] C. A. Millar, I. D. Miller, D. B. Mortimore, B. J. Ainslie and P. Urquhart, 'Fibre laser with adjustable fibre reflector for wavelength tuning and variable output coupling', *IEE Proc., Part J*, **135**, pp. 303–304, 1988.

[103] G. H. B. Thompson, *Physics of Semiconductor Laser Devices*, John Wiley, 1980.

[104] Y. Horikoshi, 'Semiconductor lasers with wavelengths exceeding 2 μm', in W. T. Tsang (Vol. Ed.) *Semiconductors and Semimetals: Lightwave communication technology*, Academic Press, 22C, pp. 93–151, 1985.

[105] C. Caneau, A. K. Srivastava, A. G. Dentai, J. L. Zyskind and M. A. Pollack, 'Room temperature GaInAsSb/AlGaAsSb DH injection lasers at 2.2 μm', *Electron. Lett.*, **21**, pp. 815–817, 1985.

[106] A. E. Bockarev, L. M. Dolginov, A. E. Drakin, L. V. Druzhinina, P. G. Eliseev and B. N. Sverdlov, 'Injection InGaAsSb lasers emitting radiation of wavelengths 1.2–2.3 μm at room temperature', *Sov. J. Quantum Electron.*, **15**, pp. 869–870, 1985.

[107] C. Caneau, J. L. Zyskind, J. W. Sulhoff, T. E. Glover, J. Centanni, C. A. Burrus, A. G. Dentai and M. A. Pollack, '2.2 μm GaInAsSb/AlGaAsSb injection lasers with low threshold current density', *Appl. Phys. Lett.*, **51**, pp. 764–766, 1987.

[108] H. Ebe, Y. Nishijima and K. Shinohara, 'PbEuTe lasers with 4–6 μm wavelength mode with hot-well epitaxy', *IEEE J. Quantum Electron.*, **25**(6), pp. 1381–1384, 1989.

[109] M. C. Brierley and P. W. France, 'Continuous wave lasing at 2.7 μm in an erbium-doped fluorozirconate fibre', *Electron. Lett.*, **24**, pp. 935–937, 1988.

[110] M. C. Brierley, P. W. France and C. A. Millar, 'Lasing at 2.08 μm in a holmium-doped fluorozirconate fibre laser', *Electron. Lett.*, **24**, pp. 539–540, 1988.

[111] L. Esterowitz, R. Allen and I. Aggarwal, 'Pulsed laser emission at 2.3 μm in a thulium-doped fluorozirconate fibre', *Electron. Lett.*, **24**, p. 1104, 1988.

[112] R. W. Tkach and A. R. Chaplyry, 'Phase noise and linewidth in an InGaAsP laser', *J. Lightwave Technol.*, **LT-4**, pp. 1711–1716, 1986.

[113] T.-P. Lee, 'Recent advances in long-wavelength semiconductor lasers for optical fiber communication', *Proc. IEEE*, **79**(3), pp. 253–276, 1991.

7

Optical sources 2: The light emitting diode

7.1 Introduction
7.2 LED power and efficiency
7.3 LED structures
7.4 LED characteristics
7.5 Modulation
Problems
References

7.1 Introduction

Spontaneous emission of radiation in the visible and infrared regions of the spectrum from a forward biased *p–n* junction was discussed in Section 6.3.2. The normally empty conduction band of the semiconductor is populated by electrons injected into it by the forward current through the junction, and light is generated when these electrons recombine with holes in the valence band to emit a photon. This is the mechanism by which light is emitted from an LED, but stimulated emission is not encouraged, as it is in the injection laser, by the addition of an optical cavity and mirror facets to provide feedback of photons.

The LED can therefore operate at lower current densities than the injection laser, but the emitted photons have random phases and the device is an incoherent optical source. Also, the energy of the emitted photons is only roughly equal to the bandgap energy of the semiconductor material, which gives a much wider spectral

linewidth (possibly by a factor of 100) than the injection laser. The linewidth for an LED corresponds to a range of photon energy between 1 and 3.5 KT, where K is Boltzmann's constant and T is the absolute temperature. This gives linewidths of 30 to 40 nm for GaAs-based devices operating at room temperature. Thus the LED supports many optical modes within its structure and is therefore often used as a multimode source, although more recently the coupling of LEDs to single-mode fibers has been pursued with success, particularly when advanced structures have been employed. At present, LEDs have several further drawbacks in comparison with injection lasers. These include:

(a) generally lower optical power coupled into a fiber (microwatts);
(b) usually lower modulation bandwidth;
(c) harmonic distortion.

However, although these problems may initially appear to make the LED a less attractive optical source than the injection laser, the device has a number of distinct advantages which have given it a prominent place in optical fiber communications:

1. *Simpler fabrication*. There are no mirror facets and in some structures no striped geometry.
2. *Cost*. The simpler construction of the LED leads to much reduced cost which is always likely to be maintained.
3. *Reliability*. The LED does not exhibit catastrophic degradation and has proved far less sensitive to gradual degradation than the injection laser. It is also immune to self pulsation and modal noise problems.
4. *Generally less temperature dependence*. The light output against current characteristic is less affected by temperature than the corresponding characteristic for the injection laser. Furthermore, the LED is not a threshold device and therefore raising the temperature does not increase the threshold current above the operating point and hence halt operation.
5. *Simpler drive circuitry*. This is due to the generally lower drive currents and reduced temperature dependence which makes temperature compensation circuits unnecessary.
6. *Linearity*. Ideally, the LED has a linear light output against current characteristic (see Section 7.4.1), unlike the injection laser. This can prove advantageous where analog modulation is concerned.

These advantages combined with the development of high radiance, relatively high bandwidth devices have ensured that the LED remains an extensively used source for optical fiber communications.

Structures fabricated using the GaAs/AlGaAs material system are well tried for operation in the shorter wavelength region. In addition, more recently there have been substantial advances in devices based on the InGaAsP/InP material structure for use in the longer wavelength region especially around 1.3 μm. At this wavelength, the material dispersion in silica glass fibers goes through zero and hence the wider linewidth of the LED imposes a far slighter limitation on link length than

does intermodal dispersion within multimode fiber. Furthermore, the reduced fiber attenuation at this operating wavelength can allow longer-haul LED systems.

Although longer wavelength LED systems using multimode graded index fiber are continuing to be developed, particularly for nontelecommunication applications (see Sections 14.5 to 14.7), much recent activity has been concerned with both high speed operation and with the coupling of these InGaAsP LEDs to single-mode fiber. A major impetus for these strategies is the potential deployment of such single-mode LED systems in the telecommunication access network or subscriber loop (see Section 14.2.3). In this context, theoretical studies of both LED coupling [Ref. 1] and transmission [Ref. 2] with single-mode fiber have been undertaken, as well as numerous practical investigations, some of which are outlined in the following sections. It is therefore apparent that LEDs are likely to remain a prominent optical fiber communication source for many system applications including operation over significant distances with single-mode fiber at transmission rates that may exceed a Gbit s^{-1}.

Structures fabricated using the GaAs/AlGaAs material system are well advanced for the shorter wavelength region. There has also been much interest in LEDs for the longer wavelength region, especially around 1.3 μm where material dispersion in silica-based fibers goes through zero and where the wide linewidth of the LED imposes far less limitation on link length than intermodal dispersion within the fiber. Furthermore, the reduced attenuation allows longer-haul LED systems. As with injection lasers InGaAsP/InP is the material structure currently favoured in this region for the high radiance devices. These longer wavelength systems utilizing graded index fibers have led to the development of wider bandwidth devices providing transmission rates of hundreds of Mbit s^{-1}.

LEDs therefore remain the primary optical source for nontelecommunication applications (i.e. shorter-haul) whilst injection lasers find major use as single-mode devices within single-mode fiber systems for long-haul, wideband applications. In addition, LEDs have been shown to launch acceptable, albeit often modest (5 to 10 μW) levels of optical power into single-mode fiber and therefore may well find use in short-haul single-mode fiber telecommunication systems (i.e. the subscriber loop) in the future.

Having dealt with the basic operating principles for the LED in Section 6.3.2, we continue in Section 7.2 with a discussion of LED power and efficiency in relation to the launching of light into optical fibers. Moreover, at the end of this section we include a brief account of the operation of an efficient LED which employs a double heterostructure. This leads into a discussion in Section 7.3 of the major practical LED structures where again we have regard to their light coupling efficiency. Also included in this section are the more advanced device structures such as the edge-emitting and the superluminescent LED. The various operating characteristics and limitations on LED performance are then described in Section 7.4. Finally in Section 7.5, we include a brief discussion on the possible modulation techniques for semiconductor optical sources.

7.2 LED power and efficiency

The absence of optical amplification through stimulated emission in the LED tends to limit the internal quantum efficiency (ratio of photons generated to injected electrons) of the device. Reliance on spontaneous emission allows nonradiative recombination to take place within the structure due to crystalline imperfections and impurities giving, at best, an internal quantum efficiency of 50% for simple homojunction devices. However, as with injection lasers double heterojunction (DH) structures have been implemented which recombination lifetime measurements suggest [Ref. 3] give internal quantum efficiencies of 60 to 80%.

The power generated internally by an LED may be determined by consideration of the excess electrons and holes in the p and n type material respectively (i.e. the minority carriers) when it is forward biased and carrier injection takes place at the device contacts (see Section 6.3.2). The excess density of electrons Δn and holes Δp is equal since the injected carriers are created and recombined in pairs such that charge neutrality is maintained within the structure. In extrinsic materials one carrier type will have a much higher concentration than the other and hence in the p type region, for example, the hole concentration will be much greater than the electron concentration. Generally, the excess minority carrier density decays exponentially with time t [Ref. 4] according to the relation:

$$\Delta n = \Delta n(0) \exp(-t/\tau) \qquad (7.1)$$

where $\Delta n(0)$ is the initial injected excess electron density and τ represents the total carrier recombination lifetime. In most cases, however, Δn is only a small fraction of the majority carriers and comprises all of the minority carriers. Therefore, in these cases, the carrier recombination lifetime becomes the minority or injected carrier lifetime τ_i.

When there is a constant current flow into the junction diode, an equilibrium condition is established. In this case, the total rate at which carriers are generated will be the sum of the externally supplied and the thermal generation rates. The current density J in amperes per square metre may be written as J/ed in electrons per cubic metre per second, where e is the charge on an electron and d is the thickness of the recombination region. Hence a rate equation for carrier recombination in the LED can be expressed in the form [Ref. 4]:

$$\frac{d(\Delta n)}{dt} = \frac{J}{ed} - \frac{\Delta n}{\tau} \qquad (\mathrm{m}^{-3}\,\mathrm{s}^{-1}) \qquad (7.2)$$

The condition for equilibrium is obtained by setting the derivative in Eq. (7.2) to zero. Hence

$$\Delta n = \frac{J\tau}{ed} \qquad (\mathrm{m}^{-3}) \qquad (7.3)$$

Equation (7.3) therefore gives the steady state electron density when a constant current is flowing into the junction region.

It is also apparent from Eq. (7.2) that in the steady state the total number of carrier recombinations per second or the recombination rate r_t will be:

$$r_t = \frac{J}{ed} \quad (\text{m}^{-3}) \tag{7.4}$$

$$= r_r + r_{nr} \quad (\text{m}^{-3}) \tag{7.5}$$

where r_r is the radiative recombination rate per unit volume and r_{nr} is the nonradiative recombination rate per unit volume. Moreover, when the forward biased current into the device is i, then from Eq. (7.4) the total number of recombinations per second R_t becomes:

$$R_t = \frac{i}{e} \tag{7.6}$$

It was indicated in Section 6.3.3.1 that excess carriers can recombine either radiatively or nonradiatively. Whilst in the former case a photon is generated, in the latter case the energy is released in the form of heat (i.e. lattice vibrations). Moreover, for a DH device with a thin active region (a few μm), then the nonradiative recombination tends to be dominated by surface recombination at the heterojunction interfaces.

The LED internal quantum efficiency* η_{int}, which can be defined as the ratio of the radiative recombination rate to the total recombination rate, following Eq. (7.5) may be written as [Ref. 5]:

$$\eta_{int} = \frac{r_r}{r_t} = \frac{r_r}{r_r + r_{nr}} \tag{7.7}$$

$$= \frac{R_r}{R_t} \tag{7.8}$$

where R_r is the total number of *radiative* recombinations per second. Rearranging Eq. (7.8) and substituting from Eq. (7.6) gives:

$$R_r = \eta_{int} \frac{i}{e} \tag{7.9}$$

Since R_r is also equivalent to the total number of photons generated per second and from Eq. (6.1) each photon has an energy equal to hf joules, then the optical power

* The internal quantum efficiency for the LED is obtained only from the spontaneous radiation and hence is written as η_{int}. By contrast, the internal quantum efficiency for the injection laser combined the internal quantum efficiencies for both spontaneous and simulated radiation. It was therefore denoted as η_i (see Section 6.4.1).

generated internally by the LED, P_{int} is:

$$P_{int} = \eta_{int} \frac{i}{e} hf \qquad \text{(W)} \tag{7.10}$$

Using Eq. (6.22) to express the internally generated power in terms of wavelength rather than frequency gives:

$$P_{int} = \eta_{int} \frac{hci}{e\lambda} \qquad \text{(W)} \tag{7.11}$$

It is interesting to note that Eqs. (7.10) and (7.11) display a linear relationship between the optical power generated in the LED and the drive current into the device (see Section 7.4.1). Similar relationships may be obtained for the optical power emitted from an LED but in this case the constant of proportionality η_{int} must be multiplied by a factor representing the external quantum efficiency* η_{ext} to provide an overall quantum efficiency for the device.

For the exponential decay of excess carriers depicted by Eq. (7.1) the radiative minority carrier lifetime is $\tau_r = \Delta n/r_r$ and the nonradiative minority carrier lifetime is $\tau_{nr} = \Delta n/r_{nr}$. Therefore, from Eq. (7.7) the internal quantum efficiency is:

$$\eta_{int} = \frac{1}{1 + (r_{nr}/r_r)} = \frac{1}{1 + (\tau_r/\tau_{nr})} \tag{7.12}$$

Furthermore, the total recombination lifetime τ can be written as $\tau = \Delta n/r_t$ which, using Eq. (7.5), gives:

$$\frac{1}{\tau} = \frac{1}{\tau_r} + \frac{1}{\tau_{nr}} \tag{7.13}$$

Hence Eq. (7.12) becomes

$$\eta_{int} = \frac{\tau}{\tau_r} \tag{7.14}$$

It should be noted that the same expression for the internal quantum efficiency could be obtained from Eq. (7.7).

Example 7.1

The radiative and nonradiative recombination lifetimes of the minority carriers in the active region of a double heterojunction LED are 60 ns and 100 ns respectively. Determine the total carrier recombination lifetime and the power internally generated within the device when the peak emission wavelength is 0.87 μm at a drive current of 40 mA.

* The external quantum efficiency may be defined as the ratio of the photons emitted from the device to the photons internally generated. However, it is sometimes defined as the ratio of the number of photons emitted to the total number of carrier recombinations (radiative and nonradiative).

Solution: The total carrier recombination lifetime is given by Eq. (7.13) as:

$$\tau = \frac{\tau_r \tau_{nr}}{\tau_r + \tau_{nr}} = \frac{60 \times 100 \text{ ns}}{(60 + 100)} = 37.5 \text{ ns}$$

To calculate the power internally generated it is necessary to obtain the internal quantum efficiency of the device. Hence using Eq. (7.14):

$$\eta_{int} = \frac{\tau}{\tau_r} = \frac{37.5}{60} = 0.625$$

Thus from Eq (7.11):

$$P_{int} = \eta_{int} \frac{hci}{e\lambda} = \frac{0.625 \times 6.626 \times 10^{-34} \times 2.998 \times 10^{8} \times 40 \times 10^{-3}}{1.602 \times 10^{-19} \times 0.87 \times 10^{-6}}$$

$$= 35.6 \text{ mW}$$

The LED which has an internal quantum efficiency of 62.5% generates 35.6 mW of optical power, internally. It should be noted, however, that this power level will not be readily emitted from the device.

Although the possible internal quantum efficiency can be relatively high the radiation geometry for an LED which emits through a planar surface is essentially Lambertian in that the surface radiance (the power radiated from a unit area into a unit solid angle, given in $\text{W sr}^{-1}\text{m}^{-2}$) is constant in all directions. The Lambertian intensity distribution is illustrated in Figure 7.1 where the maximum intensity I_0 is perpendicular to the planar surface but is reduced on the sides in proportion to the cosine of the viewing angle θ as the apparent area varies with this angle. This reduces the external power efficiency to a few per cent as most of the light generated within the device is trapped by total internal reflection (see Section 2.2.1) when it is radiated at greater than the critical angle for the crystal–air

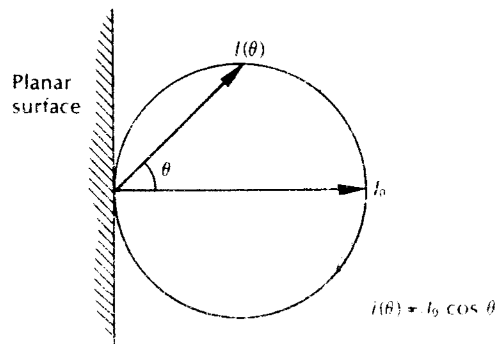

Figure 7.1 The Lambertian intensity distribution typical of a planar LED.

interface. As with the injection laser (see Section 6.4.1) the external power efficiency η_{ep} is defined as the ratio of the optical power emitted externally P_e to the electrical power provided to the device P or:

$$\eta_{ep} \simeq \frac{P_e}{P} \times 100\% \tag{7.15}$$

Also, the optical power emitted P_e into a medium of low refractive index n from the face of a planar LED fabricated from a material of refractive index n_x is given approximately by [Ref. 6]:

$$P_e = \frac{P_{int} F n^2}{4 n_x^2} \tag{7.16}$$

where P_{int} is the power generated internally and F is the transmission factor of the semiconductor–external interface. Hence it is possible to estimate the percentage of optical power emitted.

Example 7.2

A planar LED is fabricated from gallium arsenide which has a refractive index of 3.6.

(a) Calculate the optical power emitted into air as a percentage of the internal optical power for the device when the transmission factor at the crystal–air interface is 0.68.

(b) When the optical power generated internally is 50% of the electrical power supplied, determine the external power efficiency.

Solution: (a) The optical power emitted is given by Eq. (7.16), in which the refractive index n for air is 1.

$$P_e \simeq \frac{P_{int} F n^2}{4 n_x^2} = \frac{P_{int} 0.68 \times 1}{4(3.6)^2} = 0.013 P_{int}$$

Hence the power emitted is only 1.3% of the optical power generated internally.

(b) The external power efficiency is given by Eq. (7.15), where

$$\eta_{ep} = \frac{P_e}{P} \times 100 = 0.013 \frac{P_{int}}{P} \times 100$$

Also, the optical power generated internally $P_{int} = 0.5P$.

Hence

$$\eta_{ep} = \frac{0.013 P_{int}}{2 P_{int}} \times 100 = 0.65\%$$

A further loss is encountered when coupling the light output into a fiber. Considerations of this coupling efficiency are very complex; however, it is possible to use an approximate simplified approach [Ref. 7]. If it is assumed for step index fibers that all the light incident on the exposed end of the core within the acceptance angle θ_a is coupled, then for a fiber in air, using Eq. (2.8):

$$\theta_a = \sin^{-1}(n_1^2 - n_2^2)^{\frac{1}{2}} = \sin^{-1}(NA) \tag{7.17}$$

Also, incident light at angles greater than θ_a will not be coupled. For a Lambertian source, the radiant intensity at an angle θ, $I(\theta)$ is given by (see Figure 7.1):

$$I(\theta) = I_0 \cos\theta \tag{7.18}$$

where I_0 is the radiant intensity along the line $\theta = 0$. Considering a source which is smaller than, and in close proximity to, the fiber core, and assuming cylindrical symmetry, the coupling efficiency η_c is given by:

$$\eta_c = \frac{\int_0^{\theta_a} I(\theta)\sin\theta\, d\theta}{\int_0^{\pi/2} I(\theta)\sin\theta\, d\theta} \tag{7.19}$$

Hence substituting from Eq. (7.18):

$$\eta_c = \frac{\int_0^{\theta_a} I_0\cos\theta\sin\theta\, d\theta}{\int_0^{\pi/2} I_0\cos\theta\sin\theta\, d\theta}$$

$$= \frac{\int_0^{\theta_a} I_0\sin 2\theta\, d\theta}{\int_0^{\pi/2} I_0\sin 2\theta\, d\theta}$$

$$\eta_c = \frac{[-I_0\cos 2\theta/2]_0^{\theta_a}}{[-I_0\cos 2\theta/2]_0^{\pi/2}}$$

$$= \sin^2\theta_a \tag{7.20}$$

Furthermore, from Eq. (7.17):

$$\eta_c = \sin^2\theta_a = (NA)^2 \tag{7.21}$$

Equation (7.21) for the coupling efficiency allows estimates for the percentage of optical power coupled into the step index fiber relative to the amount of optical power emitted from the LED.

Example 7.3

The light output from the GaAs LED of Example 7.2 is coupled into a step index

fiber with a numerical aperture of 0.2, a core refractive index of 1.4 and a diameter larger than the diameter of the device. Estimate:

(a) The coupling efficiency into the fiber when the LED is in close proximity to the fiber core.
(b) The optical loss in decibels, relative to the power emitted from the LED, when coupling the light output into the fiber.
(c) The loss relative to the internally generated optical power in the device when coupling the light output into the fiber when there is a small air gap between the LED and the fiber core.

Solution: (a) From Eq. (7.21), the coupling efficiency is given by:

$$\eta_c = (NA)^2 = (0.2)^2 = 0.04$$

Thus about 4% of the externally emitted optical power is coupled into the fiber.

(b) Let the optical power coupled into the fiber be P_c. Then the optical loss in decibels relative to P_e when coupling the light output into the fiber is

$$Loss = -10 \log_{10} \frac{P_c}{P_e}$$

$$= -10 \log_{10} \eta_c$$

Hence,

$$Loss = -10 \log_{10} 0.04$$
$$= 14.0 \text{ dB}$$

(c) When the LED is emitting into air, from Example 7.2:

$$P_e = 0.013 P_{int}$$

Assuming a very small air gap (i.e. cylindrical symmetry unaffected); then from (a) the power coupled into the fiber is:

$$P_c = 0.04 P_e = 0.04 \times 0.013 P_{int}$$
$$= 5.2 \times 10^{-4} \; P_{int}$$

Hence in this case only about 0.05% of the internal optical power is coupled into the fiber.

The loss in decibels relative to P_{int} is:

$$Loss = -10 \log_{10} \frac{P_c}{P_{int}} = -10 \log_{10} 5.2 \times 10^{-4} = 32.8 \text{ dB}$$

If significant optical power is to be coupled from an incoherent LED into a low NA fiber the device must exhibit very high radiance. This is especially the case when considering graded index fibers where the Lambertian coupling efficiency with the

same NA (same refractive index difference) and $\alpha \simeq 2$ (see Section 2.4.4) is about half that into step index fibers [Ref. 8]. To obtain the necessary high radiance, direct bandgap semiconductors (see Section 6.3.3.1) must be used fabricated with DH structures which may be driven at high current densities. The principle of operation of such a device will now be considered prior to discussion of various LED structures.

7.2.1 The double heterojunction LED

The principle of operation of the DH LED is illustrated in Figure 7.2. The device shown consists of a *p* type GaAs layer sandwiched between a *p* type AlGaAs

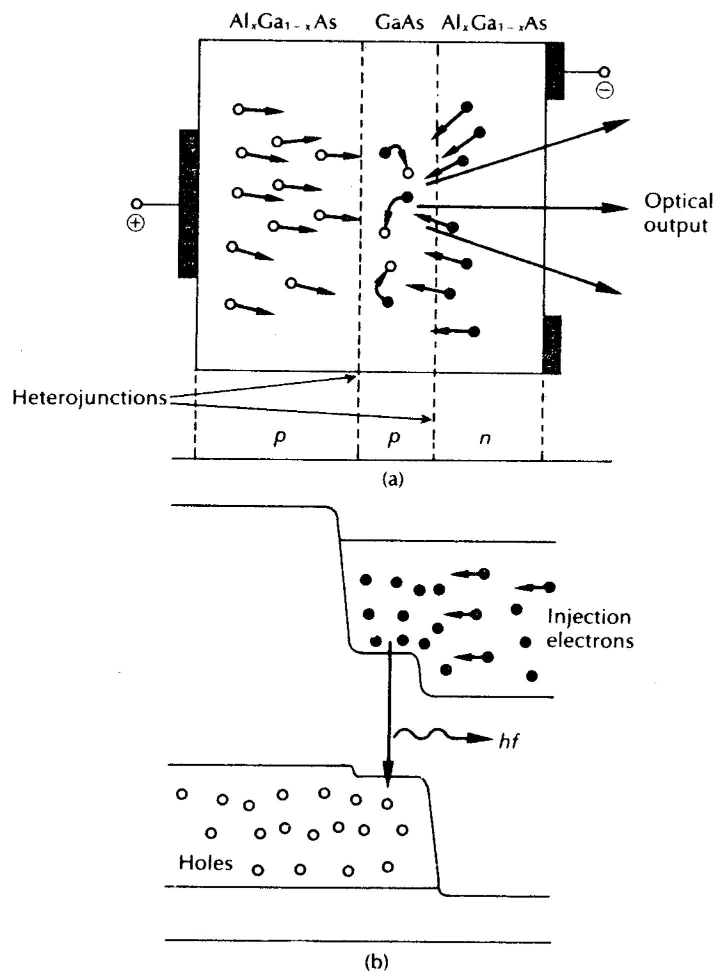

Figure 7.2 The double heterojunction LED: (a) the layer structure, shown with an applied forward bias; (b) the corresponding energy band diagram.

and an *n* type AlGaAs layer. When a forward bias is applied (as indicated in Figure 7.2(a)) electrons from the *n* type layer are injected through the *p–n* junction into the *p* type GaAs layer where they become minority carriers. These minority carriers diffuse away from the junction [Ref. 9], recombining with majority carriers (holes) as they do so. Photons are therefore produced with energy corresponding to the bandgap energy of the *p* type GaAs layer. The injected electrons are inhibited from diffusing into the *p* type AlGaAs layer because of the potential barrier presented by the *p–p* heterojunction (see Figure 7.2(b)). Hence, electroluminescence only occurs in the GaAs junction layer, providing both good internal quantum efficiency and high radiance emission. Furthermore, light is emitted from the device without reabsorption because the bandgap energy in the AlGaAs layer is large in comparison with that in GaAs. The DH structure is therefore used to provide the most efficient incoherent sources for application within optical fiber communications. Nevertheless, these devices generally exhibit the previously discussed constraints in relation to coupling efficiency to optical fibers. This and other LED structures are considered in greater detail in the following section.

7.3 LED structures

There are five major types of LED structure and although only two have found extensive use in optical fiber communications a third is becoming of increasing interest. These are the surface emitter, the edge emitter and the superluminescent LED respectively. The other two structures, the planar and dome LEDs, find more application as cheap plastic encapsulated visible devices for use in such areas as intruder alarms, TV channel changes and industrial counting. However, infrared versions of these devices have been used in optical communications mainly with fiber bundles and it is therefore useful to consider them briefly before progressing on to the high radiance LED structures.

7.3.1 Planar LED

The planar LED is the simplest of the structures that are available and is fabricated by either liquid- or vapour-phase epitaxial processes over the whole surface of a GaAs substrate. This involves a *p* type diffusion into the *n* type substrate in order to create the junction illustrated in Figure 7.3. Forward current flow through the junction gives Lambertian spontaneous emission and the device emits light from all surfaces. However, only a limited amount of light escapes the structure due to total internal reflection, as discussed in Section 7.2, and therefore the radiance is low.

7.3.2 Dome LED

The structure of a typical dome LED is shown in Figure 7.4. A hemisphere of *n* type GaAs is formed around a diffused *p* type region. The diameter of the dome is chosen to maximize the amount of internal emission reaching the surface within the

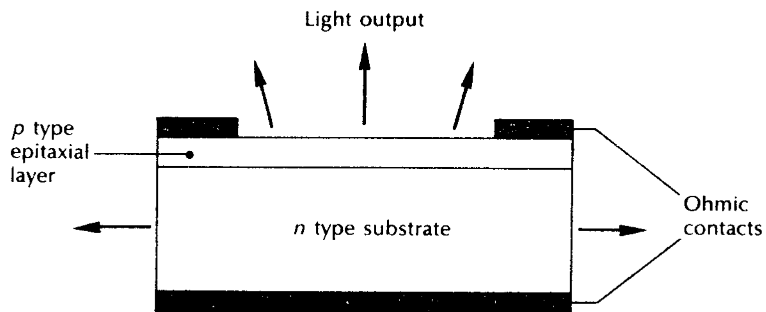

Figure 7.3 The structure of a planar LED showing the emission of light from all surfaces.

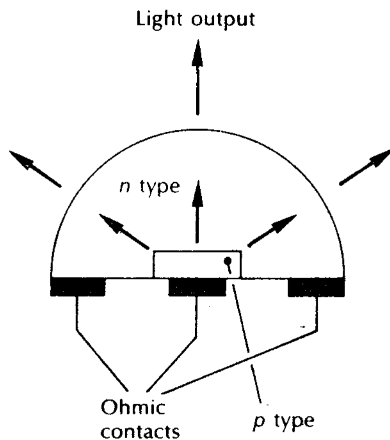

Figure 7.4 The structure of a dome LED.

critical angle of the GaAs–air interface. Hence this device has a higher external power efficiency than the planar LED. However, the geometry of the structure is such that the dome must be far larger than the active recombination area, which gives a greater effective emission area and thus reduces the radiance.

7.3.3 Surface emitter LEDs

A method for obtaining high radiance is to restrict the emission to a small active region within the device. The technique pioneered by Burrus and Dawson [Ref. 10] with homostructure devices was to use an etched well in a GaAs substrate in order to prevent heavy absorption of the emitted radiation, and physically to accommodate the fiber. These structures have a low thermal impedance in the active region allowing high current densities and giving high radiance emission into the optical fiber. Furthermore, considerable advantage may be obtained by employing

DH structures giving increased efficiency from electrical and optical confinement as well as less absorption of the emitted radiation. This type of surface emitter LED (SLED) is now widely employed within optical fiber communications.

The structure of a high radiance etched well DH surface emitter* for the 0.8 to 0.9 μm wavelength band is shown in Figure 7.5 [Ref. 11]. The internal absorption in this device is very low due to the larger bandgap confining layers, and the reflection coefficient at the back crystal face is high giving good forward radiance. The emission from the active layer is essentially isotropic, although the external emission distribution may be considered Lambertian with a beam width of 120° due to refraction from a high to a low refractive index at the GaAs–fiber interface. The power coupled P_c into a multimode step index fiber may be estimated from the relationship [Ref. 12]:

$$P_c = \pi(1 - r)AR_D(NA)^2 \tag{7.22}$$

where r is the Fresnel reflection coefficient at the fiber surface, A is the smaller of the fiber core cross section or the emission area of the source and R_D is the radiance of the source. However, the power coupled into the fiber is also dependent on many other factors including the distance and alignment between the emission area and the fiber, the SLED emission pattern and the medium between the emitting area and the fiber. For instance the addition of epoxy resin in the etched well tends to reduce the refractive index mismatch and increase the external power efficiency of the device. Hence, DH surface emitters often give more coupled optical power than

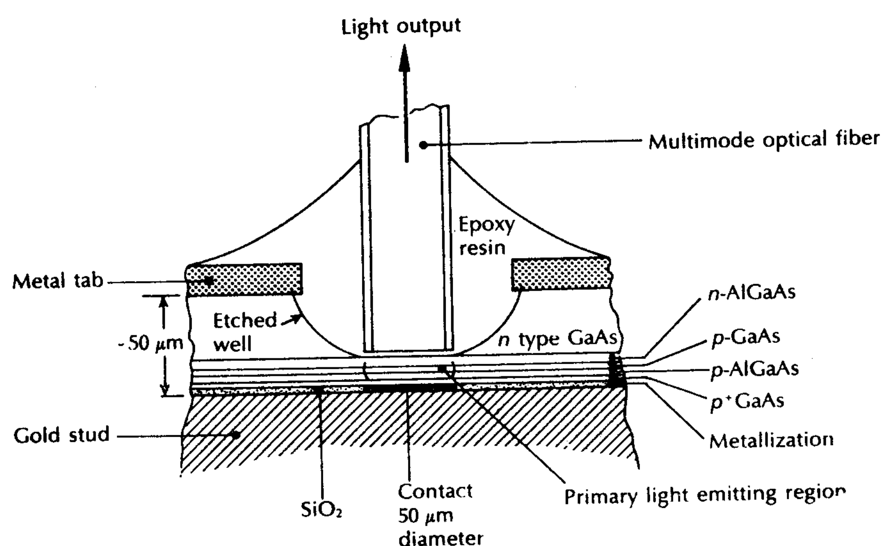

Figure 7.5 The structure of an AlGaAs DH surface-emitting LED (Burrus type) [Ref. 11]

* These devices are also known as Burrus type LEDs

predicted by Eq. (7.22). Nevertheless Eq. (7.22) may be used to gain an estimate of the power coupled, although accurate results may only be obtained through measurement.

Example 7.4

A DH surface emitter which has an emission area diameter of 50 μm is butt jointed to an 80 μm core step index fiber with a numerical aperture of 0.15. The device has a radiance of 30 $\text{W sr}^{-1}\text{cm}^{-2}$ at a constant operating drive current. Estimate the optical power coupled into the fiber if it is assumed that the Fresnel reflection coefficient at the index matched fiber surface is 0.01.

Solution: Using Eq. (7.22), the optical power coupled into the fiber P_c is given by:

$$P_c = \pi(1 - r)AR_D(NA)^2$$

In this case A represents the emission area of the source.

Hence:

$$A = \pi(25 \times 10^{-4})^2 = 1.96 \times 10^{-5}\ \text{cm}^2$$

Thus,

$$P_c = \pi(1 - 0.01)1.96 \times 10^{-5} \times 30 \times (0.15)^2$$
$$= 41.1\ \mu\text{W}$$

In this example around 41 μW of optical power is coupled into the step index fiber.

However, for graded index fiber optimum direct coupling requires that the source diameter be about one half the fiber core diameter. In both cases lens coupling may give increased levels of optical power coupled into the fiber but at the cost of additional complexity. Other factors which complicate the LED fiber coupling are the transmission characteristics of the leaky modes or large angle skew rays (see Section 2.4.1). Much of the optical power from an incoherent source is initially coupled into these large angle rays, which fall within the acceptance angle of the fiber but have much higher energy than meridional rays. Energy from these rays goes into the cladding and may be lost. Hence much of the light coupled into a multimode fiber from an LED is lost within a few hundred metres. It must therefore be noted that the effective optical power coupled into a short length of fiber significantly exceeds that coupled into a longer length.

The planar structure of the Burrus type LED and other nonetched well SLEDs [Ref. 13] allows significant lateral current spreading, particularly for contact diameters less than 25 μm. This current spreading results in a reduced current density as well as an effective emission area substantially greater than the contact area. A technique which has been used to reduce the current spreading in very small

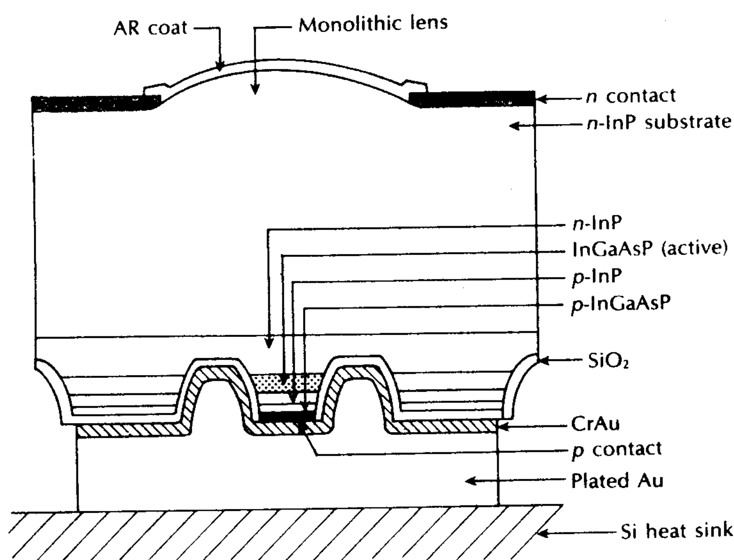

Figure 7.6 Small area InGaAsP mesa-etched surface-emitting LED structure [Ref. 14]

devices is to fabricate a mesa structure SLED, as illustrated in Figure 7.6 [Ref. 14]. In this case mesas with diameters in the range 20 to 25 μm at the active layer were formed by chemical etching.

These InGaAsP/InP devices which emitted at a wavelength of 1.3 μm had an integral lens formed at the exit face of the InP substrate in order to improve the coupling efficiency, particularly to single-mode fiber. Such monolithic lens structures provide a common strategy for improving the power coupled into fiber from LEDs, and alternative lens coupling techniques are discussed in Section 7.3.6. Moreover, there is increasing interest in coupling LEDs to single-mode fiber for shorter-haul applications which, in the case of SLEDs, necessitates efficient lens coupling to obtain acceptable launch powers. For example, the LED illustrated in Figure 7.6 with a drive current of 50 mA was found to couple only around 2 μW of optical power into single-mode fiber [Ref. 14].

7.3.4 Edge emitter LEDs

Another basic high radiance structure currently used in optical communications is the stripe geometry DH edge emitter LED (ELED). This device has a similar geometry to a conventional contact stripe injection laser, as shown in Figure 7.7. It takes advantage of transparent guiding layers with a very thin active layer (50 to 100 μm) in order that the light produced in the active layer spreads into the transparent guiding layers, reducing self absorption in the active layer. The

consequent waveguiding narrows the beam divergence to a half power width of around 30° in the plane perpendicular to the junction. However, the lack of waveguiding in the plane of the junction gives a Lambertian output with a half power width of around 120°, as illustrated in Figure 7.7.

Most of the propagating light is emitted at one end face only due to a reflector on the other end face and an antireflection coating on the emitting end face. The effective radiance at the emitting end face can be very high giving an increased coupling efficiency into small NA fiber compared with the surface emitter. However, surface emitters generally radiate more power into air (2.5 to 3 times) than edge emitters since the emitted light is less affected by reabsorption and interfacial recombination. Comparisons [Refs. 15 to 17] have shown that edge emitters couple more optical power into low NA (less than 0.3) than surface emitters, whereas the opposite is true for large NA (greater than 0.3).

The enhanced waveguiding of the edge emitter enables it in theory [Ref. 16] to couple 7.5 times more power into low NA fiber than a comparable surface emitter. However, in practice the increased coupling efficiency has been found to be slightly less than this (3.5 to 6 times) [Refs. 16 and 17]. Similar coupling efficiencies may be achieved into low NA fiber with surface emitters by the use of a lens.

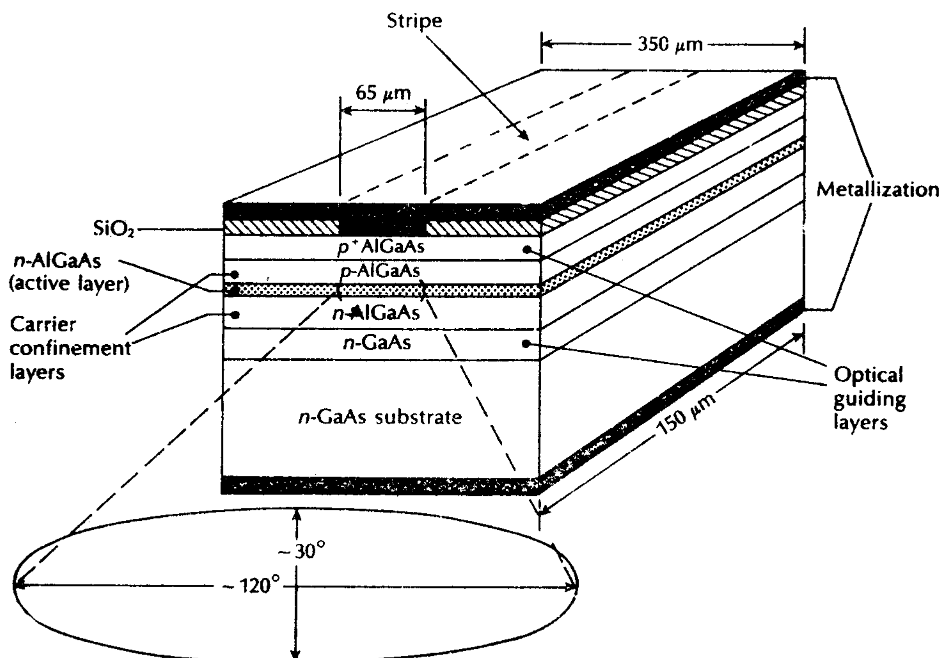

Figure 7.7 Schematic illustration of the structure of a strip geometry DH AlGaAs edge-emitting LED.

Furthermore, it has been found that lens coupling with edge emitters may increase the coupling efficiencies by comparable factors (around five times).

The stripe geometry of the edge emitter allows very high carrier injection densities for given drive currents. Thus it is possible to couple approaching a milliwatt of optical power into low NA (0.14) multimode step index fiber with edge-emitting LEDs operating at high drive currents (500 mA) [Ref. 18].

Edge emitters have also been found to have a substantially better modulation bandwidth of the order of hundreds of megahertz than comparable surface-emitting structures with the same drive level [Ref. 17]. In general it is possible to construct edge-emitting LEDs with a narrower linewidth than surface emitters, but there are manufacturing problems with the more complicated structure (including difficult heat sinking geometry) which moderate the benefits of these devices.

Nevertheless, a number of ELED structures have been developed using the InGaAsP/InP material system for operation at a wavelength of 1.3 μm. A common device geometry which has also been utilized for AlGaAs/GaAs ELEDs [Ref. 19] is shown in Figure 7.8 [Ref. 20]. This DH edge-emitting device is realized in the form of a restricted length, stripe geometry *p*-contact arrangement. Such devices are also referred to as truncated-stripe ELEDs. The short stripe structure (around 100 μm long) improves the external efficiency of the ELED by reducing its internal absorption of carriers.

It was mentioned in Section 7.1 that a particular impetus for the development of high performance LEDs operating at a wavelength of 1.3 μm was their potential application in the future optical fiber subscriber loop. In this context the capacity to provide both high speed transmission and significant launch powers into single-mode fiber are of prime concern. Aspects of these attributes are displayed by the two device structures shown in Figure 7.9.

The ELED illustrated in Figure 7.9(a) [Ref. 21] comprises a mesa structure with a width of 8 μm and a length of 150 μm for current confinement. The tilted back facet of the device was formed by chemical etching in order to suppress laser

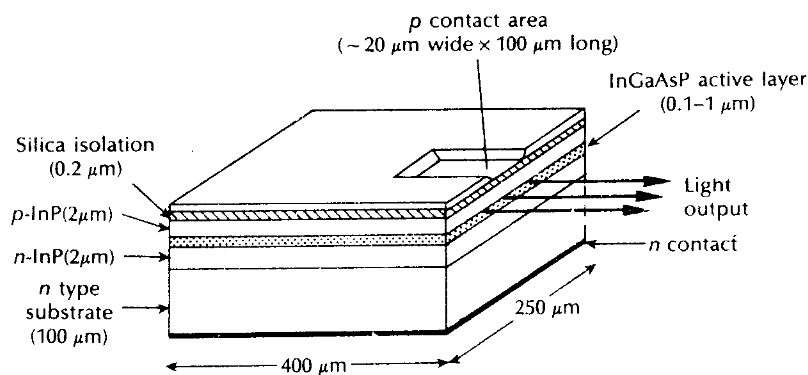

Figure 7.8 Truncated stripe InGaAsP edge-emitting LED [Ref. 20].

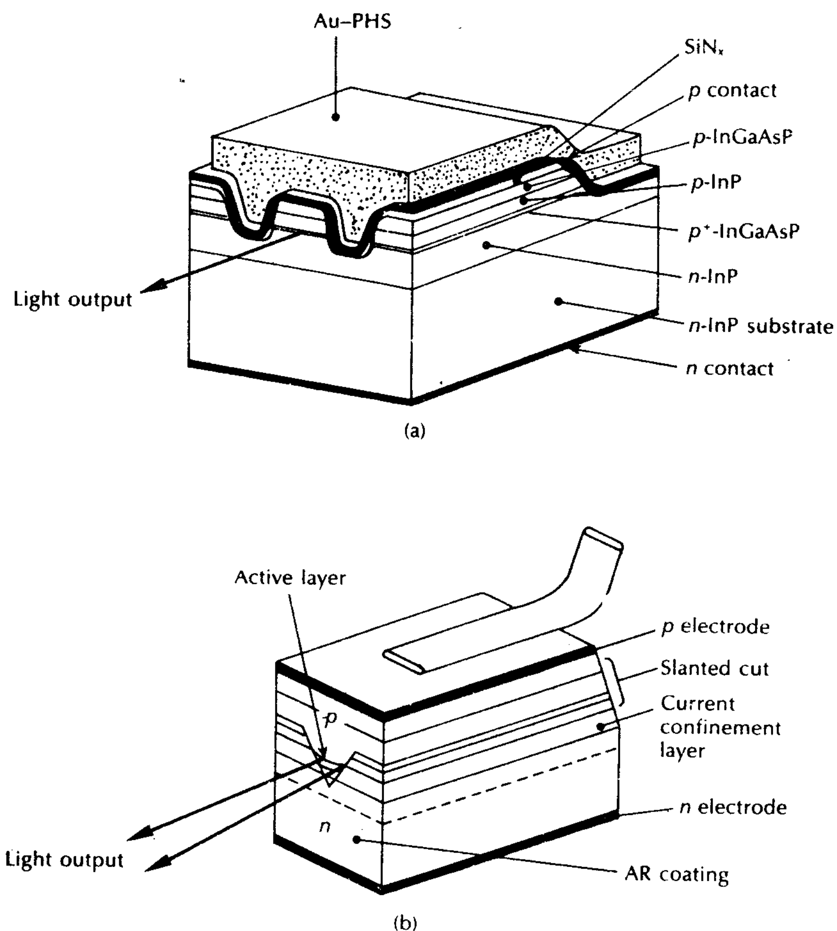

Figure 7.9 High speed InGaAsP edge-emitting LEDs: (a) mesa structure ELED [Ref. 21]. (b) V-grooved substrate BH ELED [Ref. 23].

oscillation. It should be noted that such ELED device structures, being very similar to injection structures, could lase unless this mechanism is specifically avoided by removing the potential Fabry–Perot cavity. This point is discussed in further detail in Section 7.3.5.

The ELED active layer was heavily doped with Zn to reduce the minority carrier lifetime and thus improve the device modulation bandwidth. In this way a 3 dB modulation bandwidth of 600 MHz was obtained [Ref. 21]. When operating at a speed of 600 Mbit s^{-1} the device, with lens coupling (see Section 7.3.6), launched an average optical power of approximately 4 μW into single-mode fiber at a peak drive current of 100 mA. An increase in the peak drive current to 240 mA provided

an improvement in the coupled power to slightly over 6 μW. By contrast a buried heterostructure ELED has been reported which couples 7 μW of optical power into single-mode fiber with a drive current of only 20 mA [Ref. 22]. This short cavity device (100 μm) had a spectral width (FWHP) of 70 nm in comparison with a linewidth of 90 nm for the high speed ELED shown in Figure 7.9(a).

Figure 7.9(b) displays another advanced InGaAsP ELED which was fabricated as a V-grooved substrate buried heterostructure device [Ref. 23]. In this case the front facet was antireflection coated and the rear facet was also etched at a slat to prevent laser action. This device, which again emitted at a centre wavelength of 1.3 μm, was reported to have a 3 dB modulation bandwidth around 350 MHz, with the possibility of launching 30 μW of optical power into single-mode fiber [Ref. 23].

Very high coupled optical power levels into single-mode fiber in excess of 100 μW have been obtained with InGaAsP ELEDs at drive currents as low as 50 mA [Ref. 24]. This device structure was based on the configuration of the *p*-substrate buried crescent injection laser [Ref. 25] with the rear facet bevelled by chemical etching to suppress laser oscillation. Butt coupling to 10 μm core diameter single-mode fiber provided launch powers of only 12 μW which were increased to over 200 μW using lens coupling (see Section 7.3.6) and drive currents of 100 mA. Moreover, the spectral widths of the ELEDs were as narrow as 50 nm which gave device characteristics approaching those of the superluminescent LEDs dealt with in the following section.

7.3.5 Superluminescent LEDs

A third device geometry which is already providing significant benefits over both SLEDs and ELEDs for communication applications is the superluminescent diode or SLD. This device type offers advantages of: (a) a high output power; (b) a directional output beam; and (c) a narrow spectral linewidth; all of which prove useful for coupling significant optical power levels into optical fiber (in particular to single-mode fiber [Ref. 22]). Furthermore, the superradiant emission process within the SLD tends to increase the device modulation bandwidth over that of more conventional LEDs.

Figure 7.10 shows two forms of construction for the SLD. It may be observed that the structures in both cases are very similar to those of ELEDs or, for that matter, injection lasers. In effect, the SLD has optical properties that are bounded by the ELED and the injection laser. Similar to this latter device the SLD structure requires a *p–n* junction either in the form of a long rectangular stripe (Figure 7.10(a) [Ref. 26]), a ridge waveguide [Ref. 27] or a buried heterostructure (Figure 7.10(b) [Refs. 22, 28]). However, one end of the device is made optically lossy to prevent reflections and thus suppress lasing, the output being from the opposite end.

For operation the injected current is increased until stimulated emission, and hence amplification, occurs (i.e. the initial step towards laser action), but because there is high loss at one end of the device, no optical feedback takes place.

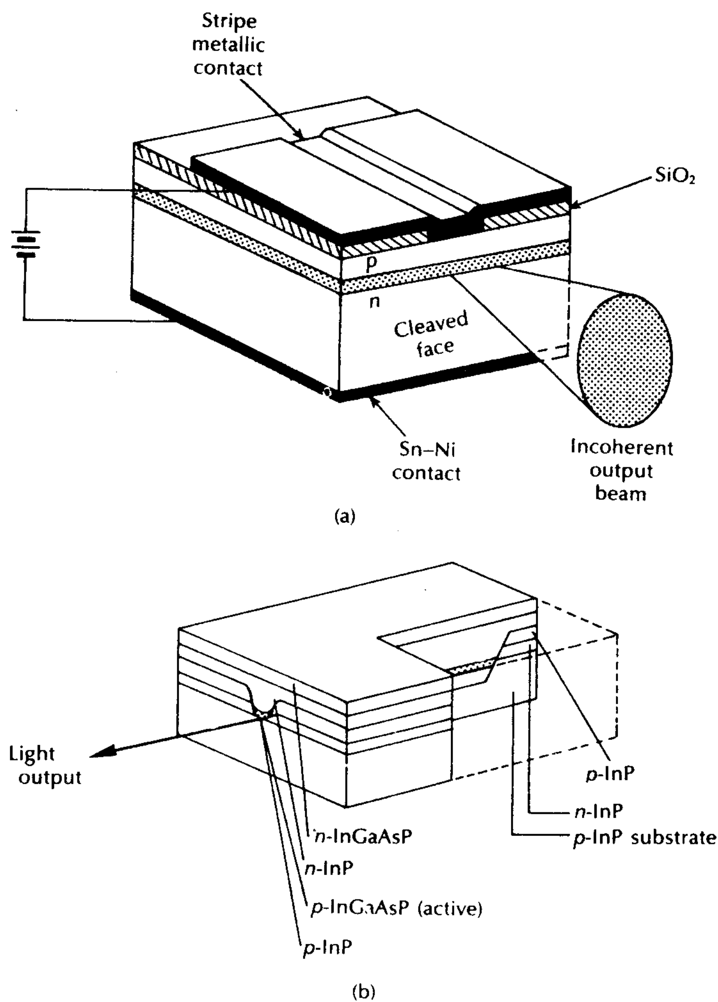

Figure 7.10 Superluminescent LED structures: (a) AlGaAs contact stripe SLD [Ref. 26]; (b) high output power InGaAsP SLD [Ref. 28].

Therefore, although there is amplification of the spontaneous emission, no laser oscillation builds up. However, operation in the current region for stimulated emission provides gain causing the device output to increase rapidly with increases in drive current due to what is effectively single pass amplification. High optical output power can therefore be obtained, together with a narrowing of the spectral width which also results from the stimulated emission.

An early SLD is shown in Figure 7.10(a) which employs a contact stripe together with an absorbing region at one end to suppress laser action. Such devices have

provided peak output power of 60 mW at a wavelength of 0.87 μm in pulsed mode [Ref. 26]. More recently, antireflection (AR) coatings have been applied to the cleaved facets of SLDs in order to suppress Fabry–Perot resonance [Refs. 22, 27, 29]. Such devices have launched 550 μW of optical power in 50 μm diameter multimode graded index fiber at drive currents of 250 mA [Ref. 22] and 250 μW into single-mode fiber using drive currents of 100 mA [Ref. 29]. In both cases the device linewidths were in the range 30 to 40 nm rather than the 60 to 90 nm spectral widths associated with conventional ELEDs.

The structure of a recently developed InGaAsP/InP SLD is illustrated in Figure 7.10(b) [Ref. 28]. The device which emits at 1.3 μm comprises a buried active layer within a V-shaped groove on the *p* type InP substrate. This technique provides an appropriate structure for high power operation because of its low leakage current. Unlike the aforementioned SLD structures which incorporate AR coatings on both end facets to prevent feedback, a light diffusion surface is placed within this device. The surface, which is applied diagonally on the active layer of length 350 μm, serves to scatter the backward light emitted from the active layer and thus decreases feedback into this layer. In addition, an AR coating is provided on the output facet. As it is not possible to achieve a perfect antireflection coating, the above structure is therefore not left totally dependent on this feedback suppression mechanism. The coupling of 1 mW of optical power into the spherically lensed end of a single-mode fiber (10 μm core diameter) has been demonstrated with this device operating at a drive current of 150 mA [Ref. 28]. Moreover, the spectral distribution from the SLD was observed to be a smooth envelope with a FWHP of 30 nm, whilst the device modulation bandwidth reached 350 MHz at the −1.5 dB point (see Section 7.4.3).

Although the incoherent optical power output from SLDs can approach that of the coherent output from injection lasers, the required current density is substantially higher (by around a factor of three times), necessitating high drive currents due to the long device active lengths (i.e. large areas). Recent improvements, however, in injection laser structures (see Sections 6.5 and 6.6) providing lower threshold currents for specific output powers have also made the SLD a more practical proposition. Nevertheless, other potential drawbacks associated with the SLD in comparison with conventional LEDs are the nonlinear output characteristic and the increased temperature dependence of the output power (see Section 7.4.1).

7.3.6 Lens coupling to fiber

It is apparent that much of the light emitted from LEDs is not coupled into the generally narrow acceptance angle of the fiber. Even with the etched well surface emitter where the low NA fiber is butted directly into the emitting aperture of the device, coupling efficiencies are poor (of the order of 1 to 2%). However, it has been found that greater coupling efficiency may be obtained if lenses are used to collimate the emission from the LED, particularly when the fiber core diameter is significantly larger than the width of the emission region. There are several lens

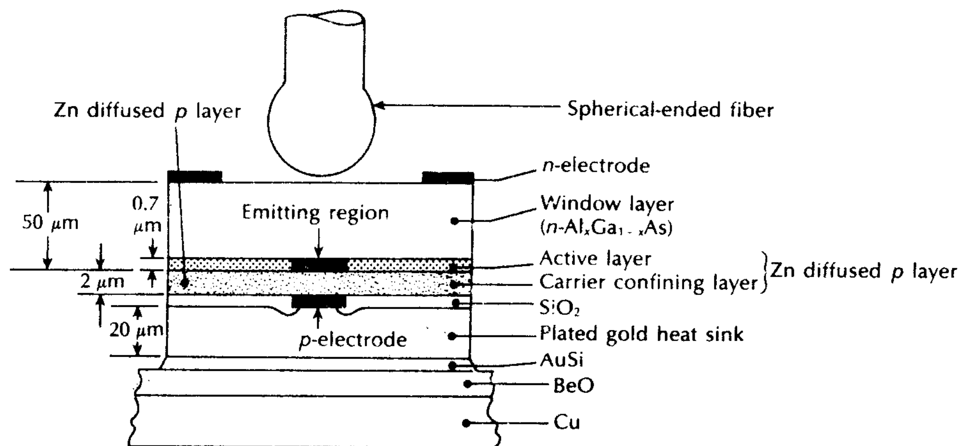

Figure 7.11 Schematic illustration of the structure of a spherical-ended fiber coupled AlGaAs LED [Ref. 30].

coupling configurations which include spherically polished structures not unlike the dome LED, spherical-ended or tapered fiber coupling, truncated spherical microlenses, GRIN-rod lenses and integral lens structures.

A GaAs/AlGaAs spherical-ended fiber coupled LED is illustrated in Figure 7.11 [Ref. 30]. It consists of a planar surface emitting structure with the spherical-ended fiber attached to the cap by epoxy resin. An emitting diameter of 35 μm was fabricated into the device and the light was coupled into fibers with core diameters of 75 and 110 μm. The geometry of the situation is such that it is essential that the active diameter of the device be substantially less (factor of 2) than the fiber core diameter if increased coupling efficiency is to be obtained. In this case good performance was obtained with coupling efficiencies around 6%. This is in agreement with theoretical [Ref. 31] and other experimental [Ref. 32] results which suggest an increased coupling efficiency of 2 to 5 times through the spherical fiber lens.

Another common lens coupling technique employs a truncated spherical microlens. This configuration is shown in Figure 7.12 for an etched well InGaAsP/InP DH surface emitter [Ref. 33] operating at a wavelength of 1.3 μm. Again, a requirement for efficient coupling is that the emission region diameter is much smaller than the core diameter of the fiber. In this case the best results were obtained with a 14 μm active diameter and an 85 μm core diameter step index fiber with a numerical aperture of 0.16. The coupling efficiency was increased by a factor of 13, again supported by theory [Ref. 31] which suggests possible increases of up to thirty times.

However, the overall power conversion efficiency η_{pc} which is defined as the ratio of the optical power coupled into the fiber P_c to the electrical power applied at the

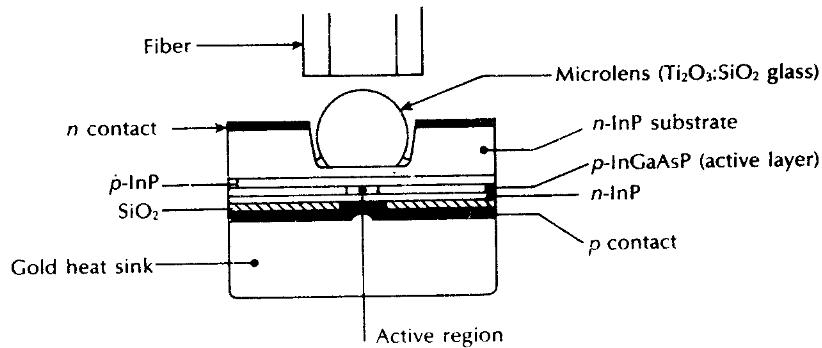

Figure 7.12 The use of a truncated spherical microlens for coupling the emission from an InGaAsP surface-emitting LED to the fiber [Ref. 33].

terminals of the device P and is therefore given by:

$$\eta_{pc} = \frac{P_c}{P} \tag{7.23}$$

is still quite low. Even with the increased coupling efficiency η_{pc} was found to be around 0.4%.

Example 7.5

A lens coupled surface-emitting LED launches 190 μW of optical power into a multimode step index fiber when a forward current of 25 mA is flowing through the device. Determine the overall power conversion efficiency when the corresponding forward voltage across the diode is 1.5 V.

Solution: The overall power conversion efficiency may be obtained from Eq. (7.23) where:

$$\eta_{pc} = \frac{P_c}{P} = \frac{190 \times 10^{-6}}{25 \times 10^{-3} \times 1.5} = 5.1 \times 10^{-3}$$

Hence the overall power conversion efficiency is 0.5%.

The integral lens structure shown in Figure 7.6 has become a favoured power coupling strategy for use with surface emitters. In this technique a low absorption lens is formed at the exit face of the substrate material instead of it being fabricated in glass and attached to a planar SLED with epoxy. The method benefits from the elimination of the semiconductor-epoxy-lens interface which can limit the maximum lens gains of the SLEDs discussed above. An early example gave an improved coupling efficiency of around three times that of a planar SLED [Ref.

32], but for optimized devices it is predicted that coupling efficiencies should exceed 15% [Ref. 33].

It was mentioned in Section 7.3.4 that lens coupling can also be usefully employed with edge-emitting devices. In practice, lenses attached to the fiber ends or tapered fiber lenses are widely utilized to increase the coupling efficiency [Refs. 13, 19]. An example of the former technique is illustrated in Figure 7.13(a) in which a hemispherical lens is epoxied onto the fiber end and positioned adjacent to the ELED emission region. The coupling efficiency has been increased by a factor of three to four times using this strategy [Refs. 13, 19]. Alternatively, a truncated spherical lens glued onto the emitting facet of a superradiant ELED has given a coupling gain of a factor of five or 7 dB [Ref. 34].

Tapered fiber lenses have been extensively used to couple power from ELEDs into single-mode fiber. Butt coupling of optical power from LEDs into single-mode fiber is substantially reduced in comparison with that obtained into multimode fiber. It ranges from between 0.5 and 2 μW for a standard SLED up to around 10 to 12 μW for an ELED. The small core diameter of single-mode fiber does not allow significant lens coupling gain to be achieved with SLEDs. For edge emitters, however, a coupling gain of around 5 dB may be realized using tapered fiber [Ref. 35].

An alternative strategy to improve the coupling efficiency from an ELED into single-mode fiber is depicted in Figure 7.13(b) [Ref. 24]. In this case a tapered GRIN-rod lens (see Section 5.5.1) was positioned between the high power ELED and the fiber. A coupling efficiency defined as the ratio of the coupled power to the total emitted power of around 15% was obtained [Ref. 24].

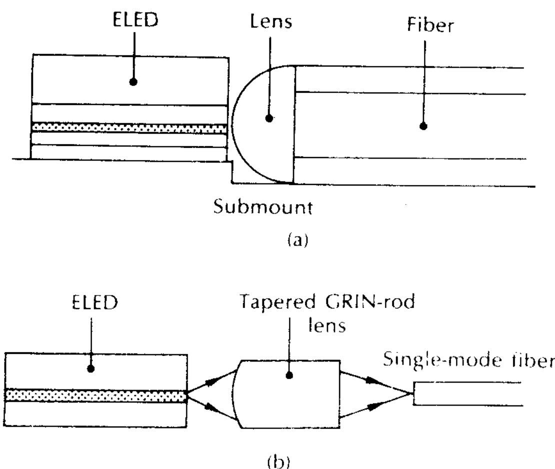

Figure 7.13 Lens coupling with edge-emitting LEDs: (a) lens-ended fiber coupling; (b) tapered (plano-convex) GRIN-rod lens coupling to single-mode fiber.

7.4 LED characteristics

7.4.1 Optical output power

The ideal light output power against current characteristic for an LED is shown in Figure 7.14. It is linear corresponding to the linear part of the injection laser optical power output characteristic before lasing occurs. Intrinsically the LED is a very linear device in comparison with the majority of injection lasers and hence it tends to be more suitable for analog transmission where severe constraints are put on the linearity of the optical source. However, in practice LEDs do exhibit significant nonlinearities which depend upon the configuration utilized. It is therefore often necessary to use some form of linearizing circuit technique (e.g. predistortion linearization or negative feedback) in order to ensure the linear performance of the device to allow its use in high quality analog transmission systems [Ref. 37]. Figure 7.15(a) and (b) show the light output against current characteristics for

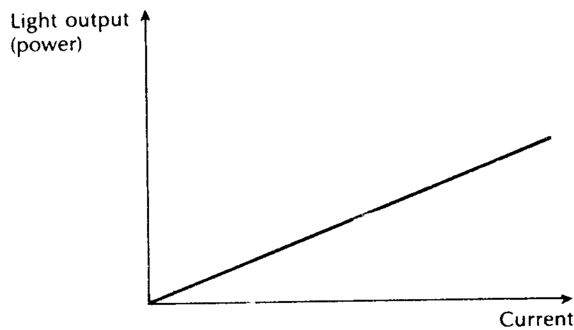

Figure 7.14 An ideal light output against current characteristic for an LED.

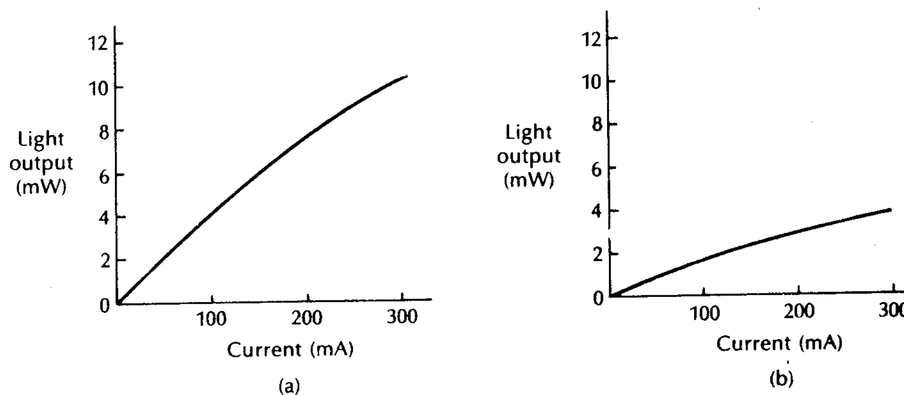

Figure 7.15 Light output (power) into air against d.c. drive current for typically good LEDs [Ref. 17]: (a) an AlGaAs surface emitter with a 50 μm diameter dot contact; (b) an AlGaAs edge emitter with a 65 μm wide stripe and 100 μm length.

typically good surface and edge emitters respectively [Ref. 17]. It may be noted that the surface emitter radiates significantly more optical power into air than the edge emitter, and that both devices are reasonably linear at moderate drive currents.

In a similar manner to the injection laser, the internal quantum efficiency of LEDs decreases exponentially with increasing temperature (see Section 6.7.1) Hence the light emitted from these devices decreases as the p–n junction temperature increases. The light output power against temperature characteristics for the three major LED structures operating at a wavelength of 1.3 μm are shown, for comparison, in Figure 7.16 [Ref. 13]. It may be observed that the edge-emitting device exhibits a greater temperature dependence than the surface emitter and that the output of the SLD with its stimulated emission is *strongly* dependent on the junction temperature. This latter factor is further emphasized in the light output against current characteristics for a superluminescent LED displayed in Figure 7.17 [Ref. 27]. These characteristics show the variation in output power at a specific drive current over the temperature range 0 to 40 °C for a ridge waveguide device providing lateral current confinement. The nonlinear nature of the output characteristic typical of SLDs can also be observed with a knee becoming apparent at an operating temperature around 20 °C. Hence to utilize the high power potential of such devices at elevated temperatures, the use of thermoelectric coolers may be necessary [Ref. 13].

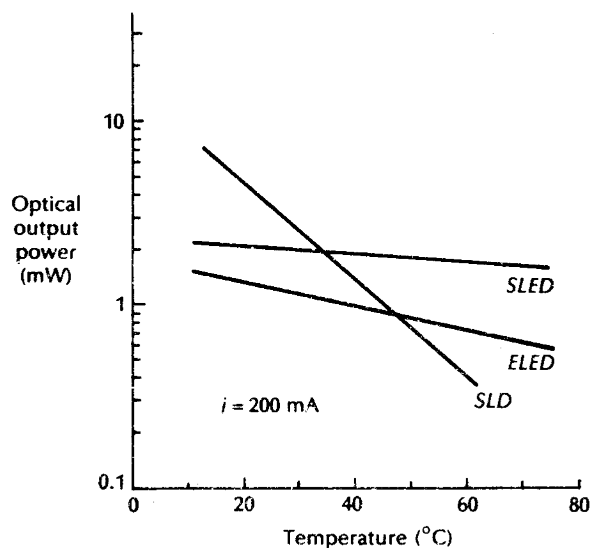

Figure 7.16 Light output temperature dependence for the three major LED structures emitting at a wavelength of 1.3 μm [Ref. 13].

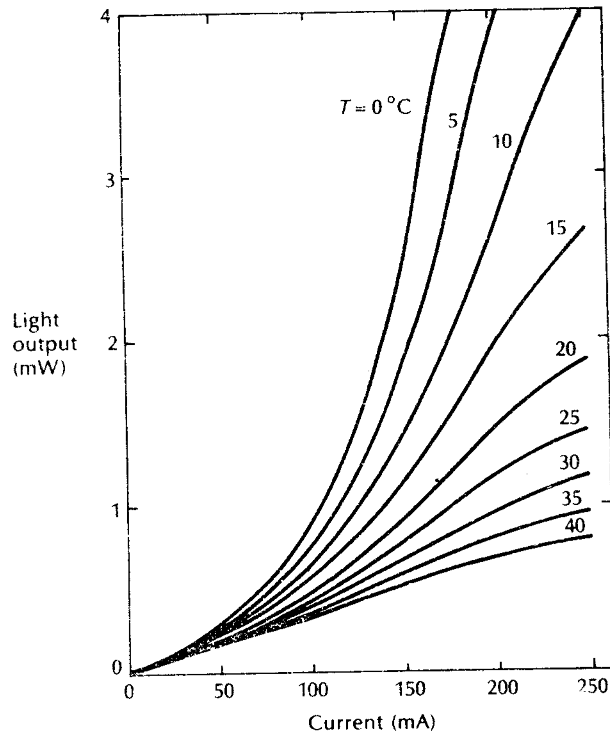

Figure 7.17 Light output against current characteristic at various ambient temperatures for an InGaAsP ridge waveguide SLD. Reproduced with permission from I. P. Kaminow, G. Eisenstein, L. W. Stulz and A. G. Dentai 'Lateral confinement InGaAsP superluminescent diode at 1.3 μm', *IEEE J. Quantum Electron.*, **QE19**, p. 78, 1983. Copyright © 1983, IEEE.

7.4.2 Output spectrum

The spectral linewidth of an LED operating at room temperature in the 0.8 to 0.9 μm wavelength band is usually between 25 and 40 nm at the half maximum intensity points (full width at half power (FWHP) points). For materials with smaller bandgap energies operating in the 1.1 to 1.7 μm wavelength region the linewidth tends to increase to around 50 to 160 nm. Examples of these two output spectra are shown in Figure 7.18 [Refs. 7 and 38]. Also illustrated in Figure 7.18(b) are the increases in linewidth due to increased doping levels and the formation of bandtail states (see Section 6.3.4). This becomes apparent in the differences in the output spectra between surface- and edge-emitting LEDs where the devices have generally heavily doped and lightly doped (or undoped) active layers respectively. It may also be noted that there is a shift to lower peak emission wavelength (i.e. higher energy) through reduction in doping in Figure 7.18(b), and hence the

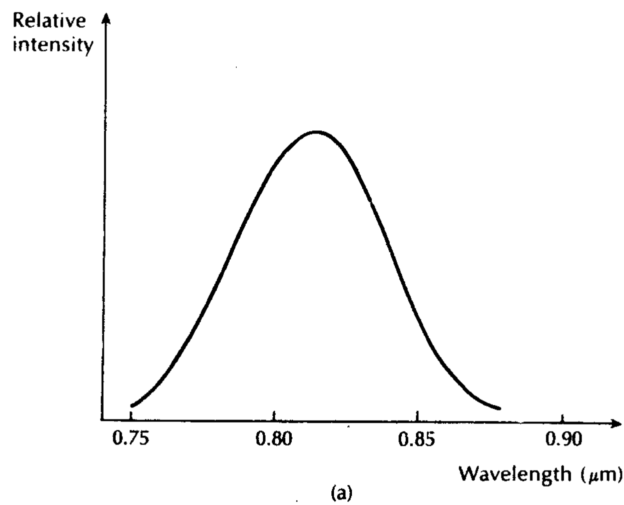

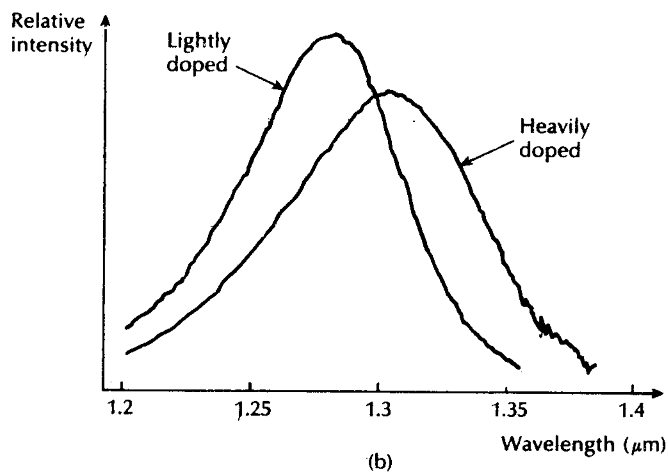

Figure 7.18 LED output spectra: (a) output spectrum for an AlGaAs surface emitter with doped active region [Ref. 7]; (b) output spectra for an InGaAsP surface emitter showing both the lightly doped and heavily doped cases. Reproduced with permission from A. C. Carter. *The Radio and Electron. Eng.*, **51**, p. 41, 1981.

active layer composition must be adjusted if the same centre wavelength is to be maintained.

The differences in the output spectra between InGaAsP SLEDs and ELEDs caused by self absorption along the active layer of the devices are displayed in Figure 7.19. It may be observed that the FWHP points are around 1.6 times smaller for the ELED than the SLED [Ref. 13]. In addition, the spectra of the ELED

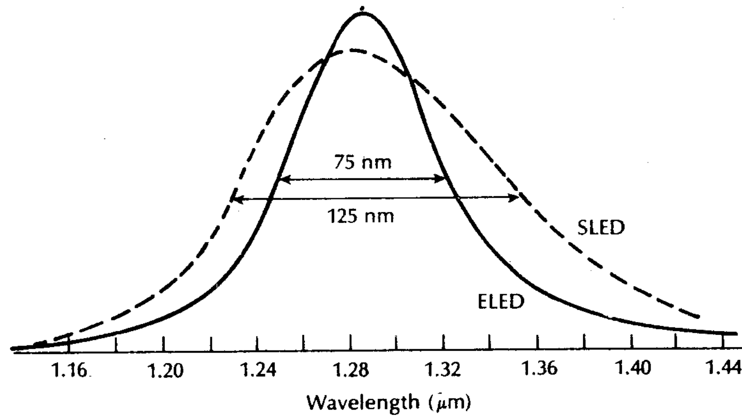

Figure 7.19 Typical spectral output characteristics for InGaAsP surface and edge-emitting LEDs operating in the 1.3 μm wavelength region [Ref. 13].

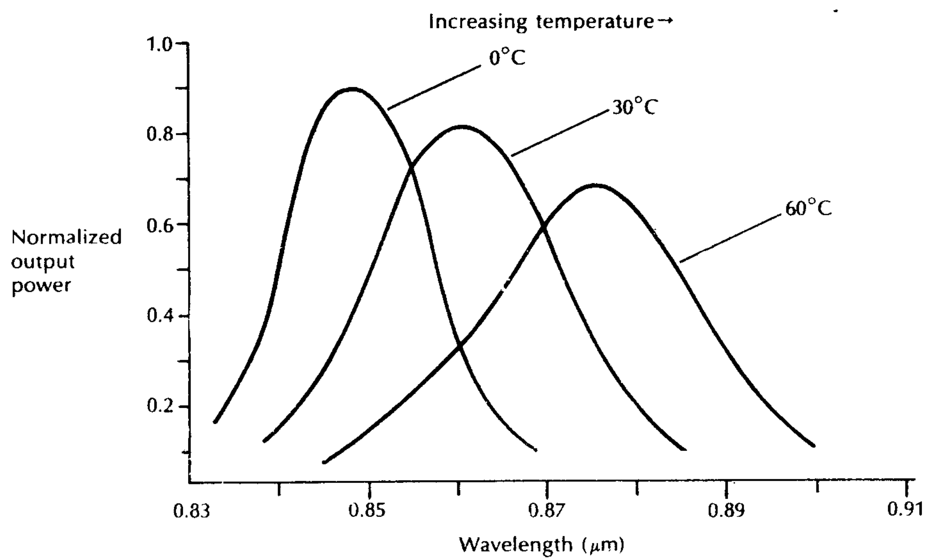

Figure 7.20 Typical spectral variation of the output characteristic with temperature for an AlGaAs surface-emitting LED.

may be further narrowed by the superluminescent operation due to the onset of stimulated gain and in this case the linewidth can be far smaller (e.g. 30 nm) than that obtained with the SLED.

The output spectra also tend to broaden at a rate of between 0.1 and 0.3 nm $^{\circ}C^{-1}$ with increase in temperature due to the greater energy spread in carrier distributions at higher temperatures. Increases in temperature of the junction affect the peak emission wavelength as well, and it is shifted by +0.3 to 0.4 nm $^{\circ}C^{-1}$ for AlGaAs devices [Ref. 11] and by +0.6 nm $^{\circ}C^{-1}$ for InGaAsP devices [Ref. 39]. The combined effects on the output spectrum from a typical AlGaAs surface emitter are illustrated in Figure 7.20. It is clear that it may therefore be necessary to utilize heat sinks with LEDs for certain optical fiber communication applications, although this is far less critical (normally insignificant compared with the device linewidth) than the cooling requirements for injection lasers.

7.4.3 Modulation bandwidth

The modulation bandwidth in optical communications may be defined in either electrical or optical terms. However, it is often more useful when considering the associated electrical circuitry in an optical fiber communication system to use the electrical definition where the electrical signal power has dropped to half its constant value due to the modulated portion of the optical signal. This corresponds to the electrical 3 dB point or the frequency at which the output electrical power is reduced by 3 dB with respect to the input electrical power. As optical sources operate down to d.c. we only consider the high frequency 3 dB point, the modulation bandwidth being the frequency range between zero and this high frequency 3 dB point.

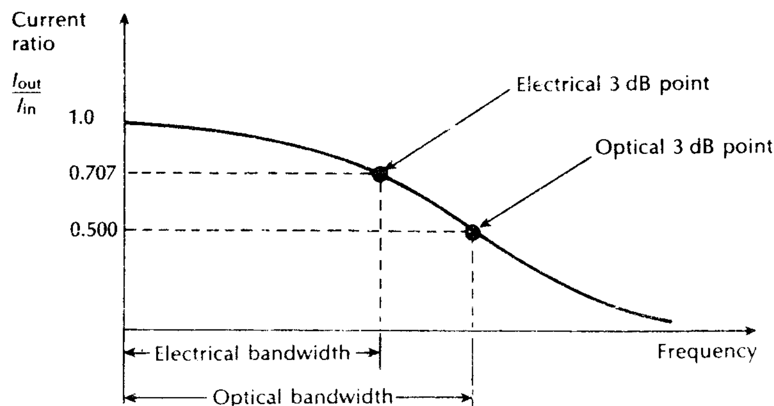

Figure 7.21 The frequency response for an optical fiber system showing the electrical and optical bandwidths

Alternatively, if the 3 dB bandwidth of the modulated optical carrier (optical bandwidth) is considered, we obtain an increased value for the modulation bandwidth. The reason for this inflated modulation bandwidth is illustrated in Example 7.6 and Figure 7.21. In considerations of bandwidth within the text the electrical modulation bandwidth will be assumed unless otherwise stated, following current practice.

Example 7.6

Compare the electrical and optical bandwidths for an optical fiber communication system and develop a relationship between them.

Solution: In order to obtain a simple relationship between the two bandwidths it is necessary to compare the electrical current through the system. Current rather than voltage (which is generally used in electrical systems) is compared as both the optical source and optical detector (see Section 8.6) may be considered to have a linear relationship between light and current.

Electrical bandwidth: The ratio of the electrical output power to the electrical input power in decibels RE_{dB} is given by:

$$RE_{dB} = 10 \log_{10} \frac{\textit{electrical power out (at the detector)}}{\textit{electrical power in (at the source)}}$$

$$= 10 \log_{10} \frac{I_{out}^2/R_{out}}{I_{in}^2/R_{in}}$$

$$\propto 10 \log_{10} \left[\frac{I_{out}}{I_{in}}\right]^2$$

The electrical 3 dB points occur when the ratio of electrical powers shown above is $\frac{1}{2}$. Hence it follows that this must occur when:

$$\left[\frac{I_{out}}{I_{in}}\right]^2 = \frac{1}{2}, \quad \text{or} \quad \frac{I_{out}}{I_{in}} = \frac{1}{\sqrt{2}}$$

Thus in the electrical regime the bandwidth may be defined by the frequency when the output current has dropped to $1/\sqrt{2}$ or 0.707 of the input current to the system.

Optical bandwidth: The ratio of the optical output power to the optical input power in decibels RO_{dB} is given by,

$$RO_{dB} = 10 \log_{10} \frac{\textit{optical power out (received a detector)}}{\textit{optical power in (transmitted at source)}}$$

$$10 \log_{10} \frac{I_{out}}{I_{in}}$$

(due to the linear light/current relationships of the source and detector). Hence the optical 3 dB points occur when the ratio of the currents is equal to $\frac{1}{2}$, and:

$$\frac{I_{out}}{I_{in}} = \frac{1}{2}$$

Therefore in the optical regime the bandwidth is defined by the frequencies at which the output current has dropped to $\frac{1}{2}$ or 0.5 of the input current to the system. This corresponds to an electrical power attenuation of 6 dB.

The comparison between the two bandwidths is illustrated in Figure 7.21 where it may be noted that the optical bandwidth is significantly greater than the electrical bandwidth. The difference between them (in frequency terms) depends on the shape of the frequency response for the system. However, if the system response is assumed to be Gaussian, then the optical bandwidth is a factor of $\sqrt{2}$ greater than the electrical bandwidth [Ref. 40].

The modulation bandwidth of LEDs is generally determined by three mechanisms. These are:

(a) the doping level in the active layer;
(b) the reduction in radiative lifetime due to the injected carriers;
(c) the parasitic capacitance of the device.

Assuming negligible parasitic capacitance, the speed at which an LED can be directly current modulated is fundamentally limited by the recombination lifetime of the carriers, where the optical output power $P_e(\omega)$ of the device (with constant peak current) and angular modulation frequency ω is given by [Ref. 41],

$$\frac{P_e(\omega)}{P_{dc}} = \frac{1}{[1 + (\omega\tau_i)^2]^{\frac{1}{2}}} \tag{7.24}$$

where τ_i is the injected (minority) carrier lifetime in the recombination region and P_{dc} is the d.c. optical output power for the same drive current.

Example 7.7

The minority carrier recombination lifetime for an LED is 5 ns. When a constant d.c. drive current is applied to the device the optical output power is 300 μW. Determine the optical output power when the device is modulated with an rms drive current corresponding to the d.c drive current at frequencies of (a) 20 MHz; (b) 100 MHz.

It may be assumed that parasitic capacitance is negligible. Further, determine the 3 dB optical bandwidth for the device and estimate the 3 dB electrical bandwidth assuming a Gaussian response.

Solution: (a) From Eq. (7.24), the optical output power at 20 MHz is:

$$P_e(20\ \text{MHz}) = \frac{P_{dc}}{[1 + (\omega\tau_i)^2]^{\frac{1}{2}}}$$

$$= \frac{300 \times 10^{-6}}{[1 + (2\pi \times 20 \times 10^6 \times 5 \times 10^{-9})^2]^{\frac{1}{2}}}$$

$$= \frac{300 \times 10^{-6}}{[1.39]^{\frac{1}{2}}}$$

$$= 254.2\ \mu\text{W}$$

(b) Again using Eq. (7.24):

$$P_e(100\ \text{MHz}) = \frac{300 \times 10^{-6}}{[1 + (2\pi \times 100 \times 10^6 \times 5 \times 10^{-9})^2]^{\frac{1}{2}}}$$

$$= \frac{300 \times 10^{-6}}{[10.87]^{\frac{1}{2}}}$$

$$= 90.9\ \mu\text{W}$$

This example illustrates the reduction in the LED optical output power as the device is driven at higher modulating frequencies. It is therefore apparent that there is a somewhat limited bandwidth over which the device may be usefully utilized.

To determine the optical 3 dB bandwidth: the high frequency 3 dB point occurs when $P_e(\omega)/P_{dc} = \frac{1}{2}$. Hence, using Eq. (7.24):

$$\frac{1}{[1 + (\omega\tau_i)^2]^{\frac{1}{2}}} = \frac{1}{2}$$

and $1 + (\omega\tau_i)^2 = 4$. Therefore $\omega\tau_i = \sqrt{3}$, and

$$f = \frac{\sqrt{3}}{2\pi\tau} = \frac{\sqrt{3}}{\pi \times 10^{-8}} = 55.1\ \text{MHz}$$

Thus the 3 dB optical bandwidth B_{opt} is 55.1 MHz as the device similar to all LEDs operates down to d.c.

Assuming a Gaussian frequency response, the 3 dB electrical bandwidth B will be:

$$B = \frac{55.1}{\sqrt{2}} = 39.0\ \text{MHz}$$

Thus the corresponding electrical bandwidth is 39 MHz. However, it must be remembered that parasitic capacitance may reduce the modulation bandwidth below this value.

The carrier lifetime is dependent on the doping concentration, the number of injected carriers into the active region, the surface recombination velocity and the thickness of the active layer. All these parameters tend to be interdependent and are adjustable within limits in present-day technology. In general, the carrier lifetime may be shortened by either increasing the active layer doping or by decreasing the thickness of the active layer. However, in surface emitters this can reduce the external power efficiency of the device due to the creation of an increased number of nonradiative recombination centres.

Edge-emitting LEDs have a very thin, virtually undoped active layer and the carrier lifetime is controlled only by the injected carrier density. At high current densities the carrier lifetime decreases with injection level because of a bimolecular recombination process [Ref. 41]. This bimolecular recombination process allows edge-emitting LEDs with narrow recombination regions to have short recombination times, and therefore relatively high modulation capabilities at reasonable operating current densities. For instance, edge-emitting devices with electrical modulation bandwidths of 145 MHz have been achieved with moderate doping and extremely thin (approximately 50 nm) active layers [Ref. 42].

However, LEDs tend to be slower devices with significantly lower output powers than injection lasers because of the longer lifetime of electrons in their donor regions resulting from spontaneous recombination rather than stimulated emission,* coupled with the increased numbers of nonradiative centres at higher doping levels. Thus at high modulation bandwidths the optical output power from conventional LED structures decreases as illustrated in Example 7.7 and also as shown in Figure 7.22.

The reciprocal relationship between modulation bandwidth and output power may be observed in Figure 7.22 which illustrates experimental results obtained with both AlGaAs and InGaAsP LEDs [Refs. 43, 44]. The solid line gives an indication of the best results for AlGaAs LEDs, whereas, for comparison, the dotted line represents these AlGaAs results shifted by the ratio of the photon energy at 0.85 μm to that at 1.3 μm. Finally, the dashed line provides a contour of the best reported results for InGaAsP LEDs. It may be observed that the output power from AlGaAs LEDs is a factor of two higher than that of InGaAsP devices at all bandwidths which partly results from the photon energy at the 1.3 μm wavelength being smaller (by a factor of 1.53) than that at 0.85 μm. Hence the centre dotted line displays the adjustment of the AlGaAs LEDs for this factor showing that the best performance of InGaAsP LEDs is not far below that of AlGaAs LEDs. Moreover the difference is probably due to the more advanced technology which is available for the latter devices combined with the enhanced wavelength saturation in the longer wavelength material [Ref. 13].

For surface-emitting AlGaAs LEDs high output power of 15 mW has been obtained at modest bandwidths (17 MHz) [Ref. 45], whereas the very large

* The superluminescent LED is an exception in this respect and is therefore capable of high output power at relatively high modulation bandwidths (see Section 7.3.5).

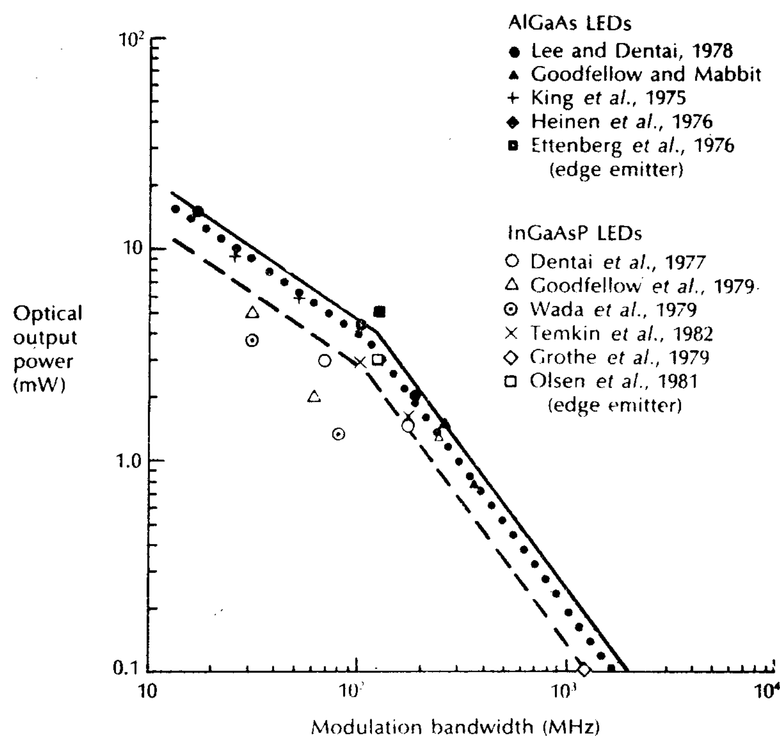

Figure 7.22 Reported optical output power against bandwidth for both AlGaAs and InGaAsP LEDs [Refs. 43,44]. Best results for AlGaAs devices (solid line). These AlGaAs LED results shifted to a wavelength of 1.3 μm (dotted line). Best results for InGaAsP devices (dashed line).

bandwidth of 1.1 GHz was only achieved at the far lower output power of 0.2 mW [Ref. 46]. In general terms, to maximize the output power from SLEDs exhibiting low modulation bandwidths in the range 20 to 50 MHz, a thick active layer (2 to 2.5 μm) with low doping levels (less than 5×10^{17} cm^{-3}) can be employed. Thinner active layers (1 to 1.5 μm) and higher doping levels (0.5 to 1.0×10^{-18} cm^{-3}) are required for devices operating in the 50 to 100 MHz bandwidth region. In order to increase the modulation bandwidth into and beyond the 100 to 200 MHz range, however, very high doping levels in excess of 5×10^{18} cm^{-3} are necessary in combination with thin active layers.

Longer wavelength LEDs fabricated from the InGaAsP/InP material system for operation at a wavelength around 1.3 μm have become widely commercially available. Such devices with undoped (i.e. with a residual n type concentration between 1×10^{-17} and 5×10^{17} cm^{-3}) active layers provide modulation bandwidths in the range 50 to 100 MHz [Ref. 39]. Moreover, with higher doping densities

(5×10^{18} cm^{-3}) and relatively thin active layers (400 nm), bandwidths of 690 MHz have been obtained [Ref. 47]. Modulation rates in the range 600 Mbit s^{-1} to 1.2 Gbit s^{-1} have also been achieved using high levels of Zn doping (1×10^{-19} to 1.3×10^{-19} cm^{-3}) in InGaAsP devices [Refs. 21, 48].

7.4.4 Reliability

LEDs are not generally affected by the catastrophic degradation mechanisms which can severely affect injection lasers (see Section 6.7.6). Early or infant failures do, however, occur as a result of random and not always preventable fabricational defects. Such failures can usually be removed from the LED batch population over an initial burn-in operational period [Ref. 49]. In addition, LEDs do exhibit gradual degradation which may take the form of a rapid degradation mode* or a slow degradation mode.

Rapid degradation in LEDs is similar to that in injection lasers, and is due to both the growth of dislocations and precipitate-type defects in the active region giving rise to dark line defects (DLDs) and dark spot defects (DSDs), respectively, under device ageing [Ref. 43]. DLDs tend to be the dominant cause of rapid degradation in GaAs-based LEDs. The growth of these defects does not depend upon substrate orientation but on the injection current density, the temperature, and the impurity concentration in the active layer.

Good GaAs substrates have dislocation densities around 5×10^4 cm^{-2}. Hence, there is less probability of dislocations in devices with small active regions. DSDs, and the glide of existing misfit dislocations, however, predominate as the cause of rapid degradation in InP-based LEDs.

LEDs may be fabricated which are largely free from these defects and are therefore subject to a slower long term degradation process. This homogeneous degradation is thought to be due to recombination enhanced point defect generation (i.e. vacancies and interstitials), or the migration of impurities into the active region [Ref. 50]. The optical output power $P_e(t)$ may be expressed as a function of the operating time t, and is given by [Ref. 50]:

$$P_e(t) = P_{out} \exp(-\beta_r t) \tag{7.25}$$

where P_{out} is the initial output power and β_r is the degradation rate. The degradation rate is characterized by the activation energy of homogeneous degradation E_a and is a function of temperature. It is given by:

$$\beta_r = \beta_0 \exp[-E_a/KT] \tag{7.26}$$

where β_0 is a proportionality constant, K is Boltzmann's constant and T is the absolute temperature of the emitting region. The activation energy E_a is a variable which is dependent on the material system and the structure of the device. The value

* LEDs which display rapid degradation are sometimes referred to as freak failures [Ref. 49] because they pass the burn-in period but fail earlier in operational life than the main device population.

of E_a is in the range 0.56 to 0.65 eV, and 0.9 to 1.0 eV for surface-emitting GaAs/AlGaAs and InGaAsP/InP LEDs respectively [Ref. 9]. These values suggest 10^6 to 10^7 hours (100 to 1000 years) CW operation at room temperature for AlGaAs devices, and in excess of 10^9 hours for surface-emitting InGaAsP LEDs.

Example 7.8

An InGaAsP surface emitter has an activation energy of 1 eV with a constant of proportionality (β_0) of 1.84×10^7 h^{-1}. Estimate the CW operating lifetime for the LED with a constant junction temperature of 17 °C, if it is assumed that the device is no longer useful when its optical output power has diminished to 0.67 of its original value.

Solution: Initially, it is necessary to obtain the degradation rate β_r, thus from Eq. (7.26):

$$\begin{aligned}\beta_r &= \beta_0 \exp[-E_a/KT] \\ &= 1.84 \times 10^7 \exp\left[\frac{-1 \times 1.602 \times 10^{-19}}{1.38 \times 10^{-23} \times 290}\right] \\ &= 1.84 \times 10^7 \exp[-40] \\ &= 7.82 \times 10^{-11}\ \text{h}^{-1}\end{aligned}$$

Now using Eq. (7.25):

$$\frac{P_e(t)}{P_{out}} = \exp(-\beta_r t) = 0.67$$

Therefore

$$\beta_r t = -\ln 0.67$$

and

$$\begin{aligned}t &= \frac{\ln 0.67}{7.82 \times 10^{-11}} = \frac{0.40}{7.82 \times 10^{-11}} \\ &= 5.1 \times 10^9\ \text{h}\end{aligned}$$

Hence the estimated lifetime of the device under the specified conditions in Example 7.8 is 5.1×10^9 hours. It must be noted that the junction temperature, even for a device operating at room temperature, is likely to be well in excess of room temperature when substantial drive currents are passed. Also the diminished level of optical output in the example is purely arbitrary and for many applications this reduced level may be unacceptable.

Nevertheless it is quite common for the device lifetime or median life to be determined for a 50% drop in light output power from the device [Ref. 49]. It is clear, however, that with the long term LED degradation process there is no absolute end-of-life power level and therefore to a large extent it is system dependent such that a trade-off can be made between the required system end-of-life power margin and the device reliability [Ref. 44]. Hence the allocated drop to end-of-life power can be substantially reduced to, say, 20% which will provide for an enhanced system power margin (e.g. increased repeater spacing) at the expense of the device median life. Overall, even with these more rigorous conditions the anticipated median life for such LEDs is excellent and it is unlikely to cause problems in most optical fiber communication system applications.

Extrapolated accelerated lifetime tests are also in broad agreement with the theoretical estimates [Refs. 47, 49 to 53] for the less sophisticated device structures. For example, a planar GaAs/AlGaAs DH LED exhibited a median life for a 50% output power reduction of 9×10^7 hours at a temperature of 25 °C [Ref. 52]. By comparison, extrapolated half-power lifetimes in excess of 10^8 hours at a temperature of 60 °C have been obtained with high speed (greater than 200 Mbit s^{-1}) InGaAsP/InP LEDs [Ref. 53].

7.5 Modulation

In order to transmit information via an optical fiber communication system it is necessary to modulate a property of the light with the information signal. This property may be intensity, frequency, phase or polarization (direction) with either digital or analog signals. The choices are indicated by the characteristics of the optical fiber, the available optical sources and detectors, and considerations of the overall system.

However, at present in optical fiber communications considerations of the above for practical systems tend to dictate some form of intensity modulation of the source. Although much effort has been expended and considerable success has been achieved in the area of coherent optical communications (see Chapter 12) the widescale deployment of such systems will take some further time. Therefore intensity modulation (IM) of the optical source and envelope or direct detection (DD) at the optical receiver is likely to remain the major modulation strategy* in the immediate future.

Intensity modulation is easy to implement with the electroluminescent sources available at present (LEDs and injection lasers). These devices can be directly modulated simply by variation of their drive currents at rates up to several gigahertz. Thus direct modulation of the optical source is satisfactory for the modulation bandwidths currently under investigation. However, considering the recent interest in integrated optical devices (see Chapter 10) it is likely that external

* This strategy is often referred to as intensity modulation/direct detection, or IM/DD

optical modulators [Ref. 54] may be utilized more in the future in order to achieve greater bandwidths and to allow the use of nonsemiconductor sources (e.g. Nd : YAG laser) which cannot be directly modulated at high frequency (see Section 6.9.1). External optical modulators are active devices which tend to be used primarily to modulate the frequency or phase of the light, but may also be used for time division multiplexing and switching of optical signals. However, modulation considerations within this text (excepting Chapter 12) will mainly be concerned with the direct modulation of the intensity of the optical source.

Intensity modulation may be utilized with both digital and analog signals. Analog intensity modulation is usually easier to apply but requires comparatively large signal to noise ratios (see Section 9.2.5) and therefore it tends to be limited to relatively narrow bandwidth, short distance applications. Alternatively, digital intensity modulation gives improved noise immunity but requires wider bandwidths, although these may be small in comparison with the available bandwidth. It is therefore ideally suited to optical fiber transmission where the available bandwidth is large. Hence at present most fiber systems in the medium to long distance range use digital intensity modulation.

Problems

7.1 Describe with the aid of suitable diagrams the mechanism giving the emission of light from an LED. Discuss the effects of this mechanism on the properties of the LED in relation to its use as an optical source for communications.

7.2 Briefly outline the advantages and drawbacks of the LED in comparison with the injection laser for use as a source in optical fiber communications.

7.3 The power generated internally within a double heterojunction LED is 28.4 mW at a drive current of 60 mA. Determine the peak emission wavelength from the device when the radiative and nonradiative recombination lifetimes of the minority carriers in the active region are equal.

7.4 The diffusion length L_D or the average distance moved by charge carriers before recombination in the active region of an LED is given by:

$$L_D = (D\tau)^{\frac{1}{2}}$$

where D is the diffusion coefficient and τ is the total carrier recombination lifetime. Calculate the diffusion coefficient in gallium arsenide when the diffusion length is 21 μm and the radiative and nonradiative carrier recombination lifetimes are equal at 90 ns.

7.5 Estimate the external power efficiency of a GaAs planar LED when the transmission factor of the GaAs–air interface is 0.68 and the internally generated optical power is 30% of the electrical power supplied. The refractive index of GaAs may be taken as 3.6.

7.6 The external power efficiency of an InGaAsP/InP planar LED is 0.75% when the internally generated optical power is 30 mW. Determine the transmission factor for the InP–air interface if the drive current is 37 mA and the potential difference across the device is 1.6 V. The refractive index of InP may be taken as 3.46.

7.7 A GaAs planar LED emitting at a wavelength of 0.85 μm has an internal quantum efficiency of 60% when passing a forward current of 20 mA s^{-1}. Estimate the optical

power emitted by the device into air, and hence determine the external power efficiency if the potential difference across the device is 1 V. It may be assumed that the transmission factor at the GaAs–air interface is 0.68 and that the refractive index of GaAs is 3.6. Comment on any assumptions made.

7.8 The external power efficiency of a planar GaAs LED is 1.5% when the forward current is 50 mA and the potential difference across its terminals is 2 V. Estimate the optical power generated within the device if the transmission factor at the coated GaAs–air interface is 0.8.

7.9 Outline the common LED structures for optical fiber communications discussing their relative merits and drawbacks. In particular, compare surface- and edge-emitting devices. Comment on the distinction between multimode and single-mode devices.

7.10 Derive an expression for the coupling efficiency of a surface-emitting LED into a step index fiber, assuming the device to have a Lambertian output. Determine the optical loss in decibels when coupling the optical power emitted from the device into a step index fiber with an acceptance angle of 14°. It may be assumed that the LED is smaller than the fiber core and that the two are in close proximity.

7.11 Considering the LED of problem 7.5, calculate:

(a) the coupling efficiency and optical loss in decibels of coupling the emitted light into a step index fiber with an NA of 0.15, when the device is in close proximity to the fiber and is smaller than the fiber core;

(b) the optical loss relative to the optical power generated internally if the device emits into a thin air gap before light is coupled into the fiber.

7.12 Estimate the optical power coupled into a 50 μm diameter core step index fiber with an NA of 0.18 from a DH surface emitter with an emission area diameter of 75 μm and a radiance of 60 W sr^{-1} cm^{-2}. The Fresnel reflection at index matched semiconductor–fiber interface may be considered negligible.

Further, determine the optical loss when coupling light into the fiber relative to the power emitted by the device into air if the Fresnel reflection at the semiconductor–air interface is 30%.

7.13 Comment on the differences in the performance characteristics between the conventional LEDs used for optical fiber communications and superluminescent LEDs.

Describe, with the aid of a diagram the structure of an SLD used for operation in the longer wavelength region and suggest potential application areas for such devices.

7.14 The Fresnel reflection coefficient at a fiber core of refractive index n_1 is given approximately from the classical Fresnel formulae by

$$r = \left[\frac{n_1 - n}{n_1 + n}\right]^2$$

where n is the refractive index of the surrounding medium.

(a) Estimate the optical loss due to Fresnel reflection at a fiber core from GaAs each of which have refractive indices of 1.5 and 3.6 respectively.

(b) Calculate the optical power coupled into a 200 μm diameter core step index fiber with an NA of 0.3 from a GaAs surface-emitting LED with an emission diameter of 90 μm and a radiance of 40 W sr^{-1} cm^{-2}. Comment on the result.

(c) Estimate the optical power emitted into air for the device in (b).

7.15 Determine the overall power conversion efficiency for the LED in Problem 7.14 if it is operating with a drive current of 100 mA and a forward voltage of 1.9 V.

7.16 Discuss lens coupling of LEDs to optical fibers and outline the various techniques employed.

7.17 Discuss the relationship between the electrical and optical modulation bandwidths for an optical fiber communication system. Estimate the 3 dB optical bandwidth corresponding to a 3 dB electrical bandwidth of 50 MHz. A Gaussian frequency response may be assumed.

7.18 Determine the optical modulation bandwidth for the LED of Problem 7.14 if the device emits 840 μW of optical power into air when modulated at a frequency of 150 MHz.

7.19 Estimate the electrical modulation bandwidth for an LED with a carrier recombination lifetime of 8 ns. The frequency response of the device may be assumed to be Gaussian.

7.20 Discuss the reliability of LEDs in comparison with injection lasers.

Estimate the CW operating lifetime for an AlGaAs LED with an activation energy of 0.6 eV and a constant of proportionality (β_0) of 2.3×10^3 h^{-1} when the junction temperature of the device is constant at 50 °C. It may be assumed that the LED is no longer useful when its optical output power is 0.8 of its original value.

7.21 What is meant by the intensity modulation of an optical source? Give reasons for the major present use of direct intensity modulation of semiconductor optical sources and comment on possible alternatives.

Answers to numerical problems

7.3 1.31 μm
7.4 9.8×10^{-3} m s^{-1}
7.5 0.4%
7.6 0.70
7.7 230 μW, 1.15%
7.8 97.2 mW
7.10 12.3 dB
7.11 (a) 16.7 dB
(b) 35.2 dB
7.12 0.12 mW, 16.9 dB
7.14 (a) 0.81 dB
(b) 600 μW
(c) 5.44 mW
7.15 0.32%
7.17 70.7 MHz
7.18 40.6 MHz
7.19 24.4 MHz
7.20 2.21×10^5 hours

References

[1] D. N. Christodoulides, L. A. Reith and M. A. Saifi, 'Theory of LED coupling to single mode fibers', *J. Lightwave Technol.*, **LT-5**(11), pp. 1623–1629, 1987.

[2] L. Hafskjaer and A. S. V. Sudbo, 'Attenuation and bit-rate limitations in LED/single-mode fiber transmission systems', *J. Lightwave Technol.*, **6**(12), pp. 1793–1797, 1988.

[3] T. P. Lee and A. G. Dentai, 'Power and modulation bandwidth of GaAs–AlGaAs high radiance LEDs for optical communication systems', *IEEE J. Quantum Electron.*, **QE-14**(3), pp. 150–156, 1978.

[4] G. Keiser, *Optical Fiber Communications*, McGraw-Hill, 1983.

[5] H. Kressel, 'Electroluminescent sources for fiber systems', in M. K. Barnoski (Ed.), *Fundamentals of Optical Fiber Communications*, pp. 109–141, Academic Press, 1976.

[6] R. C. Goodfellow and R. Davis, 'Optical source devices', in M. J. Howes and D. V. Morgan (Eds.), *Optical Fibre Communications*, pp. 27–106, John Wiley, 1980.

[7] J. P. Wittke, M. Ettenburg and H. Kressel, 'High radiance LED for single fiber optical links', *RCA Rev.*, **37**(2), pp. 160–183, 1976.
[8] T. G. Giallorenzi, 'Optical communications research and technology: fiber optics', *Proc. IEEE*, **66**, pp. 744–780, 1978.
[9] A. A. Bergh and P. J. Dean, *Light-Emitting Diodes*, Oxford University Press, 1976.
[10] C. A. Burrus and R. W. Dawson, 'Small area high-current density GaAs electroluminescent diodes and a method of operation for improved degradation characteristics', *Appl. Phys. Lett.*, **17**(3), pp. 97–99, 1970.
[11] C. A. Burrus and B. I. Miller, 'Small-area double heterostructure aluminum-gallium arsenide electroluminescent diode sources for optical fiber transmission lines', *Opt. Commun.*, **4**, pp. 307–369, 1971.
[12] T. P. Lee, 'Recent developments in light emitting diodes for optical fiber communication systems', *Proc. SPIE Int. Soc. Opt. Eng.* (USA), **224**, pp. 92–101, 1980.
[13] T. P. Lee, C. A. Burrus Jr and R. H. Saul, 'Light-emitting diodes for telecommunications', in S. E. Miller and I. P. Kaminow (Eds.) *Optical Fiber Telecommunications II*, Academic Press, pp. 467–507, 1988.
[14] T. Uji and J. Hayashi, 'High-power single-mode optical-fiber coupling to InGaAsP 1.3 μm mesa-structure surface emitting LEDs', *Electron. Lett.*, **21**(10), pp. 418–419, 1985.
[15] D. Gloge, 'LED design for fibre system', *Electron. Lett.*, **13**(4), pp. 399–400, 1977.
[16] D. Marcuse, 'LED fundamentals: Comparison of front and edge emitting diodes', *IEEE J. Quantum Electron.*, **QE-13**(10), pp. 819–827, 1977.
[17] D. Botez and M. Ettenburg, 'Comparison of surface and edge emitting LEDs for use in fiber-optical communications', *IEEE Trans. Electron. Devices*, **ED-26**(3), pp. 1230–1238, 1979.
[18] M. Ettenburg, H. Kressel and J. P. Wittke, 'Very high radiance edge-emitting LED', *IEEE J. Quantum Electron.*, **QE-12**(6), pp. 360–364, 1979.
[19] D. H. Newman, M. R. Matthews and I. Garrett, 'Sources for optical fiber communications', *Telecommun. J. (Eng. Ed.) Switzerland*, **48**(2), pp. 673–680, 1981.
[20] D. H. Newman and S. Ritchie, 'Sources and detectors for optical fiber communications applications: the first 20 years', *IEE Proc. Pt. J*, **133**(3), pp. 213–228, 1986.
[21] S. Fujita, J. Hayashi, Y. Isoda, T. Uji and M. Shikada, '2 Gbit/s and 600 Mbit/s single-mode fibre transmission experiments using a high speed Zn-doped 1.3 μm edge-emitting LED', *Electron. Lett.*, **13**(12), pp. 636–637, 1987.
[22] D. M. Fye, 'Low-current 1.3 μm edge-emitting LED for single-mode fiber subscriber loop applications', *J. Lightwave Technol.*, **LT-4**(10), pp. 1546–1551, 1986.
[23] T. Ohtsuka, N. Fujimoto, K. Yamaguchi, A. Taniguchi, N. Naitou and Y. Nabeshima, 'Gigabit single-mode fiber transmission using 1.3 μm edge-emitting LEDs for broadband subscriber loops', *J. Lightwave Technol.*, **LT-5**(10), pp. 1534–1541, 1987.
[24] S. Takahashi, K. Goto, T. Shiba, K. Yoshida, E. Omura, H. Namizaki and W. Susaki, 'High-coupled-power high-speed 1.3 μm edge-emitting LED with buried crescent structure on p-InP substrate', *Tech. Dig. Optical Fiber Communications Conf., OFC 88* (USA), paper WB5, January 1988.
[25] Y. Sakakibara, H. Higuchi, E. Oomura, Y. Nakajima, Y. Yamamoto, K. Goto, H. Namizaki, K. Ikeda and W. Susaki, 'High-power 1.3 μm InGaAsP p-substrate buried cresent lasers', *J. Lightwave Technol.*, **LT-3**(5), pp. 978–984, 1985.
[26] T. P. Lee, C. A. Burrus and B. I. Miller, 'A Stripe-geometry double-heterostructure

amplified-spontaneous-emission (superluminescent) diode', *IEEE J. Quantum Electron.*, **QE-9**, p. 820, 1973.

[27] I. P. Kaminow, G. E. Eisenstein, L. W. Stulz and A. G. Dentai, 'Lateral confinement InGaAsP superluminescent diode at 1.3 μm', *IEEE J. Quantum Electron.*, **QE-19**(1), pp. 78–82, 1983.

[28] Y. Kashima, M. Kobayashi and T. Takano, 'High output power GaInAsP/InP superluminescent diode at 1.3 μm', *Electron. Lett.*, **24**(24), pp. 1507–1508, 1988.

[29] G. Arnold, H. Gottsman, O. Krumphoiz, E. Schlosser and E. A. Schurr, '1.3 μm edge-emitting diodes launching 250 μW into single-mode fiber at 100 mA', *Electron. Lett.*, **21**(21), pp. 993–994, 1985.

[30] M. Abe, I. Umebu, O. Hasegawa, S. Yamakoshi, T. Yamaoka, T. Kotani, H. Okada and H. Takamashi, 'Highly efficient long lived GaAlAs LEDs for fiber-optical communications', *IEEE Trans. Electron. Devices*, **ED-24**(7), pp. 990–994, 1977.

[31] R. A. Abram, R. W. Allen and R. C. Goodfellow, 'The coupling of light emitting diodes to optical fibres using sphere lenses', *J. Appl. Phys.*, **46**(8), pp. 3468–3474, 1975.

[32] O. Wada, S. Yamakoshi, A. Masayuki, Y. Nishitani and T. Sakurai, 'High radiance InGaAsP/InP lensed LEDs for optical communication systems at 1.2–1.3 μm, *IEEE J. Quantum Electron.*, **QE-17**(2), pp. 174–178, 1981.

[33] R. C. Goodfellow, A. C. Carter, I. Griffith and R. R. Bradley, 'GaInAsP/InP fast, high radiance, 1.05–1.3 μm wavelength LEDs with efficient lens coupling to small numerical aperture silica optical fibers', *IEEE Trans. Electron. Devices*, **ED-26**(8), pp. 1215–1220, 1979.

[34] J. Ure, A. C. Carter, R. C. Goodfellow and M. Harding, 'High power lens coupled 1.3 μm edge-emitting LED for long haul 140 Mb/s fiber optics systems', *IEEE Specialist Conf. on Light Emitting Diodes and Photodetectors* (Canada), paper 20, p. 204, 1982.

[35] R. H. Saul, W. C. King, N. A. Olsson, C. L. Zipfel, B. H. Chin, A. K. Chin, I. Camlibel and G. Minneci, '180 Mbit/s, 35 km transmission over single-mode fiber using 1.3 μm edge-emitting LEDs', *Electron. Lett.*, **21**(17), pp. 773–775, 1985.

[36] J. Straus, 'The nonlinearity of high-radiance light-emitting diodes', *IEEE J. Quantum Electron.*, **QE-14**(11), pp. 813–819, 1979.

[37] J. Straus, 'Linearized transmitters for analog fiber links', *Laser Focus (USA)*, **14**(10), pp. 54–61, 1978.

[38] A. C. Carter, 'Light-emitting diodes for optical fibre systems', *Radio Electron. Eng. J. IERE*, **51**(7/8), pp. 341–348, 1981.

[39] H. Tempkin, C. L. Zipfel, M. A. DiGiuseppe, A. K. Chin, V. G. Keramides and R. H. Saul, 'InGaAsP LEDs for 1.3 μm optical transmission', *Bell Syst. Tech. J.*, **62** (1) pp. 1–24, 1983.

[40] I. Garrett and J. E. Midwinter, 'Optical communication systems', in M. J. Howes and D. V. Morgan (Eds.), *Optical Fibre Communications*, pp. 251–300, John Wiley, 1980.

[41] H. Kressel and J. K. Butler, *Semiconductor Lasers and Heterojunction LEDs*, Academic Press, 1977.

[42] H. F. Lockwood, J. P. Wittke and M. Ettenburg, 'LED for high data rate, optical communications', *Opt. Commun.*, **16**, p. 193, 1976.

[43] T. P. Lee, 'Recent development in light emitting diodes (LEDs) for optical fiber communications systems', *Proc. SPIE Int. Soc. Opt. Eng. (USA)*, **340**, pp. 22–31, 1982.

[44] R. H. Saul, 'Recent advances in the performance and reliability of InGaAsP LEDs for lightwave communication systems', *IEEE Trans. Electron. Devices*, **ED-30**(4), pp. 285–295, 1983.

[45] T. P. Lee and A. G. Dentai, 'Power and modulation bandwidth of GaAs–AlGaAs high radiance LEDs for optical communication systems', *IEEE J. Quantum Electron.*, **QE-14**, pp. 150–159, 1978.

[46] J. Heinen, W. Huber and W. Harth, 'Light-emitting diodes with a modulation bandwidth of more than 1 GHz', *Electron. Lett.*, **12**, p. 533, 1976.

[47] W. C. King, B. H. Chin, I. Camlibel and E. L. Zipfel, 'High-speed high-power 1.3 μm InGaAsP/InP surface emitting LEDs for short-haul wide-bandwidth optical fiber communications', *IEEE Electron. Device Lett.*, **EDL-6**, p. 335, 1985.

[48] A. Suzuki, Y. Inomoto, J. Hayashi, Y. Isoda, T. Uji and H. Nomura, 'Gbit/s modulation of heavily Zn-doped surface-emitting InGaAsP/InP DH LED', *Electron. Lett.*, **20**, p. 274, 1984.

[49] N. K. Dutta and C. L. Zipfel, 'Reliability of lasers and LEDs', in S. E. Miller and I. P. Kaminow (Eds.), *Optical Fiber Telecommunications II*, Academic Press, pp. 671–687, 1988.

[50] S. Yamakoshi, A. Masayuki, O. Wada, S. Komiya and T. Sakurai, 'Reliability of high radiance InGaAsP/InP LEDs operating in the 1.2–1.3 μm wavelength', *IEEE J. Quantum Electron.*, **QE-17**(2), pp. 167–173, 1981.

[51] S. Yamakoshi, T. Sugahara, O. Hasegawa, Y. Toyama and H. Takanashi, 'Growth mechanism of ⟨100⟩ dark-line defects in high radiance GaAlAs LEDs', *International Electronic Devices Meeting*, pp. 642–645, 1978.

[52] C. L. Zipfel, A. K. Chin, V. G. Keramidas and R. H. Saul, 'Reliability of DH $Ga_{1-x}Al_xAs$ LEDs for lightwave communications', *Proc. 19th Ann., IEEE Int. Reliab. Phys. Symp.*, pp. 124–129, 1981.

[53] A. Suzuki, T. Uji, Y. Inomoto, J. Hayashi, Y. Isoda and H. Nomura, 'InGaAsP/InP 1.3 μm wavelength surface-emitting LED's for high-speed short-haul optical communication systems', *J. of Lightwave Technol.*, **LT-3**(6), pp. 1217–1222, 1985.

[54] S. M. Stone, 'Modulation of optical sources', in E. E. Basch (Ed.) *Optical-Fiber Transmission*, H. W. Sams & Co., pp. 303–334, 1987.

8

Optical detectors

8.1 Introduction
8.2 Device types
8.3 Optical detection principles
8.4 Absorption
8.5 Quantum efficiency
8.6 Responsivity
8.7 Long wavelength cutoff
8.8 Semiconductor photodiodes without internal gain
8.9 Semiconductor photodiodes with internal gain
8.10 Mid-infrared photodiodes
8.11 Phototransistors
8.12 Photoconductive detectors
Problems
References

8.1 Introduction

We are concerned in this chapter with photodetectors currently in use and under investigation for optical fiber communications.

The detector is an essential component of an optical fiber communication system and is one of the crucial elements which dictate the overall system performance. Its

function is to convert the received optical signal into an electrical signal, which is then amplified before further processing. Therefore when considering signal attenuation along the link, the system performance is determined at the detector. Improvement of detector characteristics and performance thus allows the installation of fewer repeater stations and lowers both the capital investment and maintenance costs.

The role the detector plays demands that it must satisfy very stringent requirements for performance and compatibility. The following criteria define the important performance and compatibility requirements for detectors which are generally similar to the requirements for sources.

1. *High sensitivity at the operating wavelengths.* The first generation systems have wavelengths between 0.8 and 0.9 μm (compatible with AlGaAs laser and LED emission lines). However, considerable advantage may be gained at the detector from second generation sources with operating wavelengths above 1.1 μm as both fiber attenuation and dispersion are reduced. There is much research activity at present in this longer wavelength region, especially concerning wavelengths around 1.3 μm where attenuation and material dispersion can be minimized. In this case semiconductor materials are currently under investigation (see Section 8.4.3) in order to achieve good sensitivity at normal operating temperatures (i.e. 300 K).
2. *High fidelity.* To reproduce the received signal waveform with fidelity, for analogy transmission the response of the photodetector must be linear with regard to the optical signal over a wide range.
3. *Large electrical response to the received optical signal.* The photodetector should produce a maximum electrical signal for a given amount of optical power, i.e. the quantum efficiency should be high.
4. *Short response time to obtain a suitable bandwidth.* Present systems extend into the hundreds of megahertz. However, it is apparent that future systems (single-mode fiber) will operate in the gigahertz range, and possibly above.
5. *A minimum noise introduced by the detector.* Dark currents, leakage currents and shunt conductance must be low. Also the gain mechanism within either the detector or associated circuitry must be of low noise.
6. *Stability of performance characteristics.* Ideally, the performance characteristics of the detector should be independent of changes in ambient conditions. However, the detectors currently favoured (photodiodes) have characteristics (sensitivity, noise, internal gain) which vary with temperature, and therefore compensation for temperature effects is often necessary.
7. *Small size.* The physical size of the detector must be small for efficient coupling to the fiber and to allow easy packaging with the following electronics.
8. *Low bias voltages.* Ideally the detector should not require excessive bias voltages or currents.
9. *High reliability.* The detector must be capable of continuous stable operation at room temperature for many years.

10. *Low cost.* Economic considerations are often of prime importance in any large scale communication system application.

We continue the discussion in Section 8.2 by briefly indicating the various types of device which could be employed for optical detection. From this discussion it is clear that semiconductor photodiodes currently provide the best solution for detection in optical fiber communications. Therefore, in Sections 8.3 and 8.4 we consider the principles of operation of these devices, together with the characteristics of the semiconductor materials employed in their construction. Sections 8.5–8.7 then briefly outline the major operating parameters (quantum efficiency, responsivity, long wavelength cutoff) of such photodiodes. Following, in Sections 8.8 and 8.9, we discuss the structure, operation and performance characteristics of the major device types (*p–n*, *p–i–n* and avalanche photodiodes) for optical detection over the wavelength range 0.8 to 1.6 μm. Then in Section 8.10 recent developments associated with photodiodes for mid-infrared detection (particularly up to 2.6 μm) are considered prior to discussion in Sections 8.11 and 8.12 of other semiconductor devices (heterojunction phototransistors and photoconductive detectors) which may eventually find wider use as detectors for optical fiber communications.

8.2 Device types

To detect optical radiation (photons) in the near-infrared region of the spectrum, both external and internal photoemission of electrons may be utilized. External photoemission devices typified by photomultiplier tubes and vacuum photodiodes meet some of the performance criteria but are too bulky, and require high voltages for operation. However, internal photoemission devices especially semiconductor photodiodes with or without internal (avalanche) gain provide good performance and compatibility with relatively low cost. These photodiodes are made from semiconductors such as silicon, germanium and an increasing number of III–V alloys, all of which satisfy in various ways most of the detector requirements. They are therefore used in all major current optical fiber communication systems.

The internal photoemission process may take place in both intrinsic and extrinsic semiconductors. With intrinsic absorption, the received photons excite electrons from the valence to the conduction bands in the semiconductor, whereas extrinsic absorption involves impurity centres created within the material. However, for fast response coupled with efficient absorption of photons, the intrinsic absorption process is preferred and at present all detectors for optical fiber communications use intrinsic photodetection.

Silicon photodiodes [Ref. 1] have high sensitivity over the 0.8–0.9 μm wavelength band with adequate speed (hundreds of megahertz), negligible shunt conductance, low dark current and long term stability. They are therefore widely used in first generation systems and are currently commercially available. Their

usefulness is limited to the first generation wavelength region as silicon has an indirect bandgap energy (see Section 8.4.1) of 1.14 eV giving a loss in response above 1.09 μm. Thus for second generation systems in the longer wavelength range 1.1–1.6 μm research is devoted to the investigation of semiconductor materials which have narrower bandgaps. Interest has focused on germanium and III–V alloys which give a good response at the longer wavelengths. Again, the performance characteristics of such devices has improved considerably over recent years and a wide selection of III–V alloy photodiodes as well as germanium photodiodes are now commercially available.

In addition to the development of advanced photodiode structures fabricated from III–V semiconductor alloys for operation at wavelengths of 1.3 and 1.55 μm, similar material systems are under investigation for use at the even longer wavelengths required for mid-infrared transmission (2 to 5 μm). Interest has also been maintained in other semiconductor detector types, namely, the heterojunction phototransistor and the photoconductive detector, both of which can be usefully fabricated from III–V alloy material systems. In particular, the latter device type has more recently found favour as a potential detector over the 1.1 to 1.6 μm wavelength range. Nevertheless, at present the primary operating wavelength regions remain 0.8 to 0.9 μm, 1.3 μm and 1.55 μm, with the major device types being the *p–i–n* and avalanche photodiodes. We shall therefore consider these devices in greater detail before discussing mid-infrared photodiodes, phototransistors and photoconductive detectors.

8.3 Optical detection principles

The basic detection process in an intrinsic absorber is illustrated in Figure 8.1 which shows a *p–n* photodiode. This device is reverse biased and the electric field developed across the *p–n* junction sweeps mobile carriers (holes and electrons) to their respective majority sides (*p* and *n* type material). A depletion region or layer is therefore created on either side of the junction. This barrier has the effect of stopping the majority carriers crossing the junction in the opposite direction to the field. However, the field accelerates minority carriers from both sides to the opposite side of the junction, forming the reverse leakage current of the diode. Thus intrinsic conditions are created in the depletion region.

A photon incident in or near the depletion region of this device which has an energy greater than or equal to the bandgap energy E_g of the fabricating material (i.e. $hf \geq E_g$) will excite an electron from the valence band into the conduction band. This process leaves an empty hole in the valence band and is known as the photogeneration of an electron–hole (carrier) pair, as shown in Figure 8.1(a). Carrier pairs so generated near the junction are separated and swept (drift) under the influence of the electric field to produce a displacement by current in the external circuit in excess of any reverse leakage current (Figure 8.1(b)). Photo-

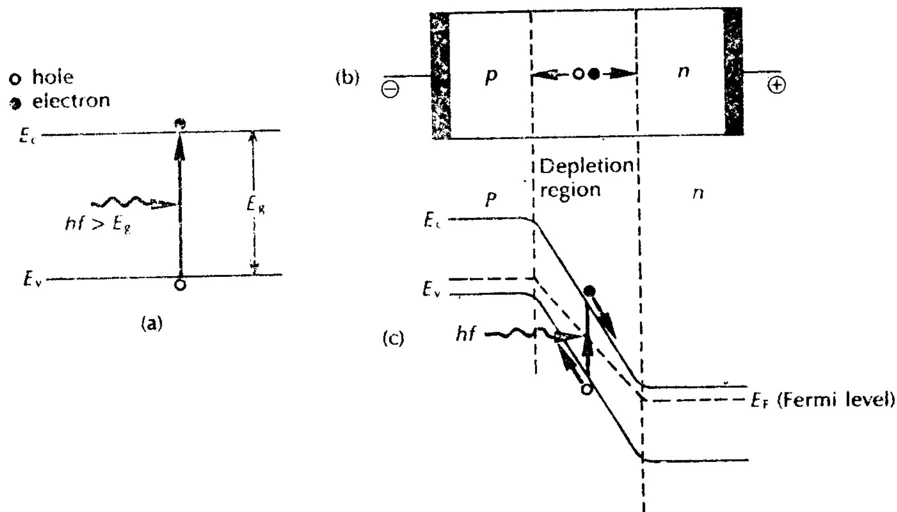

Figure 8.1 Operation of the *p–n* photodiode: (a) photogeneration of an electron–hole pair in an intrinsic semiconductor; (b) the structure of the reverse biased *p–n* junction illustrating carrier drift in the depletion region; (c) the energy band diagram of the reverse biased *p–n* junction showing photo-generation and the subsequent separation of an electron–hole pair.

generation and the separation of a carrier pair in the depletion region of this reverse biased *p–n* junction is illustrated in Figure 8.1(c).

The depletion region must be sufficiently thick to allow a large fraction of the incident light to be absorbed in order to achieve maximum carrier-pair generation. However, since long carrier drift times in the depletion region restrict the speed of operation of the photodiode it is necessary to limit its width. Thus there is a trade-off between the number of photons absorbed (sensitivity) and the speed of response.

8.4 Absorption

8.4.1 Absorption coefficient

The absorption of photons in a photodiode to produce carrier pairs and thus a photocurrent, is dependent on the absorption coefficient α_0 of the light in the semiconductor used to fabricate the device. At a specific wavelength and assuming only bandgap transitions (i.e. intrinsic absorber) the photocurrent I_p produced by incident light of optical power P_o is given by [Ref. 4]:

$$I_p = \frac{P_o e(1-r)}{hf}\,[1 - \exp(-\alpha_0 d)] \tag{8.1}$$

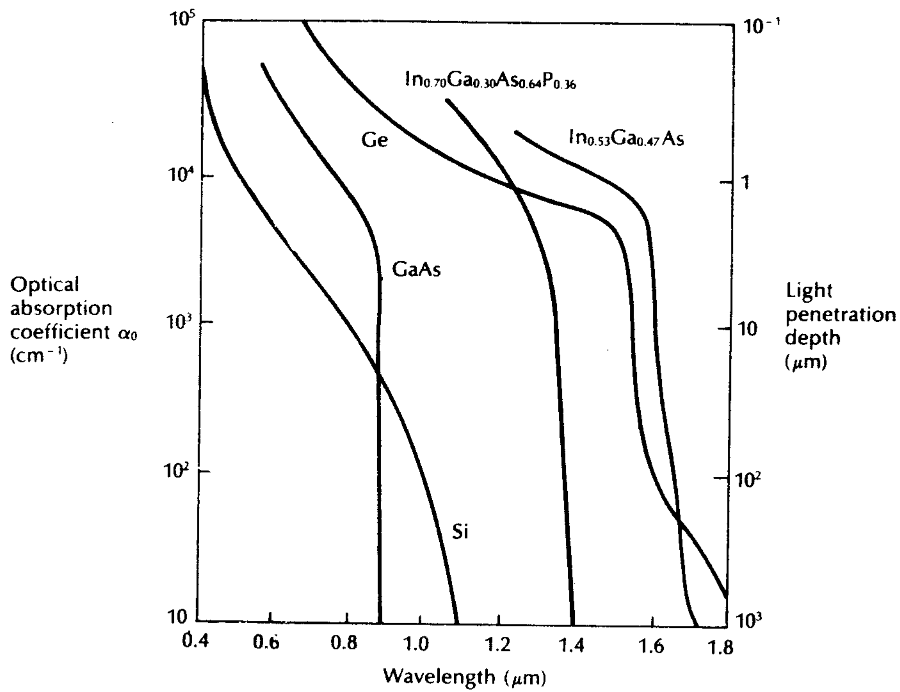

Figure 8.2 Optical absorption curves for some common semiconductor photodiode materials (silicon, germanium, gallium arsenide, indium gallium arsenide and indium gallium arsenide phosphide).

Table 8.1 Bandgaps for some semiconductor photodiode materials at 300 K

	Bandgap (eV) at 300 K	
	Indirect	Direct
Si	1.14	4.10
Ge	0.67	0.81
GaAs	—	1.43
InAs	—	0.35
InP	—	1.35
GaSb	—	0.73
$In_{0.53}Ga_{0.47}As$	—	0.75
$In_{0.14}Ga_{0.86}As$	—	1.15
$GaAs_{0.88}Sb_{0.12}$	—	1.15

where e is the charge on an electron, r is the Fresnel reflection coefficient at the semiconductor–air interface and d is the width of the absorption region.

The absorption coefficients of semiconductor materials are strongly dependent on wavelength. This is illustrated for some common semiconductors [Ref. 4] in Figure 8.2. It may be observed that there is a variation between the absorption curves for the materials shown and that they are each suitable for different wavelength applications. This results from their differing bandgaps energies, as show in Table 8.1. However, it must be noted that the curves depicted in Figure 8.2 also vary with temperature.

8.4.2 Direct and indirect absorption: silicon and germanium

Table 8.1 indicates that silicon and germanium absorb light by both direct and indirect optical transitions. Indirect absorption requires the assistance of a photon so that momentum as well as energy are conserved. This makes the transition probability less likely for indirect absorption than for direct absorption where no photon is involved. In this context direct and indirect absorption may be contrasted with direct and indirect emission discussed in Section 6.3.3.1. Therefore as may be seen from Figure 8.2 silicon is only weakly absorbing over the wavelength band of interest in optical fiber communications (i.e. first generation 0.8 to 0.9 μm). This is because transitions over this wavelength band in silicon are due only to the indirect absorption mechanism. As mentioned previously (Section 8.2) the threshold for indirect absorption occurs at 1.09 μm. The bandgap for direct absorption in silicon is 4.10 eV, corresponding to a threshold of 0.30 μm in the ultraviolet, and thus is well outside the wavelength range of interest.

Germanium is another semiconductor material for which the lowest energy absorption takes place by indirect optical transitions. However, the threshold for direct absorption occurs at 1.53 μm, below which germanium becomes strongly absorbing, corresponding to the kink in the characteristic shown in Figure 8.2. Thus germanium may be used in the fabrication of detectors over the whole of the wavelength range of interest (i.e. first and second generation 0.8 to 1.6 μm), especially considering that indirect absorption will occur up to a threshold of 1.85 μm.

Ideally, a photodiode material should be chosen with a bandgap energy slightly less than the photon energy corresponding to the longest operating wavelength of the system. This gives a sufficiently high absorption coefficient to ensure a good response, and yet limits the number of thermally generated carriers in order to achieve a low dark current (i.e. displacement current generated with no incident light (see Figure 8.5)). Germanium photodiodes have relatively large dark currents due to their narrow bandgaps in comparison to other semiconductor materials. This is a major disadvantage with the use of germanium photodiodes, especially at shorter wavelengths (below 1.1 μm).

8.4.3 III–V alloys

The drawback with germanium as a fabricating material for semiconductor photodiodes has led to increased investigation of direct bandgap III–V alloys for the longer wavelength region. These materials are potentially superior to germanium because their bandgaps can be tailored to the desired wavelength by changing the relative concentrations of their constituents, resulting in lower dark currents. They may also be fabricated in heterojunction structures (see Section 6.3.5) which enhances their high speed operations.

Ternary alloys such as InGaAs and GaAlSb deposited on InP and GaSb substrates, respectively, have been used to fabricate photodiodes for the longer wavelength band. Although difficulties were experienced in the growth of these alloys, with lattice matching causing increased dark currents, these problems have now been reduced. In particular the alloy $In_{0.53}Ga_{0.47}As$ lattice matched to InP, which responds to wavelengths up to around 1.7 μm (see Figure 8.2), has been extensively utilized in the fabrication of photodiodes for operation at both 1.3 and 1.55 μm. Quaternary alloys are also under investigation for detection at these wavelengths. Both InGaAsP grown on InP and GaAlAsSb grown on GaSb have been studied, with the former material system finding significant application within advanced photodiode structures.

8.5 Quantum efficiency

The quantum efficiency η is defined as the fraction of incident photons which are absorbed by the photodetector and generate electrons which are collected at the detector terminals:

$$\eta = \frac{\textit{number of electrons collected}}{\textit{number of incident photons}} \tag{8.2}$$

Hence,

$$\eta = \frac{r_e}{r_p} \tag{8.3}$$

where r_p is the incident photon rate (photons per second) and r_e is the corresponding electron rate (electrons per second).

One of the major factors which determines the quantum efficiency is the absorption coefficient (see Section 8.4.1) of the semiconductor material used within the photodetector.The quantum efficiency is generally less than unity as not all of the incident photons are absorbed to create electron–hole pairs. Furthermore, it should be noted that it is often quoted as a percentage (e.g. a quantum efficiency of 75% is equivalent to 75 electrons collected per 100 incident photons). Finally, in common with the absorption coefficient, the quantum efficiency is a function of the photon wavelength and must therefore only be quoted for a specific wavelength.

8.6 Responsivity

The expression for quantum efficiency does not involve photon energy and therefore the responsivity R is often of more use when characterizing the performance of a photodetector. It is defined as:

$$R = \frac{I_p}{P_o} \ (AW^{-1}) \tag{8.4}$$

where I_p is the output photocurrent in amperes and P_o is the incident optical power in watts. The responsivity is a useful parameter as it gives the transfer characteristic of the detector (i.e. photocurrent per unit incident optical power).

The relationship for responsivity (Eq. (8.4)) may be developed to include quantum efficiency as follows. Considering Eq. (6.1) the energy of a photon $E = hf$. Thus the incident photon rate r_p may be written in terms of incident optical power and the photon energy as:

$$r_p = \frac{P_o}{hf} \tag{8.5}$$

In Eq. (8.3) the electron rate is given by:

$$r_e = \eta r_p \tag{8.6}$$

Substituting from Eq. (8.5) we obtain

$$r_e = \frac{\eta P_o}{hf} \tag{8.7}$$

Therefore, the output photocurrent is:

$$I_p = \frac{\eta P_o e}{hf} \tag{8.8}$$

where e is the charge on an electron. Thus from Eq. (8.4) the responsivity may be written as:

$$R = \frac{\eta e}{hf} \tag{8.9}$$

Equation (8.9) is a useful relationship for responsivity which may be developed a stage further to include the wavelength of the incident light.

The frequency f of the incident photons is related to their wavelength λ and the velocity of light in air c, by:

$$f = \frac{c}{\lambda} \tag{8.10}$$

Substituting into Eq. (8.9) a final expression for the responsivity is given by:

$$R = \frac{\eta e \lambda}{hc} \tag{8.11}$$

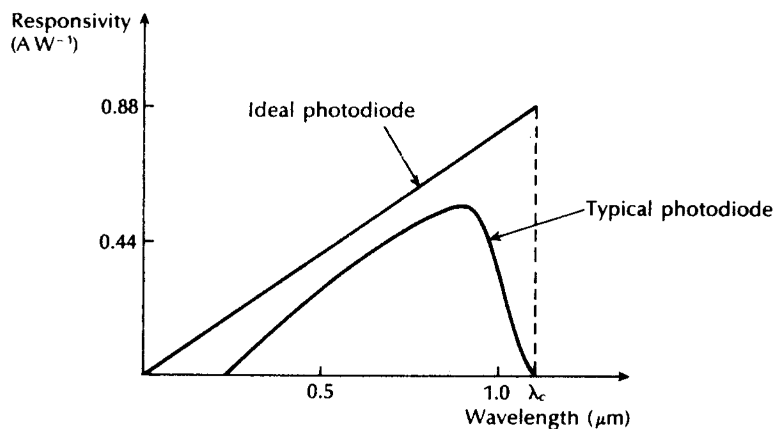

Figure 8.3 Responsivity against wavelength characteristic for an ideal silicon photodiode. The responsivity of a typical device is also shown.

It may be noted that the responsivity is directly proportional to the quantum efficiency at a particular wavelength.

The ideal responsivity against wavelength characteristic for a silicon photodiode with unit quantum efficiency is illustrated in Figure 8.3. Also shown is the typical responsivity of a practical silicon device.

Example 8.1

When 3×10^{11} photons each with a wavelength of $0.85\ \mu m$ are incident on a photodiode, on average 1.2×10^{11} electrons are collected at the terminals of the device. Determine the quantum efficiency and the responsivity of the photodiode at $0.85\ \mu m$.

Solution: From Eq. (8.2),

$$\text{Quantum efficiency} = \frac{\text{number of electrons collected}}{\text{number of incident photons}}$$

$$= \frac{1.2 \times 10^{11}}{3 \times 10^{11}}$$

$$= 0.4$$

The quantum efficiency of the photodiode at $0.85\ \mu m$ is 40%.

From Eq. (8.11),

$$\textit{Responsivity } R = \frac{\eta e \lambda}{hc}$$

$$= \frac{0.4 \times 1.602 \times 10^{-19} \times 0.85 \times 10^{-6}}{6.626 \times 10^{-34} \times 2.998 \times 10^{8}}$$

$$= 0.274 \text{ A W}^{-1}$$

The responsivity of the photodiode at 0.85 μm is 0.27 A W^{-1}.

Example 8.2

A photodiode has a quantum efficiency of 65% when photons of energy 1.5×10^{-19} J are incident upon it.

(a) At what wavelength is the photodiode operating?
(b) Calculate the incident optical power required to obtain a photocurrent of 2.5 μA when the photodiode is operating as described above.

Solution: (a) From Eq. (6.1), the photon energy $E = hf = hc/\lambda$. Therefore

$$\lambda = \frac{hc}{E} = \frac{6.626 \times 10^{-34} \times 2.998 \times 10^{8}}{1.5 \times 10^{-19}}$$

$$= 1.32 \ \mu\text{m}$$

The photodiode is operating at a wavelength of 1.32 μm.

(b) From Eq. (8.9),

$$\textit{Responsivity } R = \frac{\eta e}{hf} = \frac{0.65 \times 1.602 \times 10^{-19}}{1.5 \times 10^{-19}}$$

$$= 0.694 \text{ A W}^{-1}$$

Also from Eq. (8.4).

$$R = \frac{I_p}{P_o}$$

Therefore

$$P_o = \frac{2.5 \times 10^{-6}}{0.694} = 3.60 \ \mu\text{W}$$

The incident optical power required is 3.60 μW.

8.7 Long wavelength cutoff

It is essential when considering the intrinsic absorption process that the energy of incident photons be greater than or equal to the bandgap energy E_g of the material used to fabricate the photodetector. Therefore, the photon energy

$$\frac{hc}{\lambda} \geqslant E_g \tag{8.12}$$

giving

$$\lambda \leqslant \frac{hc}{E_g} \tag{8.13}$$

Thus the threshold for detection, commonly known as the long wavelength cutoff point λ_c, is:

$$\lambda_c = \frac{hc}{E_g} \tag{8.14}$$

The expression given in Eq. (8.14) allows the calculation of the longest wavelength of light to give photodetection for the various semiconductor materials used in the fabrication of detectors.

It is important to note that the above criterion is only applicable to intrinsic photodetectors. Extrinsic photodetectors violate the expression given in Eq. (8.12), but are not currently used in optical fiber communications.

Example 8.3

GaAs has a bandgap energy of 1.43 eV at 300 K. Determine the wavelength above which an intrinsic photodetector fabricated from this material will cease to operate.

Solution: From Eq. (8.14), the long wavelength cutoff:

$$\lambda_c = \frac{hc}{E_g} = \frac{6.626 \times 10^{-34} \times 2.998 \times 10^8}{1.43 \times 1.602 \times 10^{-19}}$$

$$= 0.867\ \mu\text{m}$$

The GaAs photodetector will cease to operate above 0.87 μm.

8.8 Semiconductor photodiodes without internal gain

Semiconductor photodiodes without internal gain generate a single electron-hole pair per absorbed photon. This mechanism was outlined in Section 8.3, and in order to understand the development of this type of photodiode it is now necessary to elaborate upon it.

8.8.1 *p–n* Photodiode

Figure 8.4 shows a reverse biased *p–n* photodiode with both the depletion and diffusion regions. The depletion region is formed by immobile positively charged donor atoms in the *n* type semiconductor material and immobile negatively charged acceptor atoms in the *p* type material, when the mobile carriers are swept to their majority sides under the influence of the electric field. The width of the depletion region is therefore dependent upon the doping concentrations for a given applied reverse bias (i.e. the lower the doping, the wider the depletion region). For the interested reader expressions for the depletion layer width are given in Ref. 5.

Photons may be absorbed in both the depletion and diffusion regions, as indicated by the absorption region in Figure 8.4. The absorption region's position and width depends upon the energy of the incident photons and on the material from which the photodiode is fabricated. Thus in the case of the weak absorption of photons, the absorption region may extend completely throughout the device. Electron–hole pairs are therefore generated in both the depletion and diffusion regions. In the depletion region the carrier pairs separate and drift under the influence of the electric field, whereas outside this region the hole diffuses towards the depletion region in order to be collected. The diffusion process is very slow compared to drift and thus limits the response of the photodiode (see Section 8.8.3).

It is therefore important that the photons are absorbed in the depletion region. Thus it is made as long as possible by decreasing the doping in the *n* type material. The depletion region width in a *p–n* photodiode is normally 1 to 3 μm and is optimized for the efficient detection of light at a given wavelength. For silicon

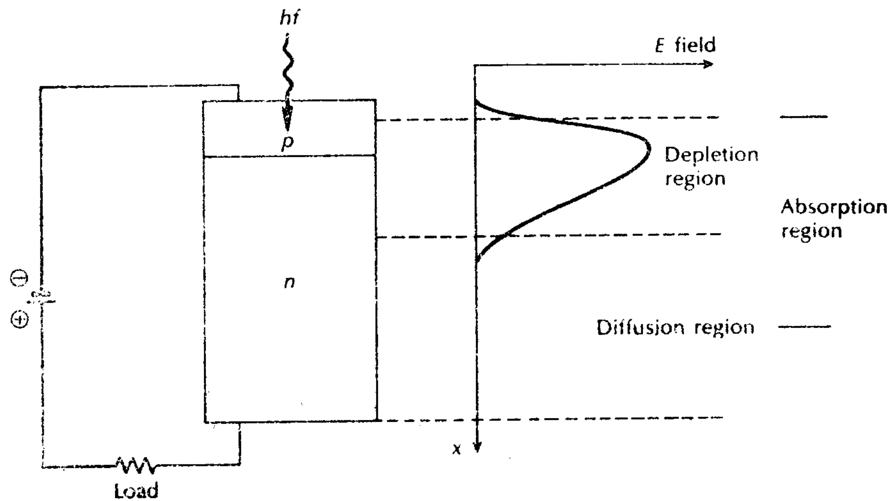

Figure 8.4 *p–n* photodiode showing depletion and diffusion regions.

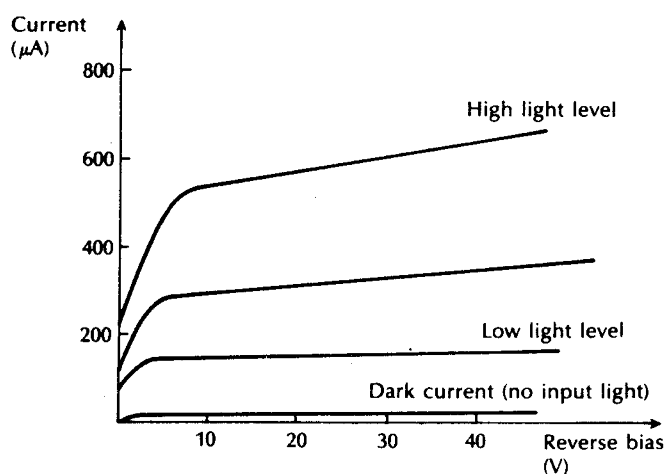

Figure 8.5 Typical *p–n* photodiode output characteristics.

devices this is in the visible spectrum (0.4 to 0.7 μm) and for germanium in the near infrared (0.7 to 0.9 μm).

Typical output characteristics for the reverse-biased *p–n* photodiode are illustrated in Figure 8.5. The different operating conditions may be noted moving from no light input to a high light level.

8.8.2 *p–i–n* Photodiode

In order to allow operation at longer wavelengths where the light penetrates more deeply into the semiconductor material a wider depletion region is necessary. To achieve this the *n* type material is doped so lightly that it can be considered intrinsic, and to make a low resistance contact a highly doped *n* type (n^+) layer is added. This creates a *p–i–n* (or PIN) structure, as may be seen in Figure 8.6 where all the absorption takes place in the depletion region.

Figure 8.7 shows the structures of two types of silicon *p–i–n* photodiode for operation in the shorter wavelength band below 1.09 μm. The front illuminated photodiode, when operating in the 0.8 to 0.9 μm band (Figure 8.7(a)), requires a depletion region of between 20 and 50 μm in order to attain high quantum efficiency (typically 85%) together with fast response (less than 1 ns) and low dark current (1 nA). Dark current arises from surface leakage currents as well as generation–recombination currents in the depletion region in the absence of illumination. The side illuminated structure (Figure 8.7(b)), where light is injected parallel to the junction plane, exhibits a large absorption width ($\simeq 500$ μm) and hence is particularly sensitive at wavelengths close to the bandgap limit (1.09 μm) where the absorption coefficient is relatively small.

Germanium *p–i–n* photodiodes which span the entire wavelength range of interest are also commercially available, but as mentioned previously (Section 8.4.2)

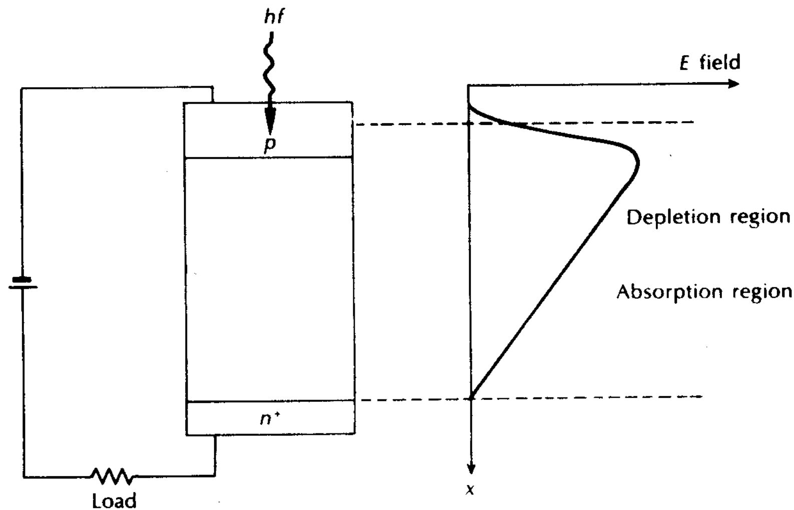

Figure 8.6 *p–i–n* photodiode showing combined absorption and depletion region.

the relatively high dark currents are a problem (typically 100 nA at 20 °C increasing to 1 μA at 40 °C). However, as outlined in Section 8.4.3, III–V semiconductor alloys have been employed in the fabrication of longer wavelength region detectors. At present, the favoured material is the lattice matched $In_{0.53}Ga_{0.47}As/InP$ system [Ref. 6] which can detect at wavelengths up to 1.67 μm. A typical planar device structure is shown in Figure 8.8(a) [Ref. 7] which requires epitaxial growth of several layers on an *n* type InP substrate. The incident light is absorbed in the low doped *n* type InGaAs layer generating carriers, as illustrated in the energy band diagram Figure 8.8(b) [Ref. 8]. The discontinuity due to the homojunction between the n^+–InP substrate and the *n*–InGaAs absorption region may be noted. This can be reduced by the incorporation of an *n* type InP buffer layer.

The top entry* device shown in Figure 8.8(a) is the simplest structure, with the light being introduced through the upper p^+ layer. However, a drawback with this structure is a quantum efficiency penalty which results from optical absorption in the undepleted p^+ region. In addition, there is a limit to how small such a device can be fabricated as both light access and metallic contact are required on the top. To enable smaller devices with lower capacitances to be made a substrate entry technique is employed. In this case light enters through a transparent InP substrate and the device area can be fabricated as small as may be practical for bonding.

Conventional growth techniques for III–V semiconductors can be employed to fabricate these devices, although liquid phase epitaxy (LPE) tends to be preferred because of the relative ease in obtaining the low doping levels needed (around

* Top entry is also referred to as front illumination.

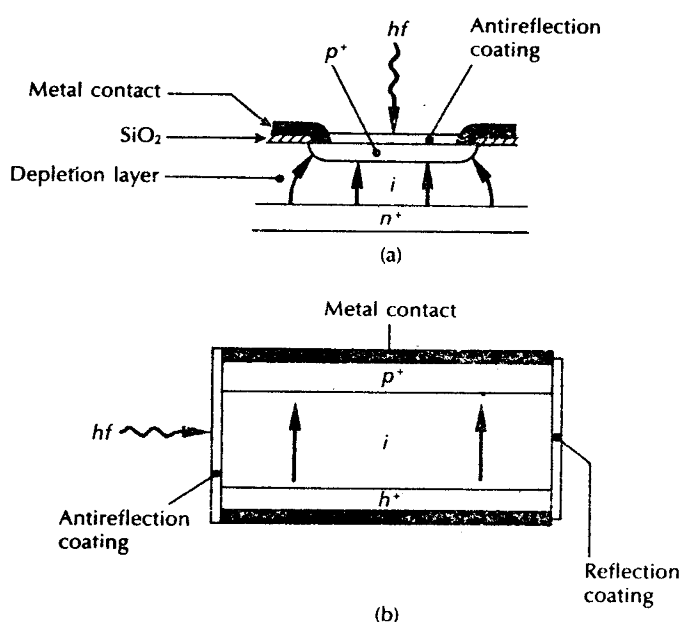

Figure 8.7 (a) Structure of a front illuminated silicon *p–i–n* photodiode. (b) Structure of a side illuminated (parallel to junction) *p–i–n* photodiode.

10^5 cm^{-3}) to obtain low capacitance (less than 0.2 pF). However, LPE does not easily allow low impurity level concentrations and it is necessary to use long baking procedures over several days to purify the source material. High quality devices have been produced using metal oxide vapour-phase epitaxy (MOVPE) [Ref. 9], a technique which appears much more appropriate for large scale production of such devices.

A substrate entry* *p–i–n* photodiode is shown in Figure 8.9(a). This device incorporates a p^+–InGaAsP layer to provide a heterojunction structure (Schottky barrier) which improves quantum efficiency. Moreover, it is fabricated as a mesa structure which reduces parasitic capacitances [Ref. 10]. Unfortunately, charge trapping can occur at the n^-p^+–InGaAs/InGaAsP interface which may be observed in the energy band diagram of Figure 8.9(b). This may cause limitations in the response time of the device [Ref. 8]. However, small area substrate entry devices can be produced with extremely low capacitance (less than 0.1 pF), quantum efficiency between 75% and 100%, and dark currents less than 1 nA.

In both device types a depleted InGaAs layer of around 3 μm is used which provides high quantum-efficiency and bandwidth. Furthermore, low doping permits full depletion of the InGaAs layer at low voltage (5 V). The short transit times in

* Substrate entry is also referred to as back illumination.

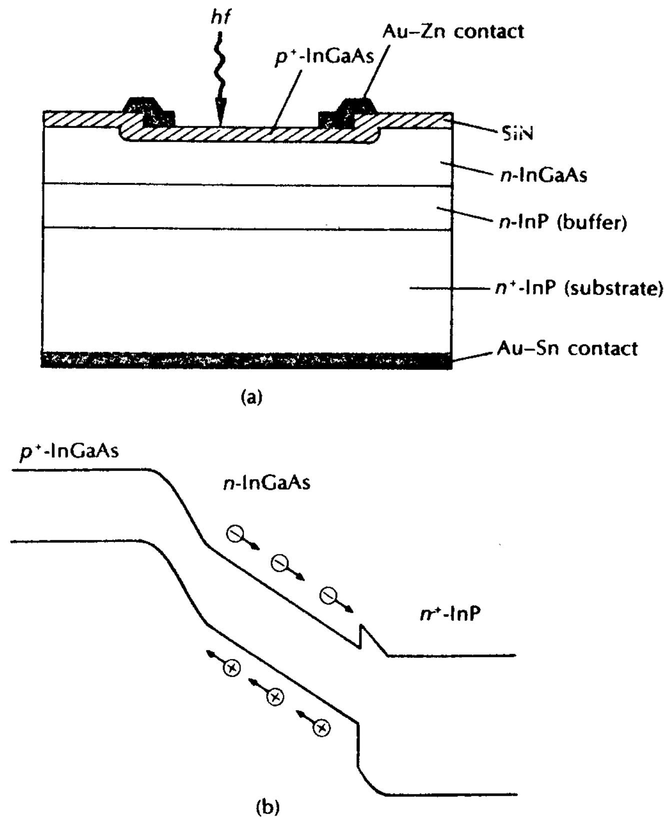

Figure 8.8 Planar InGaAs *p–i–n* photodiode: (a) structure; (b) energy band diagram showing homojunction associated with the conventional *p–i–n* structure.

the relatively narrow depletion layers give a theoretical bandwidth of approximately 15 GHz. However, the bandwidth of commercially available packaged detectors is usually between 1 and 2 GHz due to limitations of the packaging.

8.8.3 Speed of response

Three main factors limit the speed of response of a photodiode. These are [Ref. 11]:

(a) *Drift time of carriers through the depletion region*
The speed of response of a photodiode is fundamentally limited by the time it takes photogenerated carriers to drift across the depletion region. When the field in the depletion region exceeds a saturation value then the carriers may be assumed to travel at a constant (maximum) drift velocity v_d. The longest transit

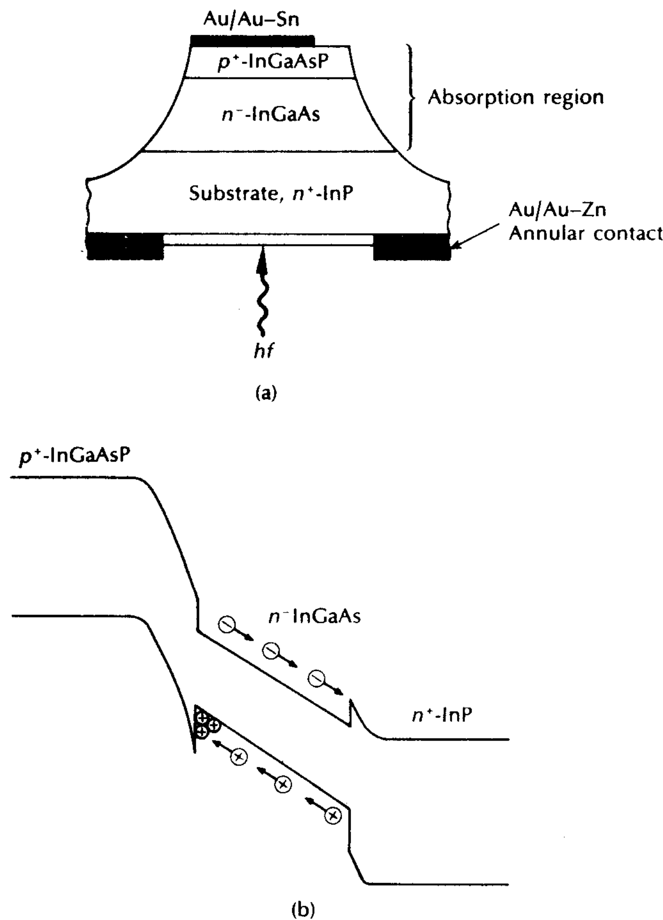

Figure 8.9 Substrate entry InGaAs *p–i–n* photodiode: (a) structure; (b) energy band diagram illustrating the heterojunction and charge trapping.

time, t_{drift}, is for carriers which must traverse the full depletion layer width w and is given by

$$t_{drift} = \frac{w}{v_d} \qquad 15)$$

A field strength above $2 \times 10^4\ \mathrm{V\,cm^{-1}}$ in silicon gives maximum (saturated) carrier velocities of approximately $10^7\ \mathrm{cm\,s^{-1}}$. Thus the transit time through a depletion layer width of 10 μm is around 0 1 ns.

(b) *Diffusion time of carriers generated outside the depletion region*
Carrier diffusion is a comparatively slow process where the time taken, t_{diff}, fo

carriers to diffuse a distance d may be written as

$$t_{\text{diff}} = \frac{d^2}{2D_c} \tag{8.16}$$

where D_c is the minority carrier diffusion coefficient. For example, the hole diffusion time through 10 μm of silicon is 40 ns whereas the electron diffusion time over a similar distance is around 8 ns.

(c) *Time constant incurred by the capacitance of the photodiode with its load*
A reversed biased photodiode exhibits a voltage dependent capacitance caused by the variation in the stored charge at the junction. The junction capacitance C_j is given by

$$C_j = \frac{\varepsilon_s A}{w} \tag{8.17}$$

where ε_s is the permittivity of the semiconductor material and A is the diode junction area. Hence, a small depletion layer width w increases the junction capacitance. The capacitance of the photodiode C_d is that of the junction together with the capacitance of the leads and packaging. This capacitance must be minimized in order to reduce the RC time constant which also limits the detector response time (see Section 9.3.2).

Although all the above factors affect the response time of the photodiode, the ultimate bandwidth of the device is limited by the drift time of carriers through the depletion region t_{drift}. In this case when assuming no carriers are generated outside the depletion region and that there is negligible junction capacitance, then the maximum photodiode 3 dB bandwidth B_m is given by [Ref.12]:

$$B_m = \frac{1}{2\pi t_{\text{drift}}} = \frac{v_d}{2\pi w} \tag{8.18}$$

Moreover, when there is no gain mechanism present within the device structure, the maximum possible quantum efficiency is 100%. Hence the value for the bandwidth given by Eq. (8.18) is also equivalent to the ultimate gain–bandwidth product for the photodiode.

Example 8.4

The carrier velocity in a silicon *p–i–n* photodiode with a 25 μm depletion layer width is 3×10^4 m s^{-1}. Determine the maximum response time for the device.

Solution: The maximum 3 dB bandwidth for the photodiode may be obtained from Eq. (8.18) where:

$$B_m = \frac{v_d}{2\pi_w} = \frac{3 \times 10^4}{2\pi \times 25 \times 10^{-6}} = 1.91 \times 10^8 \text{ Hz}$$

The maximum response time for the device is therefore:

$$\text{Max. response time} = \frac{1}{B_m} = 5.2 \text{ ns}$$

It must be noted, however, that the above response time takes no account of the diffusion of carriers in the photodiode or the capacitance associated with the device junction and the external connections.

The response of a photodiode to a rectangular optical input pulse for various device parameters is illustrated in Figure 8.10. Ideally, to obtain a high quantum efficiency for the photodiode the width of the depletion layer must be far greater than the reciprocal of the absorption coefficient (i.e. $1/\alpha_0$) for the material used to fabricate the detector so that most of the incident light will be absorbed. Hence the response to a rectangular input pulse of a low capacitance photodiode meeting this condition, and exhibiting negligible diffusion outside the depletion region, is shown in Figure 8.10(a). It may be observed in this case that the rising and falling edges of the photodiode output follow the input pulse quite well. When the detector capacitance is larger, however, the speed of response becomes limited by the RC time constant of this capacitance and the load resistor associated with the receiver circuit (see Section 9.3.2), and thus the output pulse appears as illustrated in Figure 8.10(b).

Furthermore, when there is significant diffusion of carriers outside the depletion region, as is the case when the depletion layer is too narrow ($w \leqslant 1/\alpha_0$) and carriers are therefore created by absorption outside this region, then the output pulse displays a long tail caused by the diffusion component to the input optical pulse, as shown in Figure 8.10(c). Thus devices with very thin depletion layers have a tendency to exhibit distinctive fast response and slow response components to their output pulses, as may be observed in Figure 8.10(c). The former response resulting from absorption in the thin depletion layer.

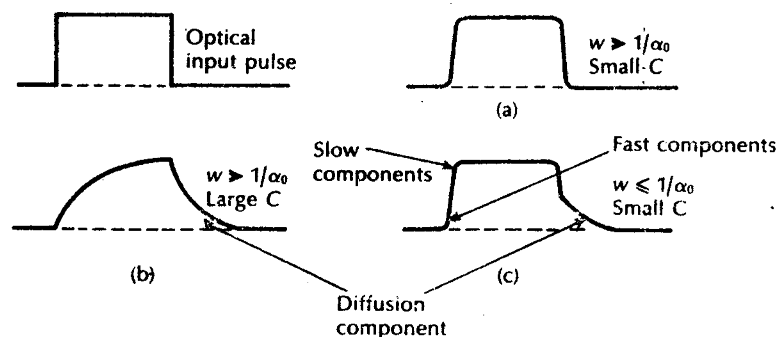

Figure 8.10 Photodiode responses to rectangular optical input pulses for various detector parameters.

8.8.4 Noise

The overall sensitivity of a photodiode results from the random current and voltage fluctuations which occur at the device output terminals in both the presence and absence of an incident optical signal. Although the factors that determine the sensitivity of the optical receiver are dealt with in Chapter 9, it is appropriate at this stage to consider the sources of noise that arise within photodiodes, which do not have an internal gain mechanism. The photodiode dark current mentioned in Section 8.8.2 corresponds to the level of the output photocurrent when there is no intended optical signal present. However, there may be some photogenerated current present due to background radiation entering the device.

The inherent dark current can be minimized through the use of high quality, defect-free material which reduces the number of carriers generated in the depletion region as well as those which diffuse into this layer from the p^+ and n^+ regions. Moreover, the surface currents can be minimized by careful fabrication and surface passivation such that the surface state and impurity ion concentrations are reduced. Nevertheless, it is the case that the detector average current $\bar{I}$ always exhibits a random fluctuation about its mean value as a result of the statistical nature of the quantum detection process (see Section 9.2.3). This fluctuation is exhibited as shot noise [Ref. 13] where the mean square current variation $\overline{i_s^2}$ is proportional to $\bar{I}$ and the photodiode received bandwidth B. Thus the rms value of this shot noise current is:

$$(\overline{i_s^2})^{\frac{1}{2}} = (2eB\bar{I})^{\frac{1}{2}} \tag{8.19}$$

Various figures of merit have traditionally been employed to assess the noise performance of optical detectors. Although these parameters are not always appropriate for the evaluation of the high speed photodiodes used in optical fiber communications, it is instructive to define those most commonly utilized. These are: the noise equivalent power (NEP); the detectivity (D); and the specific detectivity (D^*).

The NEP is defined as the incident optical power, at a particular wavelength or with a specified spectral content required to produce a photodetector current equal to the rms noise current within a unit bandwidth (i.e. $B = 1$ Hz). To obtain an expression for the NEP at a specific wavelength, Eq. (8.8) must be rearranged as follows to give:

$$P_o = \frac{I_p hf}{\eta e} = \frac{I_p hc}{\eta e \lambda} \tag{8.20}$$

Then putting the photocurrent I_p equal to the rms shot noise current in Eq. (8.19) gives:

$$I_p = (2e\bar{I}B)^{\frac{1}{2}} \tag{8.21}$$

Moreover, the photodiode average current $\bar{I}$ may be represented by $(I_p + I_d)$ where I_d is the dark current within the device. Hence:

$$I_p = [2e(I_p + I_d)B]^{\frac{1}{2}} \tag{8.22}$$

When $I_p \gg I_d$, then:

$$I_p \simeq 2eB \tag{8.23}$$

Substituting Eq. (8.23) into Eq. (8.20) and putting $B = 1$ Hz gives the noise equivalent power as:

$$NEP = P_o \simeq \frac{2hc}{\eta\lambda} \tag{8.24}$$

It should be noted that the NEP for an ideal photodetector is given by Eq. (8.24) when the quantum efficiency $\eta = 1$.

When $I_p \ll I_d$, then from Eq. (8.22) the photocurrent becomes:

$$I_p \simeq [2eI_dB]^{\frac{1}{2}} \tag{8.25}$$

Hence for a photodiode in which the dark current noise is dominant, the use of Eq. (8.20) with $B = 1$ Hz gives an expression for the noise equivalent power of:

$$NEP = P_o \simeq \frac{hc(2eI_d)^{\frac{1}{2}}}{\eta e\lambda} \tag{8.26}$$

The detectivity D is defined as the inverse of the NEP; thus:

$$D = \frac{1}{NEP} \tag{8.27}$$

Considering a photodiode receiving monochromatic radiation with the dark current as its dominant noise source, then from Eqs. (8.26) and (8.27):

$$D = D_\lambda = \frac{\eta e\lambda}{hc(2eI_d)^{\frac{1}{2}}} \tag{8.28}$$

The specific detectivity D^* is a parameter which incorporates the area of the photodetector A in order to take account of the effect of this factor on the amplitude of the device dark current. This proves necessary when background radiation and thermal generation rather than surface conduction are the major causes of dark current. Therefore the specific detectivity is given by:

$$D^* = DA^{\frac{1}{2}} = \frac{\eta e\lambda}{hc(2eI_d/A)^{\frac{1}{2}}} \tag{8.29}$$

It should be noted, however, that the above definition for D^* assumes a bandwidth of 1 Hz. Hence the specific detectivity over a bandwidth B would be equal to $D(AB)^{\frac{1}{2}}$.

Example 8.5

A germanium p–i–n photodiode with active dimensions of $100 \times 50\ \mu$m has a quantum efficiency of 55% when operating at a wavelength of 1.3 μm. The

measured dark current at this wavelength is 8 nA. Calculate the noise equivalent power and specific detectivity for the device. It may be assumed that dark current is the dominant noise source.

Solution: The noise equivalent power is given by Eq. (8.26) as:

$$NEP \simeq \frac{hc(2eI_d)^{\frac{1}{2}}}{\eta e \lambda}$$

$$= \frac{6.626 \times 10^{-34} \times 2.998 \times 10^{8}(2 \times 1.602 \times 10^{-19} \times 8 \times 10^{-9})^{\frac{1}{2}}}{0.55 \times 1.602 \times 10^{-19} \times 1.3 \times 10^{-6}}$$

$$= 8.78 \times 10^{-14}\ \mathrm{W}$$

Substituting for the detectivity D in Eq. (8.29) from Eq. (8.27) allows the specific detectivity to be written as:

$$D^* = \frac{A^{\frac{1}{2}}}{NEP} = \frac{(100 \times 10^{-6} \times 50 \times 10^{-6})^{\frac{1}{2}}}{8.78 \times 10^{-14}}$$

$$= 8.1 \times 10^{8}\ \mathrm{m\,Hz^{\frac{1}{2}}\,W^{-1}}$$

The above parameters are solely concerned with the noise performance of the photodiodes used within optical fiber communications. However, it is the noise associated with the optical receiver which also incorporates a load resistance and a preamplifier that is the major concern. This more general issue is dealt with in Chapter 9.

8.9 Semiconductor photodiodes with internal gain

8.9.1 Avalanche photodiodes

The second major type of optical communications detector is the avalanche photodiode (APD). This has a more sophisticated structure than the *p–i–n* photodiode in order to create an extremely high electric field region (approximately 3×10^5 V cm^{-1}), as may be seen in Figure 8.11(a). Therefore, as well as the depletion region where most of the photons are absorbed and the primary carrier pairs generated there is a high field region in which holes and electrons can acquire sufficient energy to excite new electron–hole pairs. This process is known as impact ionization and is the phenomenon that leads to avalanche breakdown in ordinary reverse biased diodes. It often requires high reverse bias voltages (50 to 400 V) in order that the new carriers created by impact ionization can themselves produce additional carriers by the same mechanism as shown in Figure 8.11(b). More recently, however, it should be noted that devices which will operate at much lower bias voltages (15 to 25 V) have become available.

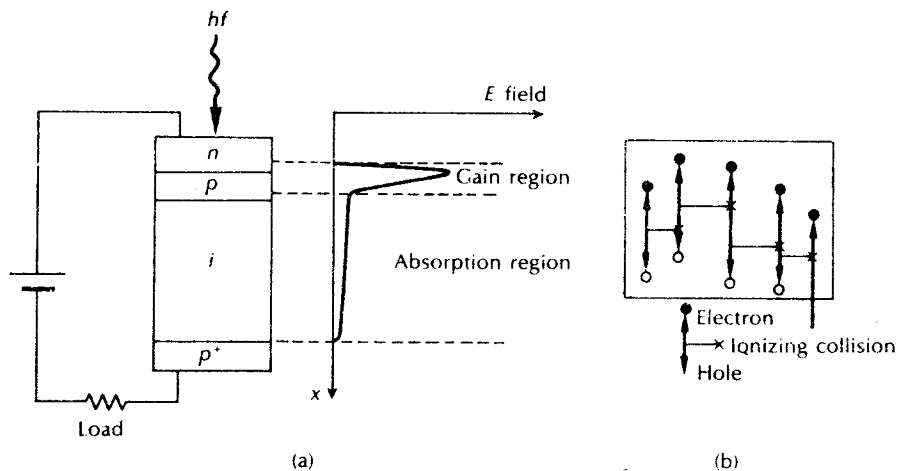

Figure 8.11 (a) Avalanche photodiode showing high electric field (gain) region. (b) Carrier pair multiplication in the gain region.

Carrier multiplication factors as great as 10^4 may be obtained using defect-free materials to ensure uniformity of carrier multiplication over the entire photosensitive area. However, other factors affect the achievement of high gain within the device. Microplasmas, which are small areas with lower breakdown voltages than the remainder of the junction, must be reduced through the selection of defect-free materials together with careful device processing and fabrication [Ref. 14]. In addition, excessive leakage at the junction edges can be eliminated by the use of a guard ring structure as shown in Figure 8.12. At present both silicon and germanium APDs are available.

Operation of these devices at high speed requires full depletion in the absorption region. As indicated in Section 8.8.1, when carriers are generated in undepleted

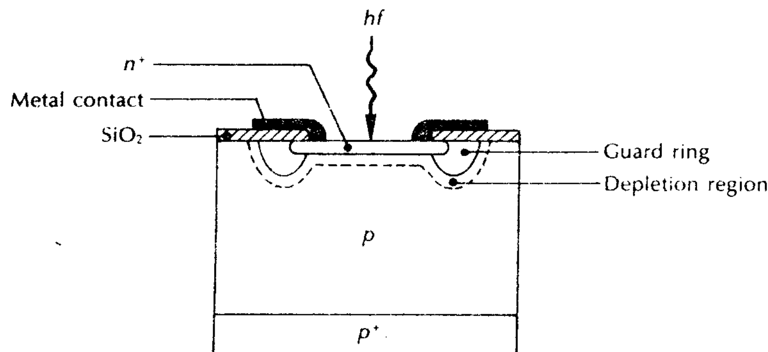

Figure 8.12 Structure of a silicon avalanche photodiode with guard ring.